

Two aspects of Bi₂Se₃ quasi 2D nanoflakes: Flexible, Wearable Pressure Sensor and SSPM based All-Optical Switching and Photonic Logic Gate

*A thesis submitted towards partial fulfilment
of the requirements for the degree of*

**Master of Technology
in
Nanoscience and Technology**

Submitted by

SASWATA GOSWAMI

Exam Roll no.: M4NST22004

Registration no.: 154573

Under the guidance of

Prof. Kalyan Kumar Chattopadhyay

Thin Film and Nanoscience Laboratory,

Head of the department - Department of Physics,

Professor-School of Materials Science and Nanotechnology

Jadavpur University

Course affiliated to

Faculty of Engineering and Technology

Jadavpur University

Kolkata – 700 032

India

August, 2022

*Dedicated to my parents, younger sister, family members
and Teachers for their endless love, support and
encouragements.*

CERTIFICATE OF RECOMMENDATION

This is to certify that the thesis entitled “Two aspects of Bi₂Se₃ quasi 2D nanoflakes: Flexible, Wearable Pressure Sensor and SSPM based All-Optical Switching and Photonic Logic Gate” is a bonafide work carried out by SASWATA GOSWAMI under our supervision and guidance for partial fulfilment of the requirement of Master of Technology (Nanoscience and Technology) in School of Materials Science and Nanotechnology, Jadavpur university, during academic year 2020 – 2022.



Prof. Kalyan Kumar Chattopadhyay

Thesis advisor

Professor, School of Materials Science and Nanotechnology,
Professor and Head of the Department of Physics,
Jadavpur University,
Kolkata – 700 032.



Prof. Kalyan Kr. Chattopadhyay
Professor and Head
Department of Physics
Jadavpur University
Kolkata – 700 032

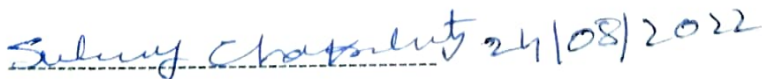


Dr. Sourav Sarkar

Director

School of Materials Science and Nanotechnology,
Jadavpur University,
Kolkata – 700 032

Dr. Sourav Sarkar
Director
Associate Professor
School of Materials Science & Nanotechnology
Jadavpur University
Kolkata - 700032



Dean

Faculty Council of Interdisciplinary Studies, Law and Management
Jadavpur University,
Kolkata – 700 032

Dean
Faculty of Interdisciplinary Studies
Law & Management
Jadavpur University, Kolkata-700032

CERTIFICATE OF APPROVAL **

This foregoing thesis is hereby approved as a credible study of an engineering subject carried out and presented in a satisfactorily manner to warranty its acceptance as a prerequisite to the degree for which it has been submitted. It is understood that by this approval the undersigned do not endorse or approve any statement made or opinion expressed or conclusion drawn therein but approve the thesis only for purpose for which it has been submitted.

Committee of final examination

for evaluation of Thesis

1. -----
2. -----
3. -----
4. -----

** Only in case the thesis is approved.

DECLARATION OF ORIGINALITY AND COMPLIANCE OF
ACADEMIC ETHICS

I hereby declare that this thesis contains literature survey and original research work done by the undersigned candidate, as part of the Master of Technology (Nanoscience and Technology) studies during academic session 2020-2022. All information in this document has been obtained and presented in accordance with academic rules and ethical conduct. I also declare that, as required by this rules and conduct, I have fully cited and referred all material and results that are not original to this work.

NAME: SASWATA GOSWAMI

ROLL NUMBER: M4NST22004
REGISTRATION NUMBER- 154573

THESIS TITLE: “Two aspects of Bi₂Se₃ quasi 2D nanoflakes: Flexible, Wearable Pressure Sensor and SSPM based All-Optical Switching and Photonic Logic Gate”

Saswata Goswami
SIGNATURE:

24.08.2022
DATE:

Acknowledgement

In the first place, I would like to express my profound gratitude to my supervisor **Prof. (Dr). Kalyan Kumar Chattopadhyay** for his advice and guidance from the very early stage of this research as well as giving me extraordinary experiences throughout the work. Above all and the most needed, he provided me constant encouragement and support in various ways. Thank you also for the amicable environment conducive to extensive research work at Thin Film and Nanoscience Lab, in which you have welcomed me. All these provided me great support, helping me to confront the difficult periods of my project, which I do not think I would have completed it otherwise.

I would also like to express my sincere thanks to Dr. Sourav Sarkar, Dr. Chandan Kumar Ghosh, Dr. Mahua Ghosh Chowdhury, for their help, support, encouragement, suggestion and advice during the course of my M. Tech. program. Their enthusiasm provided me a helpful and effective way of learning which in turn inspired me to follow the research project with great enthusiasm.

I extend my heartiest gratitude to Dr. Biswajit Das, for his constant support with rich scientific ideas, knowledge, encouragement to work hard with systematic analysis and valuable affection to reach the ultimate goal of proposed research. He will always remain very close to my heart not only for his sheer excellence and aptitude in the research field, but also as a good human being and my beloved “dada” who never said “no” at any time of my tenure as well as any queries that seemed really troublesome to my personal life.

I would like to thank Nabamita Chakraborty, research scholar at Thin Film and Nanoscience Laboratory for her constant support and help. Without her valuable support and help, I could not have completed my thesis project work with in scheduled time. She taught me very carefully. And a very special heartiest thanks goes to Avinash

Shaw, my classmate and groupmate for his constant support and help in every aspect of research tenure.

I would also like to thank FIST – II, Department of Physics, and School of Materials Science and Nanotechnology, Jadavpur University for carried out FESEM and all critical characterisation studies that composed a very important part of this thesis.

I extend my heartiest thanks to all my seniors of “Thin Film & Nano Science lab” especially Ankita di, Madhupriya di, Shrabani Di, Souvik Da, Suvankar Poddar da, Pulok da and everyone in this laboratory for extending their helping hands. I would also like to thank all my classmates Tanay Toppo, Mrinmoy Patra, Saswata Mandal, Debashis Bose for their encouragement, cooperation and support.

Abstract

In the past few decades, there has been great emphasis on developing nanomaterials for their practical applications. Extensive effort has been made to design and accurately control the material's composition, morphology, and heterostructures showing exciting properties. Among several properties of the nanostructures, dimensionality is one of the most important parameters. This thesis work aims to address some of the crucial problems.

With modern, flexible electronics development, pressure sensors have drawn much attention. Flexible pressure sensors can be used in many applications such as health care monitoring, human-machine interfacing, robot prosthetics and IOT application. In recent years, flexible electronics have been a topic of massive interest due to their application in various fields, and they are widely employed as pressure sensors. A novel pressure sensor should have high sensitivity, mechanical flexibility, fast response time, low fabrication cost, simple processing, etc. Among different types, the piezo-resistive pressure sensor is thought to be the most energy-efficient and cost-effective as it does not require a complex fabrication method. The signal acquisition methods are also accessible. Recent research contributions mainly focus on the device's cost-effectiveness and efficiency. For these reasons, Bi₂Se₃ Nanoflakes (NFs) have been considered the primary material for this study. The Bi₂Se₃ NFs were synthesized using a simple solvothermal technique. This first work, entitled **"Wearable, Ultrawide-Range, and Bending-Insensitive Pressure Sensor Based on 2D Bi₂Se₃ NFs coated tissue for Human-machine Interface and Healthcare Devices"** aimed to investigate the pressure sensing capabilities of Bi₂Se₃ NFs coated pressure sensor and the application in healthcare device. Layer variation, concentration variation and electrode metal variation are done to find the best sensitive device. The best operating piezo-resistive pressure sensor's sensitivity is 25.1 kPa⁻¹ (in the range 0-2 kPa). In addition, the sensor can detect mobile vibration, weak airflow from the mouth, voice recognition, bending, differentiating between different amounts of pressure etc. All these characteristics are attributed to the high sensitivity of the pressure sensor. Also, the optimized sensor is used to fabricate an array of matrices resembling electronic skin. This e-skin array can be used to detect spatial pressure distribution and pressure magnitude. It is believed that such a low-cost, easy-to-fabricate pressure sensor can open up new opportunities and applications in e-skin and intelligent wearable electronics.

The second work, titled "**Kerr Non-Linearity in 2D Bi₂Se₃ for all Optical Switching and Photonic Logic Gate Application,**" is an optical study of Bi₂Se₃ nanoflakes done to calculate non-linear optical parameters such as non-linear refractive index, third order susceptibility. This study is done using by SSPM technique. Here 2D Bi₂Se₃ nanoflakes were synthesized using a low-cost, simple chemical route. Basic characterizations like FESEM, EDS, XPS, and Raman Spectroscopy were done for deep understanding regarding this nanoflakes sample. The Bi₂Se₃ NFs are a promising material for non-linear optical applications in this study. The calculated non-linear refractive indexes and third order non-linear susceptibility were 7.74×10^{-6} esu and 1.9×10^{-8} esu for NMP solvents, respectively, at 671nm laser excitation. The large values indicate strong coherent non-linear interaction between light and suspended Bi₂Se₃ nanoflakes. Based on the SSPM method, Bi₂Se₃-SnS₂ based diode has been investigated to demonstrate non-reciprocal light propagation. Also, an all-optical "OR" gate application has been performed using the cross-phase modulation method involving two laser beams of a different wavelength. It is believed that such a non-linear optical phenomenon can open up a new pathway for Bi₂Se₃-based all-optical device application.

Table of Contents

<i>Certificate of Recommendation</i>	(iii)
<i>Certificate of Approval</i>	(iv)
<i>Declaration Of Originality and Compliance of Academic Ethics</i>	(v)
<i>Acknowledgement</i>	(vi)
<i>-(vii)</i>	
<i>Abstract</i>	(viii)-(ix)
<i>1.1 Introduction</i>	2
<i>1.2 What makes nano special</i>	3
<i>1.3 History of nanoscience & technology</i>	3
<i>1.4 Application of Nanotechnology</i>	
<i>1.4.1 Renewable Energy</i>	6
<i>1.4.2 Health Care and Longevity</i>	9
<i>1.4.3 Electronics and IT application</i>	9
<i>1.5 Synthesis of nanomaterials</i>	14
<i>1.6 Types of Nanomaterials</i>	15
<i>1.7 Topological Insulator</i>	18
<i>1.8 Two-Dimensional material</i>	22
<i>1.9.1 Introduction to Pressure Sensor</i>	26
<i>1.9.2 Pressure sensor classification according to their performance parameters and fabrication methods</i>	29
<i>1.9.3 Application of Pressure Sensor Device</i>	36
<i>1.10.1 Introduction</i>	38
<i>1.10.2 Non-Linear Kerr Effect</i>	40
<i>1.10.3 SSPM: Mechanism of Light matter Interaction</i>	42
<i>1.10.4 Dynamics of Collapse Phenomena of Diffraction Patterns</i>	43

<i>1.10.5 Application of SSPM Method.....</i>	<i>43</i>
<i>1.11 Aims and Objective of the thesis.....</i>	<i>44</i>
<i>1.12 Orientation of the thesis</i>	<i>44</i>
<i>1.13 References.....</i>	<i>45</i>

Chapter 2

<i>2.1 Literature of past Work: Pressure Sensor Device</i>	<i>52</i>
<i>2.2 Literature of past Work: SSPM.....</i>	<i>64</i>
<i>2.3 References.....</i>	<i>73</i>

Chapter 3

<i>3.1 Crystal Structure Analysis (XRD).....</i>	<i>77</i>
<i>3.2 Morphological Analysis</i>	
<i>3.2.1 Field Emission Scanning Electron Microscopy.....</i>	<i>81</i>
<i>3.2.2 Energy Dispersive X-Ray Spectroscopy (EDS/EDX).....</i>	<i>88</i>
<i>3.2.3 Transmission electron microscopy.....</i>	<i>89</i>
<i>3.3 Raman Scattering</i>	<i>95</i>
<i>3.4 Atomic Force Microscopy.....</i>	<i>100</i>
<i>3.5 Equipment used for Pressure Sensor Experiment</i>	
<i>3.5.1 Keysight B2902A.....</i>	<i>105</i>
<i>3.5.2 Hot Air Oven.....</i>	<i>106</i>

3.5.3 Calibrated Weights.....	107
3.6 Equipment used for SSPM Experiment	
3.6.1 Ultra Sonic Water Bath (Sonicator).....	108
3.6.2 LASER Source.....	110
3.6.3 Laser power meter.....	110
Chapter 4 : Wearable, Ultrawide-Range, and Bending-Insensitive Pressure Sensor Based on 2D Bi ₂ Se ₃ NFs coated tissue for Human-machine Interface and Healthcare Devices	
4.1 Introduction.....	112
4.2 Experimental Technique	
4.2.1 Solvothermal Synthesis and Liquid exfoliation of Bi ₂ Se ₃ Nanoflakes.....	115
4.2.2 Characterization of Bi ₂ Se ₃ Nanoflakes.....	116
4.2.3 Fabrication of Paper based Pressure sensor.....	118
4.3 Results and Discussions	
4.3.1 Pressure Sensing Mechanism and Electro-mechanical Performance of Bi ₂ Se ₃ coated Tissue Paper	120
4.3.2 Application of Bi ₂ Se ₃ functionalized Tissue Paper based Pressure Sensor...	125
4.4 Conclusion.....	130
4.5 References.....	130
Chapter 5: Kerr Non-Linearity in 2D Bi ₂ Se ₃ for all Optical Switching and Photonic Logic Gate Application	
5.1	
Introduction.....	134
5.2 Experimental Technique	
5.2.1 Solvothermal Synthesis and Liquid exfoliation of Bi ₂ Se ₃ Nanoflakes....	136
5.2.2 Characterization of Bi ₂ Se ₃ Nanoflakes.....	138
5.3 Results and Discussion	

5.3.1 Non-Linear Kerr Effect.....	140
5.3.2 SSPM Mechanism of Light Matter Interaction.....	145
5.3.3 Dynamics of the Collapse Process of Diffraction Patterns.....	148
5.3.4 Non-Reciprocal Light Propagation in Bi_2Se_3 based Photonic Diode.....	151
5.3.5 Cross-Phase Modulation: Bi_2Se_3 based All-Optical switching and Logic Gates.....	154
5.4 Conclusions.....	155
5.5 References	156
 Chapter 6 : Grand conclusion and future scope	
6.1 Conclusion.....	159
6.2 Future Scope.....	160

Chapter 1

Introduction

1.1 Introduction

The concept behind nanotechnology started with a famous talk by Richard Feynman at an American Physical Society meeting at the California Institute of Technology on December 29th, 1959, long before the term nanotechnology was even coined. In his famous talk he described the theoretical ways of manipulating and controlling individual atoms and molecules. The field of nanoscience and nanotechnology has been since growing, and has impacted other fields such as chemistry, physics, materials science and other areas also. New path ways of exploring different regime have been unfolded since. Everything we see on the earth is made up of atoms, the food we eat, the clothes we wear. It's impossible for a person to see individual atom with naked eyes, hence came powerful characterization tools such as SEM, TEM etc. Though there have been instances of nanotechnology in the past where artist created stained glass with use of gold and silver nanoparticle on the church walls.[1]

The term nanotechnology was not used until 1974, when a researcher from University of Tokyo, Japan named Norio Taniguchi, used the term to refer the design material at nanometer level. The main driving force came into play due to miniaturization at small scale, this is related to electronics industry. The main motive was to create small scale devices to pack more computer power at a small surface level. In 1970s, IBM in USA created Electron beam lithography technique for nanostructures, capable of performing electronic property.[2] The prefix 'nano' stands for dwarf in Greek, which means something of very small. There is also difference between nanoscience and nanotechnology, nanoscience is the study of structure of materials, compounds at nanometer level, and the technology that involves the application part is called

Chapter:1 Introduction

nanotechnology. As a scale for perception, a human hair is about 60,000nm thick and a DNA helix is about 1 nm thick.

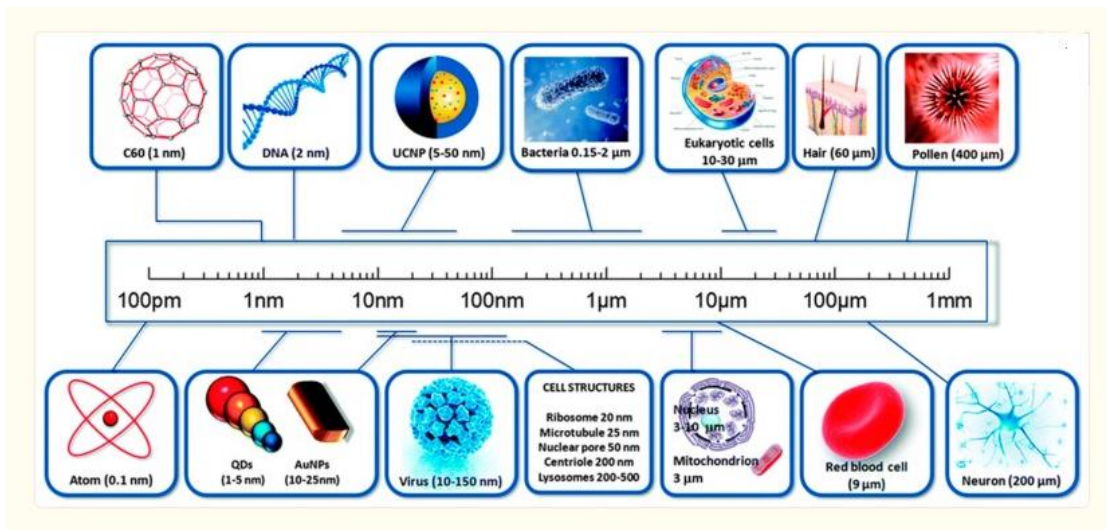


Fig.1.1 Size comparison of material from bulk scale to nano scale.

1.2 What makes nano special?

In the nanoscale dimension the quantum nature of the material becomes evident, due to reduced size. Bulk material possesses macroscopic properties this represents the behavior-based billions and billions of molecules united formed in a particular manner. At low dimension the property (electrical, mechanical, optical) of the material changes, this properties are very different from the material at the bulk scale. Hence, we can say that the properties of the material changes when the dimension is reduced. Even we can see materials having semiconductor, insulator, metal property in contrast to the bulk property of the material. For the nanomaterials the surface area is high compared to the bulk material, hence one can say that surface to volume ratio is high compared to bulk material. This is the reason why we find interesting property at nanoscale level.

1.3 History of nanoscience and technology

Chapter:1 Introduction

Application of Nanotechnology was first demonstrated by romans in fourth century AD, which demonstrated one of the interesting example of the application of nanotechnology. Lycurgus cup from British museum collection is one of such examples. This is an example of dichroic glass which means it shows different color during different lighting condition. The glass appears green upon shining of direct light and red-purple when light shines through the glass.



Fig.1.2 The lycurgus cup the cup appears to be green upon reflected light and purple upon transmitted light[3]

In the recent TEM studies show that it performs the phenomenon called dichroism. The observed dichroism is due to presence of nanoparticles with diameter 50-100nm. The Au nanoparticle produces a red color as a result of light absorption. The red colour is due to the absorption of bigger particle and green light is due to the light scattering by colloidal dispersion of Au-Ag nanoparticles.

During 9th-17th centuring Islamic world made several wonders using Ag-Au nanoparticles in the ceramic glazes[4]. Several renaissance time pottery has been made by the Italians [5]. This type of pottery has been made for several hundreds of years however the forgers did not know the real reason behind the enchanting colour effects.

Chapter:1 Introduction

In recent times, 1857 Michael Faraday studied the preparation and interesting properties of Ruby colloidal suspension. and he showed how the solution shows different colour during different lighting condition[6].

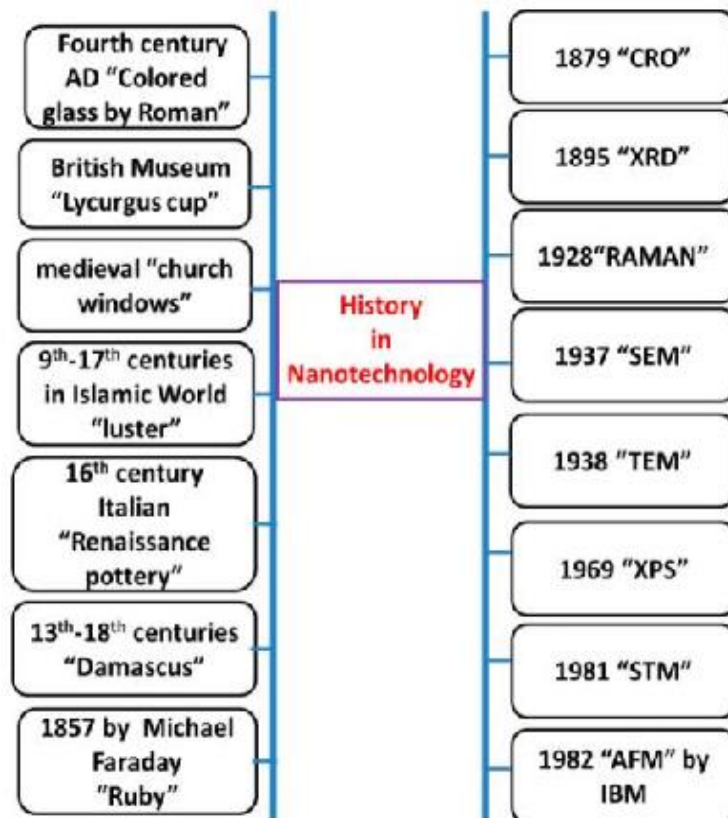


Fig.1.3 History of nanotechnology in short[7]

In modern era, two scientists from IBM Zurich research laboratory invented STM (Scanning tunneling electron microscopy)[8]. The STM uses a sharp tip which moves around the surface of the target, this sharp tip moves along the surface of the material and the wavefunction of the sharp tip coincides with wavefunction of the material. A voltage is applied on the tip for the electrons to pass through the tip to the material. STM was introduced to image the surface at the atomic level and can be used as a tool where the atoms and molecules can be manipulated. In 1986 Bining and Rohrer were awarded nobel prize for the invention of STM. During the same time Robert Curl,

Chapter:1 Introduction

Harold Kroto and Richard Smalley discovered that carbon can exist in the form of very stable spheres, named as Fullerene or buckyball[9]. In 1991 Iijima found that the Carbon Nanotubes using Transmission electron microscopy, which is a class of fullerene[10]. In 2004 a new class of materials was discovered by Xu et al. during the purification of Single wall carbon nanotube[11]. After discovery of graphene carbon based nanostructures became a very integral part of the nanoscience research. In the mean time electrical engineers have been able to miniaturize the circuit element to small scale level.

In current years there has been huge interest in nanoscience and nanotechnology in the field of biology. Recently, a number of studies have been done which showcases the huge potential of nanoscience and nanotechnology in the field of health-care, biomedicine as a cure of disease and its diagnosis[12]. Recently application of biotechnology in the biology related fields such as diagnosis, drug delivery and molecular imaging is now extensively being researched. Nanomaterials have been used in the application of drug delivery, regenerative medicine and molecular imaging. In the recent times the most innovative invention of bio-nanotechnology has been the ‘scaffolded DNA origami’, in 2006 Paul Rothemund developed it by enhancing the complexity and size of the self-assembled DNA nanostructure using one-pot reaction[13]. There has been extensive study on using bio-polymers for sensing application. Nanotechnology has impacted cancer research in many aspects, it has made cancer research more easily accessible and cheap, and more aggressive type of cancer has been treatable.

1.4 Application of Nanotechnology

1.4.1 Renewable Energy:

Chapter:1 Introduction

Energy is the most important commodity in our advancing society. This demand for energy is ever growing. Renewable energy is termed as a kind of energy which does not pollute the environment and can provide energy in the form of heat, electricity and light. Also, it is important to mention that global demand for energy to go up by 30 and 46 TW by the year of 2050 and 2100[14]. Due to the huge demand of energy and ever use of fossil fuels, environmental degradation has become a point of concern, hence there is a shift towards the use of renewable energy. Examples of renewable sources include wind, bio-mass, solar, hydrogen, geo-theermal energies. There has been huge push in this kind of energy source as it is expected to provide 50% of worlds energy by the year of 2040. Scientists refer the dimension of the nanomaterial in the range of 1-100nm. Due to the reduced size of the material , use of nanotechnology can be proven significant as it can bring down the cost of the material. Furthermore nanotechnology can be used to advance other areas related to the renewable energy, such as more higher strength material that can be developed to make lighter and more durable blades. Different material coating can be used to make the tidal energy equipment more long lasting.

Solar Cell and its Application : This is very important sector on which the nanotechnology can have huge effects. Semiconductor materials which exhibit photovoltaic effect that can be used to generate electricity from the light itself. Solar cells are extremely environment friendly. The most interesting type of solar cells are thin film solar cells which is the most researched topic. Other type of solar cells include DSSC based solar cells, Organic photovoltaic solar cell, hot carrier solar cells etc. Silicon based solar cells are expensive, as well as rigid as they are built on silicon wafers. To overcome this difficulty different kind of solarcells are being researched, perovskite based solar cells have recently drawn interest due to their efficiency. Yu and

Chapter:1 Introduction

Chen demonstrated 1D-nanomaterials which impacted the overall efficiency of the solar cell [15]. Nanotechnology can be used to enhance the photo absorption, carrier generation, electron transport and hole transport hence the whole efficiency can be increased using this.

Fuel Cells

Hydrogen is not just an energy source, it can act as an energy carrier. When hydrogen burns in the air it produces water, heat and electricity. In this process no carbon-dioxide gets produced, this does not effect global warming or any impart harmful effect to the society. The three factors deciding the fuel cell use are efficiency, size and the safe storage option for the hydrogen. Nanomaterials can be used as a membrane in the fuel cell which can easily divide the proton and electron, also can be used in catalyst and electrodes. This is due to the extremely large surface to volume ratio of the nanomaterials compared to bulk material. In spite of huge advantages it still have some drawbacks. One of the main the problem regarding the fuel cell is the hydrogen storage option. Here the application of nanotechnology can be impactful, scientist have reported that nanoblades can hold large volume of hydrogen [16], also it can be stored in CNTs [17] and Carbon Nanofibres [18]. This carbon based materials are environment friendly and cheap to produce. Some examples of different kind of fuel cells are Hydrogen fuel cells, direct methanol fuel cells.

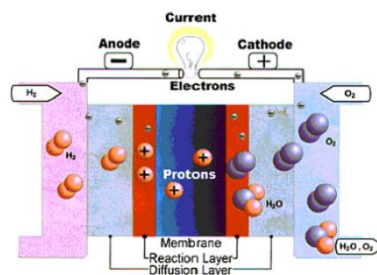


Fig.1.4 Schematic diagram of Hydrogen fuel cells [14]

Chapter:1 Introduction

Biomass and BioFuel Biomass and bio-fuel is related to the term being organic material, this type of fuel is originated from plants. Biomass is produced from plants that converts sunlight into food through photosynthesis. Biomass can be considered as a resource where energy is stored in a form of chemical bonds. During digestion or combustion when the bond is broken the compound releases energy in the form heat. Also, it can be widely available as it can be harvested in the field. Biogas is such another renewable energy source.

Batteries In modern times with the growth of portable electronic elements such as mobile phones, laptops, remote sensors, there has been rise in the need of small scale battery which can provide spontaneous energy. This aforesaid battery must be lightweight and should hold high energy density.

1.4.2 Health Care and Longevity: In the start of the 21st century life expectancy for men and women was about 48 and 51 years respectively. Now that life expectancy has increased to 74 and 80 years. With advent in nanotechnology drug delivery process can be modified. The first demonstrated drug delivery system were lipid vesicles, which later got popularized in the name liposome[19]. In 1976 better drug delivery system was reported that used complex micro polymers[20]. Later more complex drug delivery systems were invented that were capable of responding to pH for drug delivery[21]. There is many products that has been developed for therapeutic use. The current nanotechnology based products which are being used are relatively simple and lacks active targeting, also the products that lack complexity. Here role of nanotechnology comes into play.

1.4.3 Electronics and IT application: Miniaturization of computer chips has made it possible to pack huge amount of computing power in a given area. The storage of data,

Chapter:1 Introduction

processing power, creating optical and magnetic memory also depends on advancement of nanotechnology.

(i)Display: This is one of the most researched area that comes under electronics development. There is huge market for large area, high brightness, flat panel displays. Some examples of such display technologies are written below,

Field emission display(FED) and carbon nanotube based display: In this kind of technology electron emitter shoots million of electrons to hit the nanotubes, this electron emitters are made of sharp metals only activated when high voltage is applied on it. Several manufacturers are claiming that they have solved this difficulty and the technology is close to hitting the market.

Carbon nanotube Screen: In this kind of technology the metal sharp points are replaced with carbon nanotubes. The tip of the nanotubes are only 3nm in dimension.

Electrochromatic Screen: This kind of screens are sandwich of various materials. The outer layer is made up of glass substrate and inner layers are made up of electrodes, ion storing layer and the electrochromatic layer. Upon application of electricity the ions move from storing layer to electrochromatic layer, meanwhile changing the colour from dark to bright. Application of voltage results in bright spot to appear.

OLED and OTFT : This is moderately new technology named as organic light emitting diode, this technology is full of promises for a range of potential application. The basic working principle behind the OLED technology is that certain organic molecule emits light when exposed to current and this kind of technology is already being used in mobile phones, digital cameras and on TV screens. In contrast to normal LED technology OLED technology consists of a thin film of organic compounds. With more efficient and advanced technology it will be possible to make ultra thin, very bright and power saving OLED screen. In contrast to the other technologies OLED requires very

Chapter:1 Introduction

less power. Since they are thinner and light, it can be printed on almost any substrate. Application area where nanofabrication and nanotechnology can improve the overall efficiency of the OLED is the electrode. Recently researchers have found out a way to replace ITO on the OLED technology with Graphene oxide as it can become flexible and more efficient[22]. Nonetheless exciton quenching and photon loss process still limits the efficiency of this technology.

(ii)PN Junction Diode: PN junction diode is one of the most simplest semiconductor device around, and it has characteristics of passing current in one direction only. Although in contrast to resistor the diode does not behave in a linear manner. As a replacement of silicon based P-N junction diode scientists have created a CNT based diode[23], they used a single nanotube and doped electrostatically. This device can work as diode or BJT. For low bias condition they demonstrated that the diode can achieve ideality factor of 1.

(iii)Memory Storage: Advancement in nanotechnology has enabled the FET level architecture to be scaled down, recent advancement in lithography technique has enabled such feat. The computer memory which is built on solid state device technology is called flash memory. Different semiconductor manufacturing companies use nanofabrication technique to scale down the each memory unit size. Currently manufacturers are using 7 nm-10 nm technologies to fabricate memory element devices. Researchers have demonstrated vertical memory cells or vertical flash transistors. The main idea being stacking the transistors vertically, with the potential of increasing the memory density[23]. The total density can be increased 8 to 16 times in normal transistors. Hewlett packard developed a memory device that used titanium-di-oxide based nanowires[24]. A group of these nanowires are deposited parallelly to each other, when a nanowire is laid over this group of nanowires in a perpendicular manner, a circuit

Chapter:1 Introduction

element memristor was formed at the junctions. This circuit element called memristor can be used as a memory storage device in a integrated circuit. Researchers predicted that by reducing the diameter of the nanowires and closely packing them can cause more memory cells can be formed. Hp is currently working with Hynix Semiconductor to make this kind of memory technology market ready, this type of technology is called Resistive Random Access Memory (ReRAM).

Scientists from IBM have developed a new kind of memory device in which they used magnetic nanowires, made of an alloy of iron and nickel. They were able to create dense memories using these nanowires. Researchers at IBM have developed a way to magnetize a section of these nanowires. By applying a current they were able to move the magnetization along the wire. As the magnetized section move along the wire, the data is read by a stationary sensor. This method is called race track memory because data races by stationary sensors[25]. Scientists are trying to make hundreds of millions of this U shape race track nanowires on a silicon substarte to produce lowcost, high density and reliable memory chips.

Another group from Rice University have found that Silicon dioxide can be used as a memory device[26]. The nanowire was sandwiched between two electrodes, upon application of voltage on the nanowire particular location in the nanowire resistance changes. And that location can be identified by the two electrodes nearby. To create more dense storage to save up more information researchers from North Carolina State University have grown attays of magnetic nanoparticles called nanodots[27], which are about size of 6 nm. Each dot can store data by the notion that they are magneized or not.

(iv)Optoelectronics: Light travels faster than the electron, hence in this data driven society fast communication is must for daily life. From the name itself one can

Chapter:1 Introduction

recognize that any optoelectronic device can convert electrical signal into light for data transmission. Some of the example of the optoelectronic devices are 1. Photodetectors 2. Photovoltaic Devices 3. Light emitting diodes 4. Flexible devices.

(v)Nanosensors and Devices: Nanotechnology plays an important role in developing sensor technology. Nanosensors have application in many industries among them are transportation, communications, building and facilities, medicine, safety, national security etc. Researchers have reported nanowire sensors that can detect chemicals and biologics[28]. A group from Georgia Institute of Technology made world's smallest balance by taking advantage of the unique electrical and mechanical properties of carbon nanotubes[29]. They are able to mount a single particle on the end of CNT and applied electric charge on it. Acting much like a string, the CNT vibrated, the frequency was calculated from the change in the vibrational frequency from the base. This allowed the particle mass to be measured. Cleland and Roukes at the California Institute of Technology reported the fabrication and characterization of a working submicron mechanical electrometer. This device has demonstrated charge sensitivity below a single electron charge bandwidth ~ 0.1 electrons/ Hz at 2.61 MHz [30].



Fig.1.5 A nanometer scale mechanical electrometer consisting of following things a torsional mechanical resonator, a detection electrode, and a gate electrode used to couple charge to the mechanical element[30].

Chapter:1 Introduction

Various nanotube based sensors have been employed in the past few years. In the past Modi et al. developed a small scale gas detector based on CNT [31]. Nanotechnology also enables very selective and sensitive detection of bio-molecules. By sequential reduction of metal ions we can create cylindrical rods madeup of metallic cyllinders of 50 nm- 5mm long[32].

1.5 Synthesis of Nanomaterials

There are different ways of manipulaing the size of the matter at nanoscale. The two most popular methods are top down approach and bottom up approach.

The top-down approach signifies the method in which the bulk material is etched away in smaller dimension to get the required smaller structure and this is generally done via lithographic processes. In which the bulk material is sliced into smaller sizes to get the required structure. In contrast the bottom-up approach signifies the structure being built from atom to atom and molecule by molecule through covalent bond, or molecular molecular interaction in a simmilar manner how a house is built from ground.

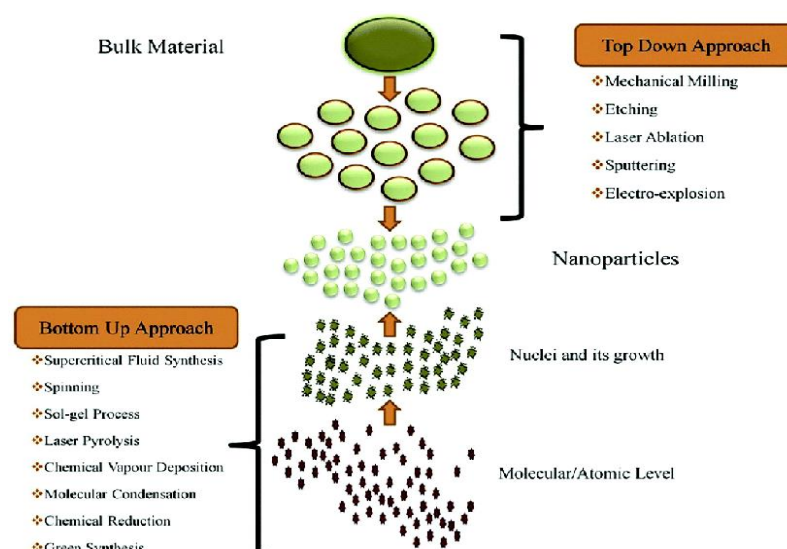


Fig.1.6 Top down and bottom up approach[32]

Chapter:1 Introduction

Different top down approaches are mechanical milling, electrospinning, lithography, sputtering, arc discharge method, laser ablation method etc. Some examples of bottom-up approaches are chemical vapour deposition method, solvothermal and hydrothermal methods, the sol-gel method etc. Also, we can see self-assembly of the material in the nature. We can see the properties of self assembly in the nature it self, it can happen in both organic and inorganic material. This structures can be generated via non covalent interactions. Currently self assembled nanotechnology is finding the area of application in the area of nanotechnology, bioscience, biotechnology.

Both approaches are very important in the nanotechnology, there are advantages and disadvantages in both approach. Milling is a typical top-down approach in making nanoparticles whereas colloidal dispersion is a good method for bottom-up approach.

Self Assembly

One popular method for bottom up approach is self assembly. Self-organizing processes are common throughout the nature, this is the process through which protein folding happens also the planetary scale movement is done. Hence the scale of the process is very broad. The key to use this self-assembly process into a controlled and direct fabrication process lies into designing the components that is required to make the patterns.

1.6 Types of Nanomaterials

Nanomaterials are generally classified depending upon five different factors, nanoparticle geometry, morphology, composition, uniformity, and agglomeration.

Based on nanoparticle geometry they are classified as 0D, 1D, 2D, 3D.

- 0D Nanomaterials are the simplest block that can be used as basic building block to make other dimension nanomaterials. This can be used to form other dimension nanomaterials.

Chapter:1 Introduction

These are generally equiaxed nanoparticles, nanogranules and nanocrystals. Generally this has dimension of maximum 100 nm. Quantum dots, nanoparticles, nanoclusters correspond to this group.

- 1D structures have only height as a dimension and that too in nm range. Carbon nanotubes, nanowires corresponds to this group.
- The 2D materials have two dimensions. This kind of materials have very low width of very thin layers. This thin layers could be in the dimension of 1-100 nm. Nanosheets, Nanoplates corresponds to this kind of group.
- The 3D nanomaterials are the materials that are not confined in the any dimension. This class contains bulk powders, dispersion of nanoparticles, bundles of nanowires and nanotubes with multiple wall.

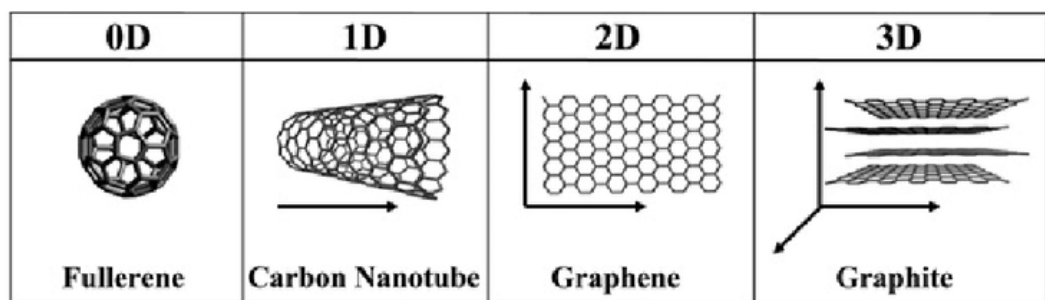


Fig.1.7 0D, 1D, 2D, 3D form of Carbon Nanostructures [33]

This dimension effect novel properties of materials due to quantum size effect. This effect changes the density of states even bandstructure of the material, transforming insulators into semiconductors even semiconductors to metals, non-magnetic element into magnetic. This quantum size effect can be realized by confinement of electron in the small dimension. When the electrons are trapped in the small confinement the energy states become discrete, hence give rise to many novel properties. Easier way to imagine this quantum confinement as a particle in the box problem in quantum mechanics. Thus both position of energy states and change in distribution of electronic energy states leads to change in effects such as increased

Chapter:1 Introduction

bandgap in semiconductors or lowering of the bandgap in semiconductors, ferromagnetic behavior, surface plasmons in the metal. Properties influenced by quantum size effect shows a discontinuous behavior due to the discontinuous nature of the filling electrons in the energy state level. The overall behavior of the bulk material changes when the dimension is reduced. In case of 0D the electrons are confined, there could be no free movement at all. For 1D material electrons are confined but are capable of moving along one direction. Same as for 2D case the electrons are capable of moving along the plane but are confined along the thickness. In case of 0D material the electrons are fully confined in the material. Also, in case of 3D materials electrons are fully delocalized.

Density of states for 3D momentum k space can be written as,

$$g(k) = \left(\frac{l}{2\pi}\right)^3 4\pi k^2 dk \dots\dots\dots (1.1)$$

$$g(E)dE = \left(\frac{l}{2\pi}\right)^3 \times 4\pi \times \frac{\sqrt{2m}}{\hbar} \times E^{1/2} dE \dots\dots\dots (1.2)$$

For 3D material we can write that,

$$g(E) \propto E^{1/2} \dots\dots\dots (1.3)$$

For the materials density of states vary as

$$g(E) \propto E^{\frac{d-2}{2}} \dots\dots\dots (1.4)$$

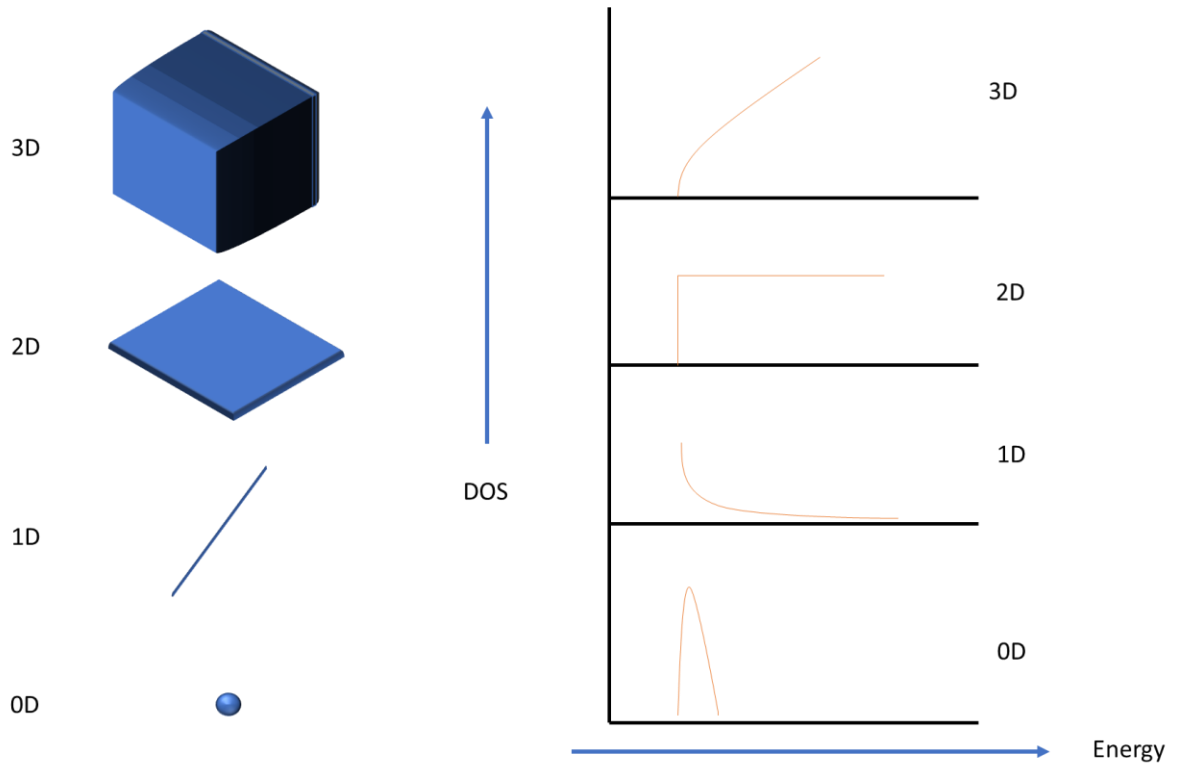


Fig.1.8 Density of states depending upon the dimension of the materials

1.7 Topological Insulator

A topological insulator is an insulator which behaves like an insulator in the bulk state but behaves like metal in the surface state. Hence the material has a conducting state on the surface, the electrons only move along the surface and an insulating state. All band insulator has a forbidden energy gap in the which it restricts the electron to move from valence band to conduction band. But topographical insulator is different from other insulator in topographic sense.[34]

With advent of physics and the discovery of quantum hall effect the hall conductance was discovered. This discovery led to measurement of quantized conductance. The first quantum spin hall effect was reported by Charles Kane and Gene Mele, they modified an reported model for graphene by F.Duncan and M.Haldane., The Kane and Haldane model is made for graphene. Topological insulator like an ordinary insulator has a bulk

Chapter:1 Introduction

energy state separating the highest band from lowest energy conduction band. But the surface state or edge state has a time reversal symmetry. The topological insulator is however closely related to the integer quantum hall state. This gap less edge state is not similar to 1D or 2D electronic system. These states are theorized to have special properties which can be useful in different applications such as quantum computation to spintronic application.

The concept of this topological order[35] is useful for characterization of intricately correlated quantum fractional quantum hall states[34], this requires many body approach to understand [36]. Due to presence of a single particle energy gap, electron-electron interaction does not modify the above-mentioned edge state. It is interesting to find that topological insulators can be explained in the context of band theory of solids. In this thesis we have worked on Bi_2Se_3 based two-dimensional topological insulator, that is second generation topological insulator. Any exotic states can occur on the boundary of the topological insulator due to an induced energy gap. Such energy gap can be induced by magnetic field or by taking the material near to a topological insulator which can show magneto-electric effect. Or by taking the topological insulator close to a superconductor can yield majorana-fermion, which may provide new venue for quantum computation. Quantum hall states belong to a topological class which explicitly breaks time reversal symmetry, via application of magnetic field. In the recent years new kind of topological insulators have been reported which are invariant to under time reversal symmetry, here spin orbit coupling plays an important role. Some important concepts were developed on 2D topological insulator where depending upon the previous work [37-39], also development of quantum spin hall effect by Bernevig and Zhang [40].

Chapter:1 Introduction

The 2D topological insulator or QSH was first theoretically predicted in the year 2006 by Bernevig, Hughes, and Zhang [41] and was experimentally observed in the year 2009[42, 43]. A topological trivial state is considered when the thickness of the QW is less than the critical value, and topological trivial state is gained when the thickness exceeds the critical value. The 2D topological insulator is synonymously called the quantum spin Hall (QSH) insulator since the edge states carry unidirectional spin current. It can be seen from four terminal measurements that longitudinal conductance of the material is quantized to be in the range of $2e^2/h$, that is independent of the width of the sample[42].

The above conclusions can be easily understood in the historical manner with theoretical prediction and experimental observation. The concepts can be described in a little bit ordered manner on how physicists developed the concept, intertwined by the theoretical paths approached by them. The first step was taken by Haldane in the year 1988 by applying the concept of the parity anomaly in quantum electrodynamics to construct a theoretical model of the QH state on the 2D honeycomb lattice[44]. This model does not require an external magnetic field nor the associated orbital quantization and Landau levels (LLs). Around the same time, Volovik proved that helium-3A film can display a topological structure without any orbital Landau levels[45]. Also, there was a misconception around that time that quantum states cannot exist hence there was a question what kind of microscopic interaction was possible for the topological behavior. In the year 2001 Zhang and Hu constructed a microscopic model for the generalization of the QH effect in 4D[46]. A crucial ingredient of this model is its invariance under TR symmetry, in sharp contrast to the QH state in 2D which explicitly breaks TR symmetry. This fact can also be seen directly from the CS effective action in 4+1 spacetime dimensions, which is invariant under TR symmetry. With this

Chapter:1 Introduction

realization two main obstacles were removed from i.e basic TR symmetry and restriction to 2D. Because of mathematical complexity, this was not appreciated by the scientific community of that time. But it is normalized now that from this all-root state from which all TR invariant topological insulators in 3D and 2D are derived. The 4D state is called grandfather state and it has two descendant state that is 3D topological insulator and 2D topological insulator this is done via dimension reduction [47].

Now motivated by construction of TR invariant topological state scientists started to look for new kind of topological class and discovered the intrinsic spin hall effect[48]. In 2004 it was realized that the two key ideas, TR symmetry and SOC can be embedded into a new class of insulator called as spin hall insulator. The spin Hall effect in insulators is dissipation-less, similar to the QH effect. This above concept motivated Kane and Mele to further investigate quantum nature of the above said spin hall effect in the graphene[34]. Bernevig and Zhang studied the QSH effect in strained semiconductors, where SOC generates LLs without the breaking of TR symmetry[49]. Although both was not realized in practical cases, they played important roles in conceptual development. Later Bernevig, Hughes, and Zhang successfully predicted the first topological insulator to be realized in HgTe/CdTe Quantum Wells[36].

Among other materials Bi_2Se_3 is made reference due to more simple band structure and bulk band gap of .3 eV. Compared to bulk Bi_2Se_3 nanostructured Bi_2Se_3 provides more surface area to a volume ratio, which greatly increases the visibility of transport phenomenon. However particular challenge for topological insulator is that for $\text{Bi}_{1-x}\text{Sb}_x$ the bulk energy gap is small and the material contains alloying disorder and that makes it difficult to control the charge carriers and manipulate them to realize a device. The topological insulator of character BiSb led us to believe that there could be compounds of the name Bi_2X_3 ($\text{X}=\text{Se},\text{Te}$)[36]. The undoped Bi_2Se_3 is a material which is

Chapter:1 Introduction

semiconductor in nature and belongs to rhombohedral crystal structure. The unit cell contains five atoms, with quintuple layers ordered in the sequence Se(1)-Bi-Se(2)-Bi-Se(1) sequence. Electrical measurement shows that bulk of the material behaves as a large band gap semiconductor and the surface state has Dirac like band structure. Also, the robustness of the surface states have been confirmed in the bulk samples with the Angle Resolved Photoelectron Spectroscopy (ARPES)[50]. Compared to bulk Bi_2Se_3 the nanostructured Bi_2Se_3 provides more surface to volume ratio which greatly enhances the transport mechanism that can be measured.

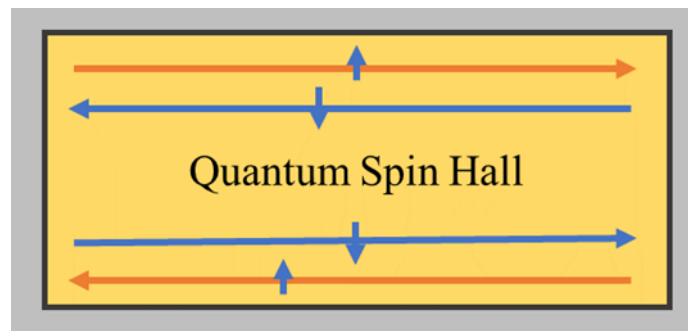


Fig.1.9 A quantum spin-hall system insulating in the bulk, they have an energy gap separating valence band and conduction band. But on the boundary, they have gapless or edgeless states that are topologically protected and immune to impurities and perturbations.

1.8 Two-Dimensional materials

Two-Dimensional material has attracted tremendous research interest following the discovery of graphene in the year of 2004. It has many application in the area such as electronics and optoelectronics and many more. The graphene can be made into atomically thin and the high surface area make it suitable for many applications. Due to the reduced size effect in the thickness, the transport of the charge carriers and heat is very much confined in 2d space leading to remarkable change in optical and electronic property. Discovery of graphene and its astonishing properties has given birth to new kind of 2D materials. At first 2D materials like graphene is known to be strong in phase chemical bond and weak inter layer coupling by van der waals forces.

Chapter:1 Introduction

These layered structures can be sliced into few layers of materials that can show interesting properties depending upon the no. of layers. Graphene is the first found 2D material and till now very interesting. It has a zero-bandgap semimetal nature, in graphene electrons are highly mobile and shows exceptional conductivity. Graphene has enormous amount of application due its intrinsic property, the kind of application range from electronic, mechanical application etc. This huge amount of application has encouraged scientists to develop new kind of 2D material. To address the point of interest the no. of 2D material library is growing day by day, till date more 150 different kind of 2D materials have been reported. 2D materials are categorized depending upon their structure other than graphene, transition metal di-chalcogenides(MoS_2 , WS_2 , MoSe_2 , and WSe_2) [51],layered double hydroxides(LDH),hexagonal boron nitride(h-BN)[52],black phosphorous, MXenes, transition metal oxides are examples of occurring 2D materials. The emergence of 2D materials like graphene has propelled the applications like sensors, LEDs, FETs, catalysis, biomedicine applications etc. Suitable bandgap semiconducting material can be used in electronics, optoelectronics and sensing application. Also, use of heterostructures can broaden the band gap range hence allowing different kind of application possible. These heterostructures has certain properties that graphene and other 2D material does not possess. This heterostructures can replace Si, as Si based technology has many limitations, potential application can be memory device or solar cells etc. The exfoliation of monolayer MoS_2 was possible back in 1966 by using adhesive mechanical tape[53]. In 2010 research on TMDC gained new interest due to finding of direct bandgap MoS_2 [54].

For simplicity TMDC can be explained in this notation, MX_2 where M is transition metal (Mo, W, Re, or Ta) and X is a chalcogen family element. The most well known TMDCs are the W and Mo based chalcogenides i.e, WS_2 , WSe_2 , WTe_2 , MoS_2 , MoSe_2 .

Chapter:1 Introduction

More than 30 kind of TMDCs have been reported using different synthesis method. 2D TMDCs have electron carrier mobility of $\sim 200 \text{ cm}^2\text{V}^{-1}\text{s}^{-1}$ with BG of 1-2 eV in the visible range. In the electronic device application this devices are used as high switching applications, and low power applications. Though implementation of single layer MoS_2 as a main device substrate has been quite hectic, in 2011 B.Radisavljevic et al. [55]fabricated a single layer MoS_2 single layer device, the most widely used 2D material is graphene but for pristine graphene the band gap is zero. But this property is essential for transistor like application. But the single layer of MoS_2 has a bandgap of 1.85eV also previously reported mobilities are too low for device-based application. Here authors used hafnium oxide as gate di-electric and using they have demonstrated a mobility of at least $200\text{cm}^2\text{V}^{-1}\text{s}^{-1}$. The electronic structure of TMDC depends sensitively on the crystal phase and bears the characteristics like metallic, semi-metallic, semi-conducting, super-conducting for different kind of TMDCs[56, 57]. The TMDCs based on group VB and VIB metals are heavily studied due to their stable characteristics and stable electronic structure. Mobility of the 2D material increases with the no. of layers for the first few layers but decreases upon the increase of the interlayer resistance keeps building up. This group also demonstrated suitable logic operation by stacking multilayer of Si substrate on the MoS_2 [57]. Some layered TMDCs like Bi_2Se_3 have long been studied as thermoelectric material but now is found to be topological insulators (Conducting phase at the surface and core remains insulating). The TMDCs based on VB and VIB are heavily studied due to their excellent stable electronic property and stability as a compound[58-60].

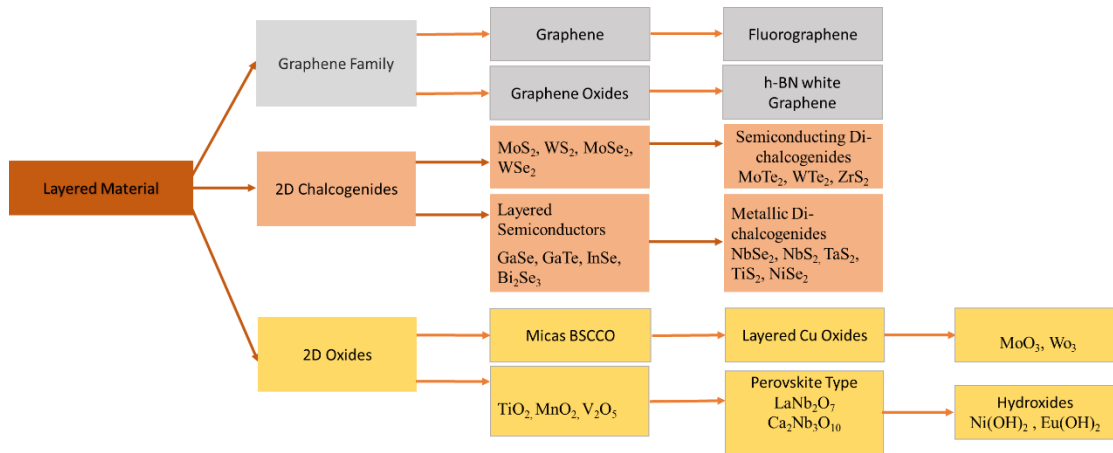


Fig.1.10 Layered material and their different classes.

In this thesis the 2D Bi_2Se_3 is synthesized and used for device application. The solvothermal synthesis of Bi_2Se_3 nanosheets is very easy and cost-effective method.

The 2D Bi_2Se_3 is explored for various applications like Photodetector[61], Resistive Switching device[62], low macroscopic field emitters for cold cathode application[63], photocatalysis[64], Tetrahertz frequency detection[65].

In 2017 Biswajit Das et al. experimented with topological insulator Bi_2Se_3 nanoflakes and Si-nanowire heterojunction photodetector. The process involves eco-friendly route, authors identified the phase using XRD and studied morphology using FESEM. High resolution TEM is done to study the elemental distribution nature of the junction. Authors also have experimented with temperature dependent current voltage characteristics; variation of barrier height and ideality factor were studied between 50 to 300K. They have observed increase in barrier height and decreases in the ideality factor with increasing temperature. They found the rectification ratio(I_+/I_-) for Si-NW substrate over pristine Si substrate under dark and near infrared irradiation of 890 nm was found to be 3.63 and 10.44. Those value reported are higher than previous reports

Chapter:1 Introduction

of any other topological insulator-based device. This work establishes Bi_2Se_3 and Si-NW heterojunction as a new candidate for opto-electronic application.

In 2018 Biswajit Das et al. experimented with Bi_2Se_3 nanoflakes embedded in PMMA solution for resistive switching application. Hexagonal 2D Bi_2Se_3 nanosheets has been synthesized by simple solvothermal method and was combined with different percentage in PMMA solution. FESEM, TEM, XPS and Raman Spectroscopy was done on Bi_2Se_3 and PMMA hybrid solution. The composite was deposited on transparent flexible PET substrate to form $\text{Ag-Bi}_2\text{Se}_3\text{@PMMA-ITO}$ memory cell. I-V characteristics of the device showed stable and non-volatile memory. The device shows high resistance ($R_{\text{HRS}}/R_{\text{LRS}}$) ratio, more than 10^3 , high retention time (more than 9000 s) with high reproducibility (10^5 ac cycles). The authors have concluded that RS performance is explained by charge trapping-detrapping method. They have also measured the flexibility of the device, and it turned out to be flexible enough.

In 2020 Shengqian Liu et al. fabricated a low cost, flexible photodetector for practical application[66]. Authors fabricated the device using pencil drawing method on a paper substrate. As Bi_2Se_3 is light sensitive material, it shows high photocurrent and long stability under 1064 nm infrared light. The device is made using flexible paper substrate hence it shows durability and stability under bending condition. Their work proposed a way to fabricate novel flexible infrared photodetector with facile manufacturing process and low cost.

There has been many device related application incorporating Bi_2Se_3 nanosheets. In this thesis work Bi_2Se_3 based pressure sensor and SSPM of the Bi_2Se_3 nanosheets have been explored.

1.9.1 Introduction to Pressure Sensor

Chapter:1 Introduction

Internet based medical and health data acquisition system is growing very rapidly. Accurate diagnosis of the health issues is very important in present time and wearable sensors are producing a pathway for this kind of development in the field. Doctors can help the patient with the routine according the data analysis done on the gathered data recorded by the wearable sensor. To obtain these data, repeated and continuous operation of sensor is required. Doctors can also recommend medicine according to the analytics done on the data. This the sole reason big data is a growing field today. Pressure sensor, photoelectric sensor, temperature sensor has been developed to monitor biological data such as blood sugar, heart rate and blood pressure etc.

Also, there is large amount of data involving personal habits stored inside the sensor hence it is necessary to have hardware security so that it cannot be accessed by another user. The use of wearable products such as smartwatches and bracelets are on the rise. In the future thin wearable sensor or implantable sensor will become breakthrough point as they will become thinner and very efficient.

Pressure sensor plays an important role in wide range of applications such as diagnostic health monitoring to precision surgery. Next generation monitoring device are now being used to measure certain biological activities such as health status, blood flow[67], tendon repair, heart rate monitoring, pulse rate determination.

With the ever-increasing demand of pressure sensors there is need of pressure sensors showing great sensitivity, dynamic range, response time and relaxation time. Sensitivity is defined as the relative change in output signal compared to input signal. Quantitatively the sensitivity defined as the change in output signal divided by change in input signal. Ideally a pressure sensor should have high sensitivity so that it can show output in

Chapter:1 Introduction

occurrence of change of pressure. The range in which the pressure sensor should operate is called the dynamic range[68, 69]. Response time and

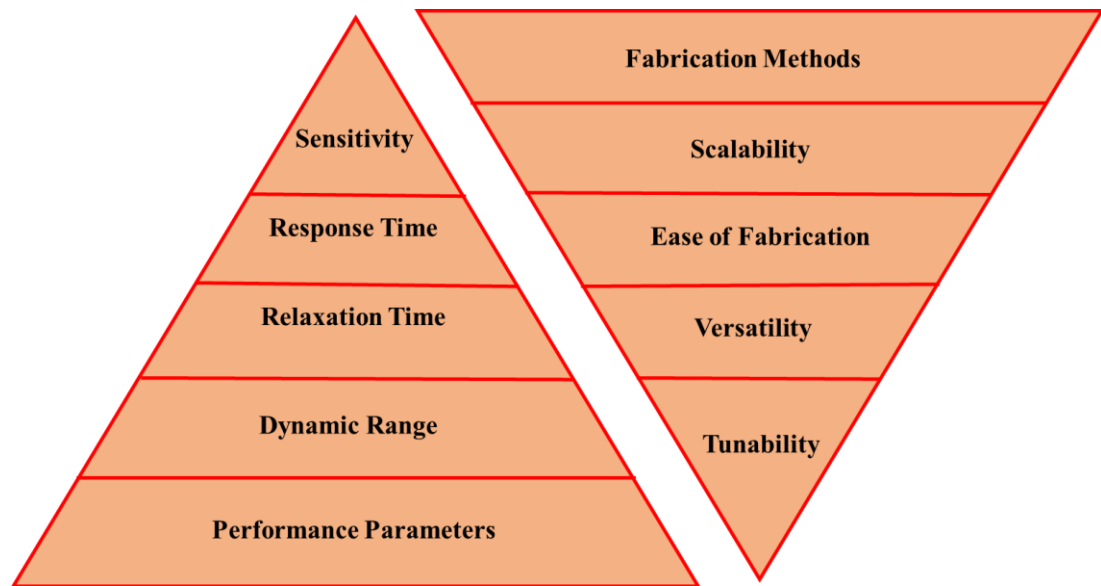


Fig.1.11 Necessary attributes of a performing pressure-sensor.

relaxation time are two key parameters, determining the speed at which the pressure sensor will be able to detect a signal. Low response and relaxation time is mandatory parameters for an ideal pressure sensor. As of now different pressure sensors have been reported operating on different working principle, and they are capacitive, resistive, piezoelectric, triboelectric etc. For each sensor type there is different operating principle, they will be discussed in below.

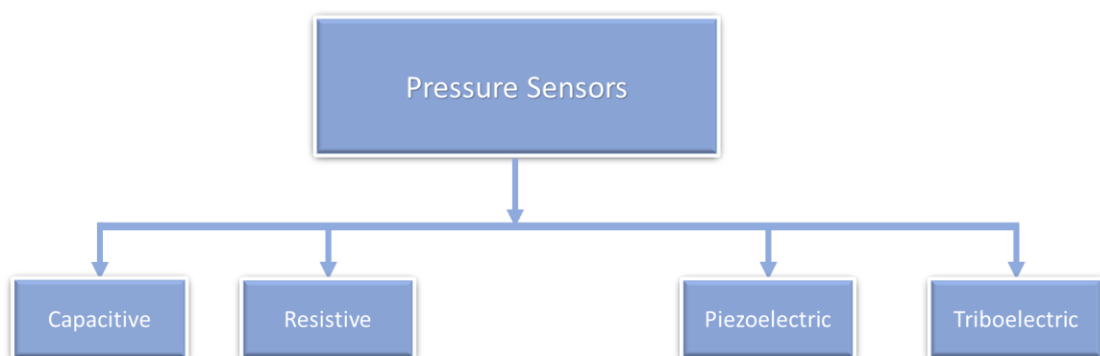


Fig. 1.12 Different kind of pressure sensor and their classification.

1.9.2 Pressure sensor classification according to their performance parameters and fabrication methods

Different kind of Pressure Sensors

3.1.1 Capacitive Pressure Sensors

A simple capacitor is made of two metal electrode and between them a dielectric is existent. A Capacitive pressure sensor works using simple capacitor formula, where ϵ is the permittivity of the dielectric, A is area of the plate capacitor and d is the distance between the two plates of the capacitor.

$$C = \epsilon A/d \dots\dots\dots(1.5)$$

When an input signal is provided to the capacitor the capacitance changes indicating change in the system, and this can be calculated using external probing machine. External pressure could change the displacement of the elastic material, thus via incorporating nanostructures it is possible to introduce a change in effective area or the distance between two parallel plate capacitor. The change in current can also be calculated, via an external probing machine. It is also possible add filamentary substances in the dielectric where change in di-electric can also sense the pressure. Also, capacitive pressure sensor is easy to fabricate and shows great response time upon application of external voltage[70]. This type of sensor is capable of working in different region of temperature also it is capable of showing low power consumption as a sensing device. Selecting appropriate materials can improve overall quality of the pressure sensor also can add qualities such as flexibility, linearity and faster response time[71, 72].

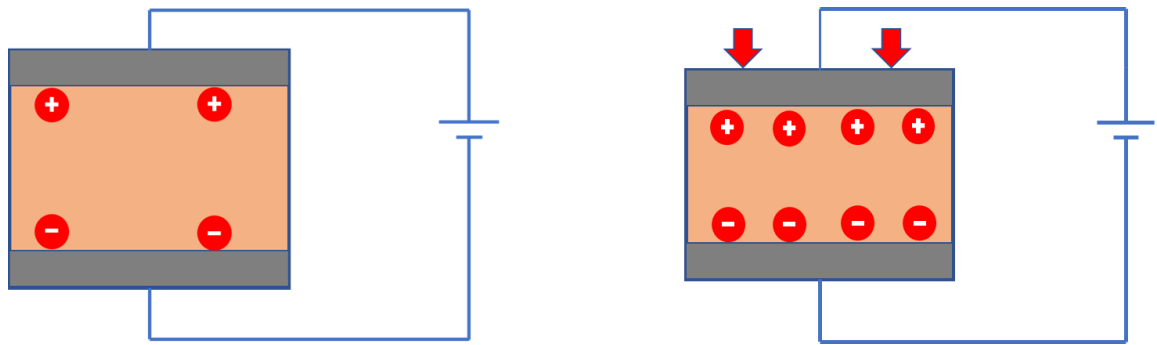


Fig.1.13 Working of Capacitive pressure Sensor application of pressure changes the capacitance, that quantifies the applied pressure.

A popular approach for increasing the efficiency of the sensor is micropatterning of the dielectric material. By this way the capacitance can be readily increased, through this method many experiments have been run[70, 73, 74]. When pressure is applied on the sensor, it can internally distress the inward structure of the dielectric material, hence by adding void to the dielectric medium, so that the sensor can be easily compressed. Mannsfeld et al. fabricated a pressure sensor employing flexible PET/ITO as a substrate that also work as an electrode, also a microstructure silicon rubber as an di-electric material[73]. Peng et al. made a capacitive array where they have used PDMS as a substrate material, here the sensor can detect subtle change in pressure as the substrate gets compressed[75]. Zhuo et al. showed that the PDMS substrate can be used di-electric material, while the micro structured pattern in the PDMS substrate enhanced the sensory capability of the device[76].

(i)Resistive Pressure Sensor

In case of resistive pressure sensor, the internal composite or material embedded fabric is distorted via application of force, this application of force can effect a change in current flowing through the sensor. This force indirectly changes the conductive filler inside the electrodes, this distortion changes the resistance of the device. This type od

Chapter:1 Introduction

sensor does not require the heavy power consumption also have the advantage of ease of fabrication.

This kind of pressure sensor works according to the ohm's law.

$$R = \rho l / A \dots \dots \dots (1.6)$$

Here R is the resistance between two electrodes, ρ is the resistivity, l is the length and A is effective area between two electrodes.

Different kind of pressure sensor has been studied, commonly studied structures include metallic particles, metal nanowire, carbon based materials like Carbon Black, graphene, CNTs and reduced oxides(rGO)[77].

Kim et al. produced a structure in which vertically aligned MWCNT is embedded in to PDMS substrate[78]. In recent years different kind of sensors are being studied, depending upon the material used and the microstructure required.



Fig.1.14 Working of piezo-resistive sensor, here application of pressure changes the substrate resistance hence make measurement of pressure possible.

Chen et al. fabricated a sandwich like structure in which the encapsulated material, using micro-structured electrode and PET/ITO film[79]. In the same year Zhang et al. produced a pressure sensor via incorporating silk like microstructure in the PDMS substrate[80].

(ii) **Piezo-electric Pressure Sensor**

Flexible piezo-electric pressure sensor is easy to fabricate, easy material collection, easy signal generation and other positive merits. This kind of pressure sensor is made of materials which converts electrical energy into mechanical energy and vice versa. Upon application of pressure or force a charge separation occurs in the material, this negative and positive charge is aligned opposite to each other and a potential difference will be formed on the outside of the material. This potential difference can drive a circuit, which in return can sense the value of pressure applied. This potential difference is studied to examine the applied pressure on the sensor.

The operation of Piezo-electric sensor can be described using Hooke's law integrated with electrical behavior.

$$S = sT \dots\dots\dots(1.7)$$

Here S is strain, s is the compliance and T is the applied stress.

$$D = \epsilon E \dots\dots\dots(1.8)$$

Here D is the electric charge density, ϵ is the permittivity of the dielectric medium and E is the electric field.

This equations can be linearly approximated to,

$$S = s^E T + dE \dots\dots\dots(1.9)$$

And also can be written as, $D = dT + \epsilon^T E \dots\dots\dots(1.10)$

This suggests that strain will result in piezoelectric output. The main advantage of the piezo-electric sensor over other sensor is that it does not require another power source

to operate. The performance of piezo-electric pressure sensor can be modified via incorporating microstructures.

Also, emergence of new kind of piezo-electric material is the new driving force behind fabrication of such device and newly reported finding. Materials such as P(VDF-TrFE), Barium Titanate BaTiO_3 , lead Zirconate-titanate (PZT) and oxide material like ZnO. This kind of material is advantageous over other materials for their easy fabrication, high piezo-electric coefficient, simple manufacturing. Persano et al. fabricated a device in which they synthesized P(VDF-TrFE)nanofiber arrays in simple electro-spinning method[81]. This device is capable of detecting low pressure in the region of 0.1 Pa, also it shows fast response. Akiyama et al. experimented with device that deposited AlN film on PET substrate[82]. They also showed that the operating range of such device is in the range of 0-8 MPa at room temperature.

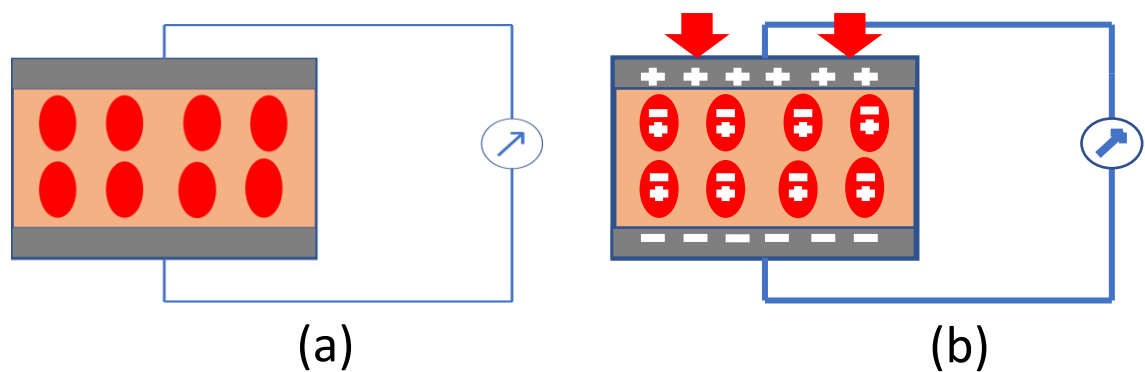


Fig.1.15 Working of a piezo-electric pressure sensor, upon application of pressure voltage is generated as seen in (b), where application zero pressure results in generation of no voltage as can be seen in (a).

(iii) Triboelectric pressure sensor

Triboelectric nanogenerators have drawn particular interest due to the promising nature of the material and ease of fabrication. Triboelectric generators offer different kind of

Chapter:1 Introduction

mechanism to the piezoelectric sensors. Triboelectric generators are based on coupling effect of the contact and its electrification and electric induction. The working principle of triboelectric pressure sensor is similar to that of triboelectric nanogenerator. This kind of pressure sensor is high in demand due to ease of fabrication, low cost, ease of fabrication etc. Das et al produced a triboelectric generator using PDMS substrate, they were able to micropattern it using commercially available sandpaper[83].

2D materials are layered materials where every single layer is few atom thick and can be isolated using exfoliation methods. These layers are bound together following weak van der Waals force, this allows sensor to have unique optical, electrical property. There have been instances where 2D based sensors have outperformed traditional sensors in different properties. There are several 2D materials have been found till today, among them Bi_2Se_3 is quite popular, and there has been no report of it as a pressure sensor application.

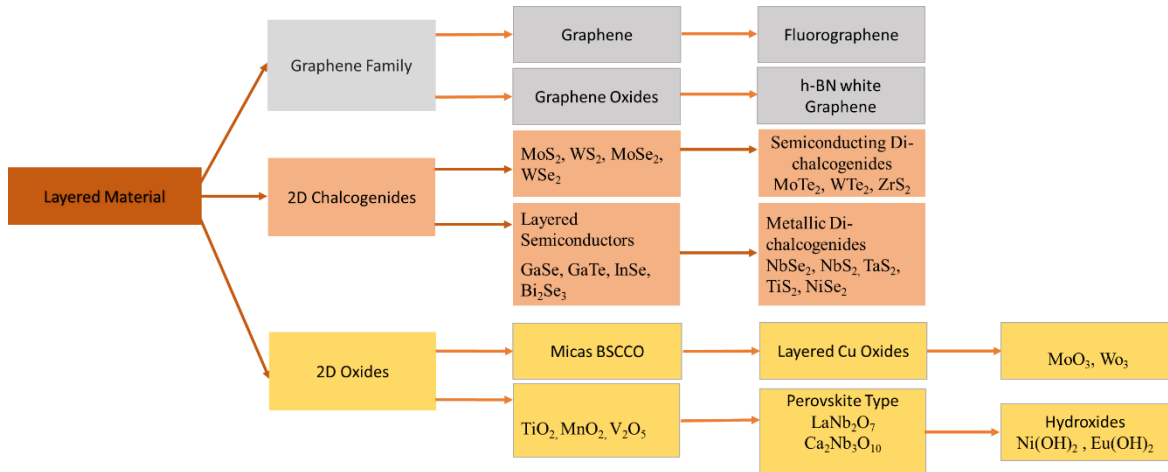


Fig.1.16: Layered material and their different classes.

In the thesis, pressure sensing application of Bi_2Se_3 is discussed

In this thesis we broadly discuss piezoresistive pressure sensor and its application and the application of 2D material. Silicon based piezo-resistive pressure sensor is widely

Chapter:1 Introduction

used and its measuring element is Wheatstone bridge. When under pressure the electrical resistance changes, this is called piezoresistive effect. The pressure to be sensed is measured by a silicon chip via a membrane and incompressible silicone oil. A piezoresistive sensor contains several thin film of wafer of silicon on the protective surface. The surfaces are generally connected with Wheatstone bridge, a small change in pressure will induce current in the device leading to output. Which indicates change in pressure.

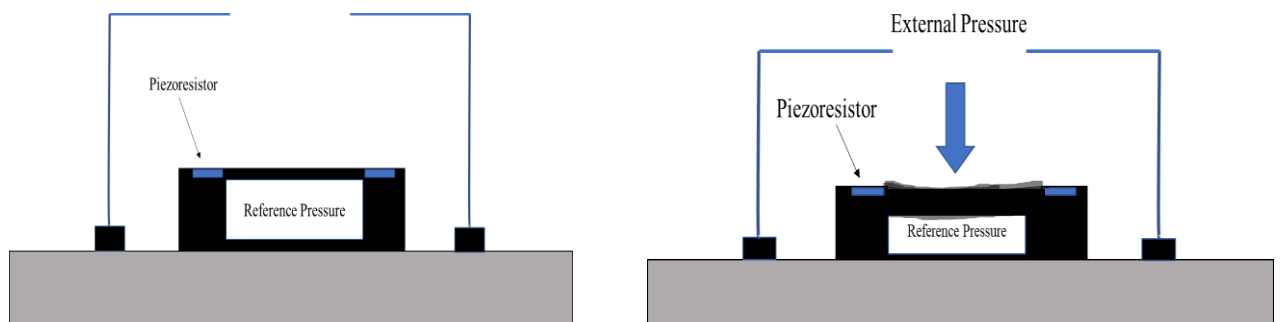


Fig.1.17 With application pressure there is bending in the piezo-resistor and there is change in resistance which is recorded in the output

The change in electrical resistance due to mechanical load was first discovered by Lord Kelvin in the year 1856. In conducting or semi-conducting material, the change in inter-atomic spacing results in change in the bandgap, making it easier for the electrons to hop to conduction band hence the change in resistance occurs. As described in the above type of device the change in conducting valley pairs which directs effects the effective mass of the electron. Hence change in the mobilities is seen on the direction of current flow. Same can be seen in case of Bi_2Se_3 based pressure sensor. Presence of selenium

Chapter:1 Introduction

causes it to be n type material. When pressure is applied two thin layer of nanosheets come together, hence their interatomic distance changes leading to a decrease in bandgap, this decrease in bandgap changes the electron mobility in the direction of the current. In this thesis we have worked on pressure sensor on flexible substrate capable of bending at will. This flexibility gives edge over the traditional silicon-based pressure sensor which is bulky and not wearable. Whereas our work on pressure sensor shows good repeatability and flexibility over time.

1.9.3 Application of Pressure Sensor Device

(i) Automobile Application: In automobiles the hydraulic brakes are crucial component that ensures the safety of the passenger. Pressure sensor can be used to monitor the pressure in the pressure chambers of the braking system. It is necessary to know the pressure inside the chamber otherwise the chamber will fail.

(ii) Life Saving Medical Application: Pressure inside a chamber can be raised containing the patient, this therapy is called hyperbaric therapy. It is used for treatment of various kind of medical conditions such as burn injuries, skin grafts, carbon-monoxide poisoning. For monitoring of this kind of chamber pressure sensor is necessary. Measuring blood pressure is crucial to patient care, now pressure sensor can be implanted inside the body to measure the internal pressure, this is called in-vivo blood pressure sensing.

(iii) Life-enhancing Consumer Application: The things we carry and wear on daily basis are increasing day by day. Addition of pressure sensor to this appliances can improve their user experience.

It can be used as heart rate monitoring device when attached to textile and placed near a vein. It can detect pulse and monitor the health of the user. The pressure sensor can

Chapter:1 Introduction

be used as e-skin for voice detection purpose. Coupled with other devices it can be used for tactile perception, this application can be used for morse code generator and other IOT devices. Taking vacuum cleaner as an example, the suction change should be monitored for cleaning purpose.

(iv) Automated Building Application: Recently with advances in IOT applications, smart home system applications are getting popular. Adding pressure sensors to the devices can make the device attain perception of spatial awareness which can enhance the attributes of the devices. Pressure sensor plays an important role in refrigeration system. Common coolants in HVAC like can cause damage to the owners, application of pressure sensor can detect the fault in this type of systems

(v) Industrial Applications: Pressure sensors can be used to measure the liquid pressure of the tank. This can be used to monitor the liquid level at the tank and alert the tank workers if the level goes down from certain safe level.

(vi) Air pressure measuring principle can now be used to monitor the patient and develop assistive living solution, when a sudden change in the altitude can indicate a fall.

(vii) Pressure Sensor application in space can be a point of interest, as it is capable of measuring air pressure in hundredths of millibar accuracy of 2mbar or better. This is can have a very interesting space application.

(viii) For sports enthusiast the barometric pressure sensor can be used to determine the height under the sea-level. These sensors are generally used by scuba-divers and skydivers. Piezoresistive pressure sensor is a popular choice for this kind of pressure sensor as they are compact in size and accurate in giving the results.

1.10 Spatial Self-Phase Modulation (SSPM)

1.10.1 Introduction

Another work done in the final year thesis is the Spatial Self Phase Modulation. This is a special branch of nonlinear optics, this occurs when high intensity laser beam is incident on the homogeneous medium, a diffracted pattern of beam is found at the distance. The phase is modulated by its own intensity. Recent studies have shown that 2D materials have excellent nonlinear optical properties and ultra-fast dynamics.

Non-linear optics came to existence after breakthrough discovery of Second harmonic generation and third harmonic generation by strong optical regime. Optical nonlinearity can be described using Electrodynamics, and more precisely considering how the dipole moment per unit volume is or the Polarization of the material depending on the strength of an applied optical field (mainly on the Electric field). Semiconducting 2D material develops di-pole moment on the application of strong electric-field. This kind of polarization is possible when the exfoliated material is suspended in a solution, the laser has to be a strong laser capable of producing high power coherent light source of a fixed wavelength. The non-linear optical responses of materials to the applied electric field can be expressed by generalized power series expansion of polarization $\tilde{P}(t)$ in the electric field $\tilde{E}(t)$.

$$\tilde{P}(t) = \epsilon_0 [\chi^{(1)} \tilde{E}(t) + \chi^{(2)} \tilde{E}^2(t) + \chi^{(3)} \tilde{E}^3(t) + \dots] \dots\dots\dots(1.11)$$

$$\tilde{P}(t) = \tilde{P}^{(1)} + \tilde{P}^{(2)} + \tilde{P}^{(3)} + \dots \dots\dots(1.12)$$

Where $\chi^{(n)}$ is the n^{th} order susceptibility of the material and the ϵ_0 is the free space permittivity. The $\tilde{P}^{(1)}$ occurs due to the term $\chi^{(1)}$ is the linear susceptibility. The $\chi^{(1)}$ is the linear susceptibility which describes linear optical effects. $\tilde{P}^{(2)}(t)$ and $\tilde{P}^{(3)}(t)$ which occurs due to $\chi^{(2)}(t)$ and $\chi^{(3)}(t)$ respectively. The $\chi^{(2)}(t)$ and $\chi^{(3)}(t)$ are called second

Chapter:1 Introduction

order non-linear susceptibility and third order non-linear susceptibility. Non optical properties occur due to third order susceptibility, such as FWM, THG, Kerr Effect is related to SSPM. This effects can be calculated[84]. The third order susceptibility gives rise to self-phase modulation which can modify the incident gaussian beam profile, while it is propagating through material. This is how the non-linear optical properties of the material is measured. The time domain laser induced polarization satisfies the Electromagnetic wave equation of non-linear medium, which is given by,

$$\nabla^2 \tilde{E}(t) - \frac{n^2}{c^2} \frac{\partial^2 \tilde{E}(t)}{\partial t^2} = \frac{1}{\epsilon_0 c^2} \frac{\partial^2 \tilde{P}^{NL}(t)}{\partial t^2} \dots \dots \dots (1.13)$$

Here n is the linear refractive index, c is the speed of light in vacuum. $\tilde{P}(t)$ is a power series that converges, this value should be finite. There is a significant role of crystallographic symmetry, especially inversion symmetry for the survival of even and odd order terms in the induced polarization by an outside source. The even order nonlinear susceptibility $\chi^{(2)}$ vanishes and its higher orders or harmonics vanishes in case of centrosymmetric class of materials. The optical non-linearity occurring in centrosymmetric materials are mainly due to third order non-linear susceptibility $\chi^{(3)}$.

SSPM is mostly used to study the refractive index of the material. There is still debate, whether the whole diffraction is caused by the non-linear optical property of the material or the thermal effects caused by the laser itself. In 2011 Wu et al. observed SSPM phenomenon in a graphene solution[85]. Graphene adjusts its non-linear refractive index using energy band structure when the laser is incident on it.

Non-linear optical responses can be measured using three different methods Z scan, Four Wave mixing (FWM) and SSPM. Among the above methods first two requires complicated setups while SSPM is a quite easier process to follow. It can be used to

Chapter:1 Introduction

measure non-linear optical properties like Non-Linear Refractive Index (n_2), Third Order Non-Linear Susceptibility ($\chi^{(3)}$)[86, 87].

1.10.2 Non-Linear Kerr Effect

Non-linear Kerr effect is important effect to study non-linear optical properties of the 2D material. According to these effects non-linear Kerr effect can be written in the form of below,

Equation describing light intensity and non-linear refractive index are,

$$n = n_0 + n_2 I \dots \dots \dots (1.14)$$

here n is the refractive index, n_0 is the linear refractive index, n_2 is the non-linear refractive index and I is the Intensity of laser light.

Because of the strong non-linear Kerr-effect a phase shift is introduced. The phase has a nonlinear modulating behavior to the transverse intensity profile of the incident gaussian laser beam. A phase shift is introduced which is expressed as,

$$\Delta\psi(r) = \frac{2\pi n_0}{\lambda} \int_0^{L_{eff}} n_2 I(r,z) dz \dots \dots \dots (1.15)$$

I is the light intensity, $\Delta\psi$ is the phase shift of the laser beam, r is the radial coordinate, λ is the wavelength, L is the total effective propagation length through the sample containing cuvette, $I(r,z)$ is the intensity of the distribution. N is the total no rings formed. The ‘self’ phase shift ($\Delta\psi$) that gets modulated due to the nonlinear Kerr Effect is result of the change in optical refractive index, n as function of intensity of the coherent Gaussian laser beam. Therefore, the propagating light creates diffraction pattern of bright and dark rings.

And the equation corresponding to the bright and dark rings is,

Chapter:1 Introduction

$$\Delta\psi(r_1) - \Delta\psi(r_2) = 2M\pi \dots \dots \dots (1.16)$$

Here M is the integer and it is even or odd corresponding to the bright or dark ring.

Here L_{eff} can be calculated using the equation below,

$$L_{eff} = \int_{L_1}^{L_2} \left(1 + \frac{Z^2}{Z_0^2}\right)^{-1} dZ = Z_0 \tan^{-1} \left[\frac{Z}{Z_0} \right]_{L_1}^{L_2} ; Z_0 = \frac{\pi \omega_0^2}{\lambda} \dots \dots \dots (1.17)$$

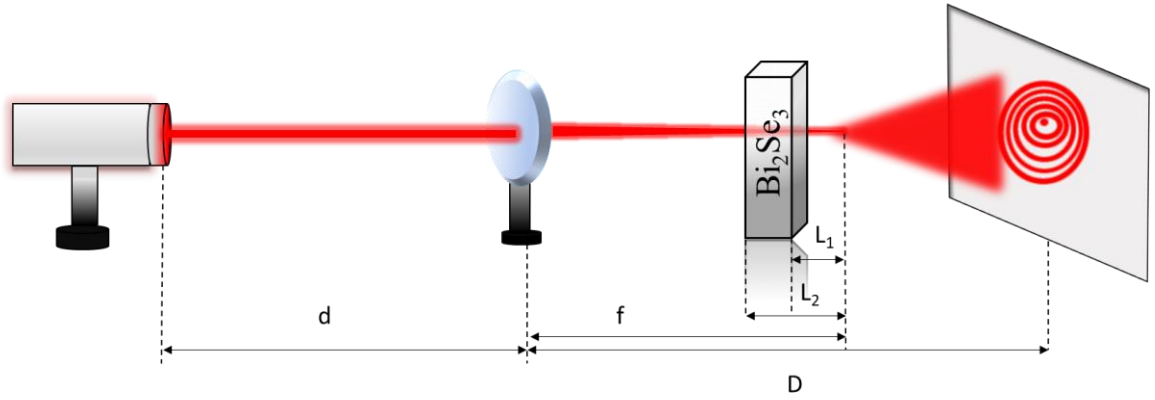


Fig.1.18 Schematic of the experimental setup and the SSPM of Bi_2Se_3 nanoflakes

Here L_1 and L_2 are the distance from the focus(f) to the side of the quartz cuvette. The central intensity profile of the transmitted gaussian beam can be expressed as $I(0,z)=2I$, where I be the average intensity of the incident laser, z_0 is the diffraction length and w_0 is the $1/e^2$ beam radius.

From the equation 1 and 3 we can conclude that the nonlinear refractive index(n_2),

$$n_2 = \frac{\lambda}{2n_0 L_{eff}} \frac{dN}{dI} \dots \dots \dots (1.18)$$

Also, we can calculate $\chi^{(3)}(t)$ from the derivation as described in [88],

$$\chi^3 = \frac{n_0^2 c}{12\pi^2} n_2 \dots \dots \dots (1.19)$$

Chapter:1 Introduction

Available number of 2D nanoflakes greatly influence the value of $\chi^{(3)}$. So, it is necessary to conclude that the $\chi_{\text{monolayer}}$ for single layer Bi_2Se_3 . For total value of χ^3 can be calculated using the formula [88]

$$\chi_{\text{total}}^{(3)} = \chi_{\text{monolayer}}^{(3)} \times N_{\text{eff}}^2 \dots \dots \dots (1.20)$$

Where N_{eff} represents effective number of layers in the cuvette.

Here dN/dI plays an important role.

1.10.3 Spatial Self-Phase Modulation: Mechanism of Light matter Interaction

In the above-mentioned non-linear Kerr effect, leading to SSPM the diffraction ring number increases with time and the n_2 and the $\chi_{\text{total}}^{(3)}$ depends upon the suspended 2D flakes on the solution. In this SSPM technique the no. of diffraction ring increases with time leading to a maximum value. The time required to reach a maximum diameter at a fixed intensity is described by wind-chime model proposed by Wu et al.[88]. This, model suggests that the intense laser beam polarizes the suspended nanoflakes of the material in the solution along the direction of the optical electric field through energy relaxation process. With time the no of ring increases as the no of the nanoflakes to get oriented in the direction of electric field. Oriented nanoflakes interact coherently with the incident laser beam. Initially a bright spot is formed with time the nanoflakes are reoriented with electric-field the full circular rings appear. According to the wind chime model the time taken to form maximum diameter diffraction pattern is the time taken for the 2D NFs to reorient themselves. The ring formation dynamics follow the exponential decay model.

$$N = A \left(1 - e^{-t/\tau_c}\right) \dots \dots \dots (1.21)$$

Chapter:1 Introduction

where N is the number of rings, A is a constant, τ_c is the rise time of ring formation.

The minimum time required for the NFs to re-orient themselves are,

$$T = \frac{\epsilon_r \pi \eta \xi R C}{1.72(\epsilon_r - 1) I h} \dots\dots\dots(1.22)$$

where ϵ_r is the relative dielectric constant of the material, η is the coefficient of viscosity of the solvent, R is the domain radius, h is the flake thickness, and I is the intensity of the laser beam

Also, keeping all the other parameters constant if we change the solvent of the material the with little bit more viscous material the time will change. Low viscous medium takes shorter time to reorient the suspended nanoflakes of the material towards the incident electric field. Hence lower the value of η the less time it will take reorient the nanoflakes.

1.10.4 Dynamics of Collapse Phenomena of Diffraction Patterns

It is observed that after reaching maximum no. of rings the upper half of the diffraction ring starts to collapse towards the center. This collapse of the upper half is due to the non-axis symmetrical thermal convection leading to the distortion of the diffraction pattern as reported by Wang et al.[89]. Also, the dispersion medium absorbs some light due to the optical absorption coefficient[90]. The temperature also increases along the vertical direction, enhancing the thermal convection process[91]. This above convection process reduces the concentration of 2D materials in the upper part of the medium than the lower part of the medium. Therefore the upper part of the laser beam is less diffracted by the dispersed 2D materials leading to distorted diffraction pattern which collapses towards center determined by the thermal convention of the medium[92].

1.10.5 Application of Spatial Self-Phase Modulation Method:

Chapter:1 Introduction

This SSPM technique can be used for optical switching. Our work demonstrates potential for Bi_2Se_3 as an optoelectronic applications such as diode application, OR Gate application. It can also be implemented in spintronic device application.

1.11 Aims and Objective of the Thesis:

1. To understand the basic theory of pressure sensor.
2. To understand the pressure sensing capability of the Bi_2Se_3 coated tissue paper.
3. To synthesize the material using cost-effective solvothermal method.
4. To develop the understanding of fabrication of the pressure sensor, using cost efficient process.
5. To adapt different mechanism to increase the sensing capability of the pressure sensor.
6. To understand different application of the pressure sensor.
7. To understand the non-linear optical response of material.
8. To calculate nonlinear optical coefficients using SSPM method.
9. To implement all optical photonic diode and all optical logic gate application using SSPM method.

1.12 Orientation of Thesis

This thesis contains six chapters, the Chapter 1 contains general review of the past applications and approach of nanotechnology. The Chapter 2 contains literature review of the present research, applications and technological development of pressure sensors incorporating different nanomaterials, it also contains present researches on SSPM study of different nanomaterials. The Chapter 3 contains general introduction to characterization tools and experimental apparatus used in the thesis. The Chapter 4 focuses on the

synthesis, characterization result of Bi_2Se_3 nanoflakes. Also, the study of piezo-resistive response of Bi_2Se_3 nanoflakes coated tissue paper and the fabricated device showed response upon application of different pressure. An e-skin was developed to quantify the spatial distribution of pressure. The Chapter 5 focuses synthesis, characterization result of Bi_2Se_3 nanoflakes and the non-linear optical response of Bi_2Se_3 nanoflakes. The nonlinear refractive index(n_2) and third order non-linear susceptibility (χ^3) was calculated. Chapter 6 concludes the work in this thesis and discusses the future prospects in this area.

1.13 References

1. Gnach, A., et al., *Upconverting nanoparticles: assessing the toxicity*. 2015. **44**(6): p. 1561-1584.
2. Binnig, G., et al., *Surface Studies by Scanning Tunneling Microscopy*. Physical Review Letters, 1982. **49**(1): p. 57-61.
3. Barber, D.J. and I.C.J.A. Freestone, *An investigation of the origin of the colour of the Lycurgus Cup by analytical transmission electron microscopy*. 1990. **32**(1): p. 33-45.
4. Pradell, T., et al., *Metallic and nonmetallic shine in luster: An elastic ion backscattering study*. 2007. **101**(10): p. 103518.
5. Poole Jr, C.P. and F.J. Owens, *Introduction to nanotechnology*. 2003: John Wiley & Sons.
6. Faraday, M.J.P.T.o.t.R.S.o.L., X. *The Bakerian Lecture.—Experimental relations of gold (and other metals) to light*. 1857(147): p. 145-181.
7. Bayda, S., et al., *The History of Nanoscience and Nanotechnology: From Chemical–Physical Applications to Nanomedicine*. 2020. **25**(1): p. 112.
8. Binnig, G., et al., *Tunneling through a controllable vacuum gap*. 1982. **40**(2): p. 178-180.
9. Kroto, H.W., et al., *C60: Buckminsterfullerene*. 1985. **318**(6042): p. 162-163.
10. Iijima, S.J.n., *Helical microtubules of graphitic carbon*. 1991. **354**(6348): p. 56-58.
11. Xu, X., et al., *Electrophoretic analysis and purification of fluorescent single-walled carbon nanotube fragments*. 2004. **126**(40): p. 12736-12737.

Chapter:1 Introduction

12. Kinnear, C., et al., *Form follows function: nanoparticle shape and its implications for nanomedicine*. 2017. **117**(17): p. 11476-11521.
13. Rothmund, P.W.J.N., *Folding DNA to create nanoscale shapes and patterns*. 2006. **440**(7082): p. 297-302.
14. Hussein, A.K.J.R. and S.E. Reviews, *Applications of nanotechnology in renewable energies—A comprehensive overview and understanding*. 2015. **42**: p. 460-476.
15. Wang, Z.L. and W.J.A.C.I.E. Wu, *Nanotechnology-enabled energy harvesting for self-powered micro-/nanosystems*. 2012. **51**(47): p. 11700-11721.
16. He, Y. and Y.J.P.C.C.P. Zhao, *Improved hydrogen storage properties of a V decorated Mg nanoblade array*. 2009. **11**(2): p. 255-258.
17. Cheng, H.-M., Q.-H. Yang, and C.J.C. Liu, *Hydrogen storage in carbon nanotubes*. 2001. **39**(10): p. 1447-1454.
18. Chen, X., et al., *Electrochemical hydrogen storage of carbon nanotubes and carbon nanofibers*. 2004. **29**(7): p. 743-748.
19. Bangham, A.D., M.M. Standish, and J.C.J.J.o.m.b. Watkins, *Diffusion of univalent ions across the lamellae of swollen phospholipids*. 1965. **13**(1): p. 238-IN27.
20. Langer, R. and J.J.N. Folkman, *Polymers for the sustained release of proteins and other macromolecules*. 1976. **263**(5580): p. 797-800.
21. Yatvin, M., et al., *p H-Sensitive Liposomes: Possible Clinical Implications*. 1980. **210**(4475): p. 1253-1255.
22. Weng, Z., et al., *Wafer-Scale Graphene Anodes Replace Indium Tin Oxide in Organic Light-Emitting Diodes*. 2022. **10**(3): p. 2101675.
23. Lee, J.U., P. Gipp, and C.J.A.P.L. Heller, *Carbon nanotube p-n junction diodes*. 2004. **85**(1): p. 145-147.
24. Strukov, D.B., et al., *The missing memristor found*. 2008. **453**(7191): p. 80-83.
25. Parkin, S.S., M. Hayashi, and L.J.S. Thomas, *Magnetic domain-wall racetrack memory*. 2008. **320**(5873): p. 190-194.
26. Yao, J., et al., *Resistive switches and memories from silicon oxide*. 2010. **10**(10): p. 4105-4110.
27. Kumar, D., et al., *Pulsed laser deposition assisted novel synthesis of self-assembled magnetic nanoparticles*. 2004. **35**(2): p. 149-155.
28. Cui, Y., et al., *Nanowire nanosensors for highly sensitive and selective detection of biological and chemical species*. 2001. **293**(5533): p. 1289-1292.
29. Poncharal, P., et al., *Electrostatic deflections and electromechanical resonances of carbon nanotubes*. 1999. **283**(5407): p. 1513-1516.
30. Cleland, A.N. and M.L.J.N. Roukes, *A nanometre-scale mechanical electrometer*. 1998. **392**(6672): p. 160-162.

Chapter:1 Introduction

31. Modi, A., et al., *Miniaturized gas ionization sensors using carbon nanotubes*. 2003. **424**(6945): p. 171-174.
32. Nicewarner-Pena, S.R., et al., *Submicrometer metallic barcodes*. 2001. **294**(5540): p. 137-141.
33. Machado, F.M., et al., *Carbon nanoadsorbents*, in *Carbon nanomaterials as adsorbents for environmental and biological applications*. 2015, Springer. p. 11-32.
34. Kane, C.L. and E.J.J.P.r.l. Mele, *Quantum spin Hall effect in graphene*. 2005. **95**(22): p. 226801.
35. Qi, X.-L. and S.-C.J.a.p.a. Zhang, *The quantum spin Hall effect and topological insulators*. 2010.
36. Bernevig, B.A., T.L. Hughes, and S.-C.J.s. Zhang, *Quantum spin Hall effect and topological phase transition in HgTe quantum wells*. 2006. **314**(5806): p. 1757-1761.
37. Nayak, C., et al., *Non-Abelian anyons and topological quantum computation*. 2008. **80**(3): p. 1083.
38. Moore, J.J.N.P., *The next generation*. 2009. **5**(6): p. 378-380.
39. Linder, J., T. Yokoyama, and A.J.P.r.B. Sudbø, *Anomalous finite size effects on surface states in the topological insulator Bi₂Se₃*. 2009. **80**(20): p. 205401.
40. Zhang, H., et al., *Topological insulators in Bi₂Se₃, Bi₂Te₃ and Sb₂Te₃ with a single Dirac cone on the surface*. 2009. **5**(6): p. 438-442.
41. Zhang, G., et al., *Quintuple-layer epitaxy of thin films of topological insulator Bi₂Se₃*. 2009. **95**(5): p. 053114.
42. Peng, H., et al., *Aharonov–Bohm interference in topological insulator nanoribbons*. 2010. **9**(3): p. 225-229.
43. Zhou, B., et al., *Finite size effects on helical edge states in a quantum spin-Hall system*. 2008. **101**(24): p. 246807.
44. Haldane, F.D.M.J.P.r.l., *Model for a quantum Hall effect without Landau levels: Condensed-matter realization of the "parity anomaly"*. 1988. **61**(18): p. 2015.
45. Volovik, G.E., *Exotic properties of superfluid ³He*. Vol. 1. 1992: World Scientific.
46. Zhang, S.-C. and J.J.S. Hu, *A four-dimensional generalization of the quantum Hall effect*. 2001. **294**(5543): p. 823-828.
47. Ryu, S., et al., *Topological insulators and superconductors: tenfold way and dimensional hierarchy*. 2010. **12**(6): p. 065010.
48. Sinova, J., et al., *Universal intrinsic spin Hall effect*. 2004. **92**(12): p. 126603.
49. Bernevig, B.A. and S.-C.J.P.r.l. Zhang, *Quantum spin Hall effect*. 2006. **96**(10): p. 106802.
50. Hsieh, D., et al., *A topological Dirac insulator in a quantum spin Hall phase*. 2008. **452**(7190): p. 970-974.

Chapter:1 Introduction

51. Torrisi, F. and J.N.J.N.n. Coleman, *Electrifying inks with 2D materials*. 2014. **9**(10): p. 738-739.
52. Liu, L., et al., *Heteroepitaxial growth of two-dimensional hexagonal boron nitride templated by graphene edges*. 2014. **343**(6167): p. 163-167.
53. Frindt, R.J.J.o.A.P., *Single crystals of MoS₂ several molecular layers thick*. 1966. **37**(4): p. 1928-1929.
54. Mak, K.F., et al., *Atomically thin MoS₂: a new direct-gap semiconductor*. 2010. **105**(13): p. 136805.
55. Radisavljevic, B., et al., *Single-layer MoS₂ transistors*. 2011. **6**(3): p. 147-150.
56. Wilson, J.A., F. Di Salvo, and S.J.A.i.P. Mahajan, *Charge-density waves and superlattices in the metallic layered transition metal dichalcogenides*. 1975. **24**(2): p. 117-201.
57. Kappera, R., et al., *Phase-engineered low-resistance contacts for ultrathin MoS₂ transistors*. 2014. **13**(12): p. 1128-1134.
58. Wang, Q.H., et al., *Electronics and optoelectronics of two-dimensional transition metal dichalcogenides*. 2012. **7**(11): p. 699-712.
59. Jariwala, D., et al., *Emerging device applications for semiconducting two-dimensional transition metal dichalcogenides*. 2014. **8**(2): p. 1102-1120.
60. Fiori, G., et al., *Electronics based on two-dimensional materials*. 2014. **9**(10): p. 768-779.
61. Das, B., et al., *Topological insulator Bi₂Se₃/Si-nanowire-based p–n junction diode for high-performance near-infrared photodetector*. 2017. **9**(27): p. 22788-22798.
62. Das, B., et al., *Flexible, transparent resistive switching device based on topological insulator Bi₂Se₃-organic composite*. 2018. **124**(12): p. 124503.
63. Das, B., et al., *rGO-Wrapped flowerlike Bi₂Se₃ nanocomposite: synthesis, experimental and simulation-based investigation on cold cathode applications*. 2016. **6**(31): p. 25900-25912.
64. Razzaque, S., et al., *Selective synthesis of bismuth or bismuth selenide nanosheets from a metal organic precursor: investigation of their catalytic performance for water splitting*. 2021. **60**(3): p. 1449-1461.
65. Viti, L., et al., *Plasma-wave terahertz detection mediated by topological insulators surface states*. 2016. **16**(1): p. 80-87.
66. Liu, S., et al., *Two-dimensional Bi₂Se₃ nanosheet based flexible infrared photodetector with pencil-drawn graphite electrodes on paper*. 2020. **2**(2): p. 906-912.
67. Liu, Z., et al., *Transcatheter self-powered ultrasensitive endocardial pressure sensor*. 2019. **29**(3): p. 1807560.

Chapter:1 Introduction

68. Yang, J.C., et al., *Electronic skin: recent progress and future prospects for skin-attachable devices for health monitoring, robotics, and prosthetics*. 2019. **31**(48): p. 1904765.
69. Chang, J.S., et al., *A circuits and systems perspective of organic/printed electronics: review, challenges, and contemporary and emerging design approaches*. 2017. **7**(1): p. 7-26.
70. Kang, S., et al., *Highly sensitive pressure sensor based on bioinspired porous structure for real-time tactile sensing*. 2016. **2**(12): p. 1600356.
71. Puers, R.J.S. and A.A. Physical, *Capacitive sensors: when and how to use them*. 1993. **37**: p. 93-105.
72. Dobrzynska, J.A., M.A.J.S. Gijs, and A.A. Physical, *Flexible polyimide-based force sensor*. 2012. **173**(1): p. 127-135.
73. Mannsfeld, S.C., et al., *Highly sensitive flexible pressure sensors with microstructured rubber dielectric layers*. 2010. **9**(10): p. 859-864.
74. Ruth, S.R.A., et al., *Rational design of capacitive pressure sensors based on pyramidal microstructures for specialized monitoring of biosignals*. 2020. **30**(29): p. 1903100.
75. Peng, P., R. Rajamani, and A.G.J.J.o.m.s. Erdman, *Flexible tactile sensor for tissue elasticity measurements*. 2009. **18**(6): p. 1226-1233.
76. Zhuo, B., et al., *High sensitivity flexible capacitive pressure sensor using polydimethylsiloxane elastomer dielectric layer micro-structured by 3-D printed mold*. 2017. **5**(3): p. 219-223.
77. Xu, F., et al., *Recent developments for flexible pressure sensors: A review*. 2018. **9**(11): p. 580.
78. Kim, K.-H., et al., *Wearable resistive pressure sensor based on highly flexible carbon composite conductors with irregular surface morphology*. 2017. **9**(20): p. 17499-17507.
79. Zhu, B., et al., *Microstructured graphene arrays for highly sensitive flexible tactile sensors*. 2014. **10**(18): p. 3625-3631.
80. Wang, X., et al., *Silk-molded flexible, ultrasensitive, and highly stable electronic skin for monitoring human physiological signals*. 2014. **26**(9): p. 1336-1342.
81. Persano, L., et al., *High performance piezoelectric devices based on aligned arrays of nanofibers of poly (vinylidene fluoride-co-trifluoroethylene)*. 2013. **4**(1): p. 1-10.
82. Akiyama, M., et al., *Flexible piezoelectric pressure sensors using oriented aluminum nitride thin films prepared on polyethylene terephthalate films*. 2006. **100**(11): p. 114318.
83. Das, P.S., et al., *A laser ablated graphene-based flexible self-powered pressure sensor for human gestures and finger pulse monitoring*. 2019. **12**(8): p. 1789-1795.

Chapter:1 Introduction

84. Boyd, R.W., *Nonlinear optics*. 2020: Academic press.
85. Wu, R., et al., *Purely coherent nonlinear optical response in solution dispersions of graphene sheets*. 2011. **11**(12): p. 5159-5164.
86. Kalimuddin, S., et al., *Nonlinear coherent light-matter interaction in 2D MoSe₂ nanoflakes for all-optical switching and logic applications*. 2022.
87. Wang, Q., et al., *Broadband nonlinear optical response in Bi₂Se₃-Bi₂Te₃ heterostructure and its application in all-optical switching*. 2019. **9**(2): p. 025022.
88. Shan, Y., et al., *A promising nonlinear optical material and its applications for all-optical switching and information converters based on the spatial self-phase modulation (SSPM) effect of TaSe₂ nanosheets*. 2019. **7**(13): p. 3811-3816.
89. Wang, G., et al., *Tunable effective nonlinear refractive index of graphene dispersions during the distortion of spatial self-phase modulation*. 2014. **104**(14): p. 141909.
90. Wang, J., et al., *Broadband nonlinear optical response of graphene dispersions*. 2009. **21**(23): p. 2430-2435.
91. Teng, C., et al., *Flexible, thermally conductive layered composite films from massively exfoliated boron nitride nanosheets*. 2019. **124**: p. 105498.
92. Wang, G., et al., *Tunable nonlinear refractive index of two-dimensional MoS₂, WS₂, and MoSe₂ nanosheet dispersions*. 2015. **3**(2): p. A51-A55.

Chapter 2

Literature Review

2.1 Literature of past Work: Pressure Sensor Device

In recent years flexible electronics have drawn attention to various applications like healthcare monitoring, human machine interaction.[1, 2]. Traditional silicon based MOSFET pressure sensor lacks the flexibility. To make a such flexible pressure sensor two type of element is necessary, one the conducting medium and the other is substrate. The chosen substrate is highly desired to be porous, so that it can absorb the conducting material. In the recent literature different material and substrate is discussed. To date different kind of material have been used such as carbon nanotube[3], graphene[4],Au nanowire[5], Ag nanowire[6]. Also, different kind of substrates have been used like PDMS, tissue, sponge etc. In those above-mentioned substrates tissue paper holds interesting properties as it is more porous and it can absorb much more material. Hence during application input signal, it can show wide range of sensitivity as well different output range. Paper is the one of the most important invention of the human society, it is light-weight, cheap, disposable, environment-friendly. Paper has become an integral part of daily human life. It is also available in different composition, texture. Recently paper based devices has been of great interest due to their application as a pressure sensor[7],gas sensor [8], energy storage device [9], diode[10] and transistor[11]. This is due to the huge advantage of using flexible devices for healthcare monitoring and this is growing field as this devices can be used to measure biological activities like respiration, heart pulses, body movement. This online monitoring of the devices can be essential as they don't interrupt any in-vitro biological processes of the body, this devices can be easily patched on to the body part of a human being. Devices can be used to record many biological data which can in turn can be used for detection of many diseases like asthma, cancer, diabetes and so forth. Apart

from these this devices can be used to measure external pressure and biological signals without any interruption of any biological processes happening inside the body. In order to fabricate high performance pressure sensor, various materials has been used such as carbon nanotube incorporated with polymer substrate[12], graphene nanosheets[13], graphite particle and metal nanostructures [5, 7], carbon black[1] etc. the sensing mechanism of the paper based pressure sensors are quite simple, it depends upon the change in electrical transport due to the change in contact area of the sensor material upon application of pressure. The main contributing factor of the paper-based sensor is the porosity of the material which can be greatly influence the performance of the device. Till now researches have used different kind of papers such as whatman paper, tissue paper, photocopy paper etc. The porosity of the paper or the porous structure of the paper is significantly important as it decides the amount of material to be soaked. Also, another way of adding layered paper into the substrate is to add more paper layer into the device. An ideal pressure sensor should possess high sensitivity, long durability and good repeatability[14].

Over last few years pressure sensors working on different principles have been employed like piezocapacitive[14], piezoelectric[15], triboelectric[16] etc. and piezoresistive principle[12, 14, 17]. Among the above operating principles the devices working in piezoresistive principle principles yields high sensitivity, repeatability, reproducibility and low power consumption in the low pressure range[18]. Most of the research done in this field is confined to 2D TMDC material, metallic materials etc. liquid exfoliation of 2D TMDC is material is easy and very cost-effective procedure and controlled nature of the above said experiment is very research interesting. Ying Lu et al.[19] reported graphene incorporated silk which showed great responsivity, this silk was available in the market.

They have also made different layered devices to report best efficiency device. Other groups have reported different ways of fabricating graphene for pressure sensor devices, Fu et al. devised a way to incorporate graphene using CVD method, they reported a strain sensor using the device[20]. The previously mentioned device was made using PDMS substrate. However, this method requires high temperature which in turn makes it difficult for device fabrication, also the process of removing substrate and encapsulating the graphene in the porous material is also quite difficult. Tian and et. al produced an alternative way of producing graphene using laser-scribe method on foam like substrate[21].

In 2017 Tao et al. produced a rGO based pressure sensor capable of producing excellent sensitivity in the range 0-20 kPa, when used as a wearable device[14]. They also mentioned the need of highly sensitive flexible pressure sensor for IOT applications related to healthcare monitoring. In the above-mentioned literature, authors fabricated a device which shows great promise by of showing reading at 20 kPa with a reported sensitivity of 17.2 kPa^{-1} . Also, the device is greatly stable. It can be used as a wearable device, can monitor human responses like respiration, wrist-pulse detection, movement detection, voice recognition etc. The sensor is easy to fabricate can be produced in wide scale manner with a very low cost. Authors devised a fabrication technique where the tissue papers were cut into squares and placed in culture dish. Then the tissues were soaked with GO solution of 2 mg/ml concentration using drop cast method. After this drop casting method, the culture dish was put into the oven for 5 h at 250 degree Celsius. After that, the GO is turned into rGO, and this rGO-soaked tissue papers were stacked onto each other. They have reported eight or five layer of stacked tissue paper to form sensor device. Then the top and bottom

layer of the device is connected to Cu foil using Ag paste. And at the end the pressure sensor is encapsulated with polyimide tape. As it is seen the fabrication process of the graphene-based sensor is very easy and the fabricated device shows good repeatability. The one-layer device sensor shows best response in the region of 2-20 kPa and the reported sensitivity is 0.1 kPa^{-1} . The eight-layer device shows response in the range of 0-2 kPa^{-1} and reports a sensitivity of 17.2 kPa^{-1} . The five-layer device shows a great response between 0-20 kPa and reports a sensitivity of 16.2 kPa^{-1} . And they have also reported that pressure sensors made from tissue papers are more stable and shows better sensitivity than the devices made from filter paper or Whatman paper. The authors also found that different no. of stacked tissue papers can impact the sensitivity of the device. The air gap between the device is reported to be important factor in deciding the reported sensitivity of the device.

Hong Bin Yao et al. produced highly sensitive graphene made of polyurethane sponge based on microstructure design[22]. Authors have three-dimensional network of sponge and these network is conductive and these fibers are easily bendable, elastic and perfectly elastic. They have also done finite element method analysis to analyses how microstructure topology effects variation rate of the contacts among the network. They have also found that variation in microstructure due application of pressure can cause contact area to increase. To construct large area conductive fiber network, on a polyurethane sponge. Graphene is one atom thick two-dimensional layer of sp^2 bonded carbon, this has shown to produce great electronic and mechanical property. This Go-nanosheets were then dip-coated on PU sponge. At last, they attached electrode with sponge on both side, they also recorded the resistance with the varying pressure. They have found that fractured

microstructure rGO-PU enhances the two order in magnitude in the region 0-2 kPa and one order in the region 2-10 kPa compared to original rGO-PU. They have also indicated that fractured microstructure in the sponge can greatly enhance the sensitivity. It showed greater sensitivity of 0.26 kPa^{-1} in the region 0-3 kPa and showed less sensitivity of 0.03 kPa^{-1} in the region of 3-10 kPa^{-1} . They have also demonstrated a pulse detection system made up of PDMS belt which can record wrist pulses during normal condition and heavy exercising condition. They have also demonstrated a potential application of electronic skin which can be used to detect pressure on any surface area, they made this using pixel arrays which can detect spatial distribution of the pressure applied.

In 2019 Zhiyaan Han et al.[1] fabricated a flexible pressure sensor made up of airlaid paper and Carbon-Black. This process of making the pressure sensor is extremely cheap and simple. The sensing material of the pressure sensor is based on the low-cost carbon black material and it is fabricated via drop casting the CB solution on to the air laid paper. Through stacking multiple CB-soaked airlaid paper onto each other they were able to make a pressure sensor capable of demonstrating a frequency of 51.23 kPa^{-1} and an ultra-low detection limit of 1 Pa. Also, the sensor shows good repeatability, ultra-fast response time. Also, the authors were able to detect weak airflow, wrist pulse detection, wrist bending etc. In addition, they also demonstrated electronic skin application using array of pressure sensor put together. They have also varied the no. of layers encased in the pressure sensor, it was found that for low pressure range the four-layer device showed sensitivity of 51.23 kPa^{-1} , three-layer device showed a sensitivity of 9.15 kPa^{-1} and the two-layer device showed a sensitivity of 7.12 kPa^{-1} . But the three-layer pressure sensor showed much more flexibility, good repeatability and sensitivity over wide range of pressure. In addition of

the subtle pressure this device can detect wide range of pressure applied to the device. the authors also reported different kind of application such as angle measurement from wrist bending, breathing detection etc. This fabricated device has shown response time of less than 200 ms and a high durability of 3000 cycles. A small amount of Ag paste was used to increase conductivity and improve signal collection strength.

In 2014 Shu Gong fabricated a pressure sensor made up of ultrathin gold nanowires[5]. This fabrication method is cheap, cost effective, this pressure sensor is made up by sandwiching the Au nanowire impregnated tissue papers between two PDMS films. Also, the entire fabrication process is scalable and can be used for large scale production and patterning is possible for large scale application. Authors demonstrated that the device can be operated as low voltage of 1.5 V with power consumption of less than 30 μ W and are able to detect pressure as low as 13 Pa with fast response time. Also, it has shown high sensitivity of 1.14 kPa⁻¹ in the pressure range of 0-5 kPa and high stability of 50,000 loading and unloading cycle. To assess the device strain gauge, factor the authors formulated experiments, to see if the device works as a strain gauge sensor. The authors also showed high durability by exposing the pressure sensor under a pressure of 2.5 kPa at 2 Hz.

In 2018 Hae Jin Kim et al. constructed a highly stretchable and sensitive semiconductor for pressure sensing application[6]. They constructed 3X3 array is constructed for encapsulating functional systems, two layers of PDMS (layer 1 and 2) AGNW/PDMS conductor(layer1) and P3HT-NF/PDMS (layer 2) are stacked together. For the flexibility they have employed rubbery semiconductor P3HT nanofibrils and the π - π stacking is exploited. It is mixed with PDMS to yield the stretchability. This fabricated pressure sensor showed reversible sensing capability, high gauge factor (32), high linearity($R^2 > .996$), and

low hysteresis (12%) responses up to mechanical strain 100%. A strain sensor can be employed on gloves making the product smart which can be employed for smart applications. To illustrate the application of such sensor, the sensors are applied onto the gloves so that different hand gestures can be recognized.

In 2020 Pratik M Pataniya et al. reported pressure sensor based on 2D-WSe₂ nanosheets[23]. In this paper authors have varied the type of paper upon which the WSe₂ nanosheets were suspended those are Whatman filter paper and tissue paper. Tissue paper showed greater porosity and hence better material absorption leading to higher sensitivity. The authors have synthesized the WSe₂ nanosheets using solvothermal synthesis and size-controlled exfoliation of the nanosheets makes it possible drop cast the material into the tissue. Using SEM, they have determined that the hole size in the tissue paper is larger than the observed in Whatman paper. The proper coating on tissue paper yields better results than the Whatman paper. The resistance measured on the tissue paper is found to be 81 ohm compared to the what man paper 75 ohm. The pressure sensor was able to show broad range of pressure range 1-100 kPa with exceptionally high sensitivity of 29.4 kPa⁻¹, current responsivity of 70 ms and response time of 100 ms. This pressure sensor was even able to detect small pressure change of 1.4 Pa generated by water drop. The pressure sensor was able to detect pressure generated due to the tapping of the finger onto the device.

In 2017 Ying Liu et al. produced a flexible pressure sensor-based graphene-silk network structure[19]. The production of this kind of structure is easy to prepare, low cost it is based of silk substrate which can be thermally reduced to get good performance. As the substrate body is silk which can produce 3D ordered multi-layer structure for material absorption. The reported sensitivity value is 0.4 kPa⁻¹ and the measurement range can be as high as

140 kPa. This sensor is shown to detect bodily signals. The sensitivity value with 3 layers was 0.082 kPa^{-1} . And the sensitivity value with layers 5,7 and 9 were 0.12 kPa^{-1} , 0.29 kPa^{-1} and 0.4 kPa^{-1} respectively. The device sensitivity value increased with the number of layers. When the no. of layers changed from 3 layers to 9 layers the change in resistance was significant 145 kOhm to 1.16 kOhm. When the pressure was applied to the device, part of the gap was closed which resulted in decrease in resistance. In addition, as the pressure increased the contact points also increased leading to decrease in resistance in the upper and lower electrode.

In 2020 Pratik M Pataniya et al. produced a pressure sensor based on MoSe_2 nanosheets coated on cellulose paper[24]. This fabricated sensor shows ability to sense different deformities such as pressing, twisting and trivial vibrations such as pulses etc. The present sensor exhibits large pressure sensitivity of 18.42 kPa^{-1} in the pressure range 0.001-0.05 kPa, 7.28 kPa^{-1} in the pressure range 1-35 kPa and 2.63 kPa^{-1} in the pressure range 40-100kPa. The pressure sensor is also capable of detecting vibrations of machines including cellular phones, compressor etc. The sensor shows excellent repeatability and environmental stability. The bulk MoSe_2 crystal was exfoliated using sonication procedure and was synthesized using direct vapor transport growth. The rise time and the decay time was recorded to be about 110 ms and 60 ms. The pressure sensor also showed that for smaller pressure the ranging from 0.001-0.5 kPa, the sensitivity was approximately about 18.42 kPa^{-1} . The reported device showed response even after 6 months.

In 2019 Seunghwan Kim et al. produced a CNT coated elastomer for healthcare devices or human interface monitoring[25]. The authors have integrated CNT into the elastomer for

making highly sensitive 3D network, with greater porosity. The elastomer with greater porosity is taken into consideration because it showed greater sensitivity. The authors reported a sensitivity of $0.001\text{--}0.002\text{ kPa}^{-1}$ and a wide pressure range of 10 Pa to 1.2 MPa with linearity of 0.096. The fabricated pressure sensor showed excellent stability upon bending type deformation. The authors also have integrated the device with flexible piano for entertainment purposes.

In 2014 Chwee Lin Choong et al. fabricated a highly sensitive pressure sensor capable of operating under low pressure region[25]. They have micropatterned the PDMS substrate, this causes the sensor to have high sensitivity. They have demonstrated micro-pyramid array with spring like compressible platform that are deposited to form a base for capacitive electrode. This micropatterned structure is then coated with PEDOT: PSS/PUD composite for a semiconducting layer, which generate electron upon the application of pressure. This microstructure was essential to yield such properties. Using SEM analysis authors have found that each dome size is of approximately of $8\text{ }\mu\text{m} \times 8\text{ }\mu\text{m}$ in dimension. The sensor showed a sensitivity of 4.88 kPa^{-1} over a wide range of pressure from 0.37 to 0.59 kPa. They also stated that the resistive mode of sensitivity is 9 times more than the capacitive counterpart (0.55 kPa^{-1}). Also, the sensor showed low hysteresis from the multiple cycle of loading and unloading. The sensor shows increased sensitivity with elongation about 10.3 kPa^{-1} when stretched by 40%. The sensor operating voltage of 0.2 V is sufficiently low to allow the powering of self-power device, green hybrid device to be possible.

In 2019 Dekui Song et al. produced a hollow structured MXene-PDMS nanocomposite as a flexible, wearable, bendable pressure sensor[26]. Authors synthesized it using nickel foam as the three-dimension substrate into which the MXene nanosheets are dip coated,

followed by adding PDMS substrate and etching of nickel foam. The fabricated device shows wide range of angle detection using 0-180 degree and shows excellent long-term stability. This device showed repeatability even after 1000 cycles. It was able to detect signals in the incremental amount of angle bending of 0-15-30-150 degree. And a stable durability in the angle bending of 30 degree and can endure a frequency range from 0.05 to 2 Hz as a bendable piezoresistive pressure sensor. The sensor shows very low detection limit for pressure sensor. Slipping of MXene sheets from each other is the operating reason for which the device was able to detect small vibrations and human movement. They have also made a MPC sensor made of 4X4 array for electronic skin application.

In 2016 Yuanqing Li et al. fabricated a device which is capable of working as a strain sensor[27]. This sensor is made from tissue paper and the above-mentioned sensor is easy to produce and cheap in cost. The sensor is made from carbon paper and PDMS elastomer. This carbon paper is prepared from high temperature pyrolysis process. This strain sensor is highly sensitive with gauge factor of 25.3, about 10 times higher than conventional mechanical strain gauge. The authors also performed cyclic strain test on the device. It showed fast response and steady response in the frequency range .01-10 Hz the authors have also demonstrated potential healthcare application of the device. breath monitoring, robot controlling etc. was performed.

In 2019 Lei Gao et al. [7]fabricated a low-cost pressure sensor based on Ag-NW coated sensing material, a nanocellulose as a bottom substrate for printing electrode and another NCP as a top layer to encapsulate the whole system. The sensor showed a sensitivity of 1.5 kPa^{-1} in the range of 0.03-30.32 kPa and it retained its characteristics under bending states also. Furthermore, the sensor was used to detect signals like arterial pulse and

pronunciation from throat. The authors have also tested for potential electronic skin application. Due to the use of low-cost materials like NCP, Ag-NW the application of such brings down the cost of the device hence nominal cost production.

Oliveria et al. developed a Ag-Nw based pressure sensor for bio-medical application[28]. The flexible pressure sensor was fabricated using silver nanowire deposited on in PDMS substrate in a sandwich like structure. Then they attached the sensor to a ring-shaped connecting module and then to a pacifier. Authors reported a sensitivity of 0.06 kPa^{-1} in pressure range 0-4 kPa and 0.63 kPa^{-1} in the region 4-7 kPa. The sensor showed rise time of 0.184 s and fall time of 0.184 s while loading and de-loading condition under 6 kPa pressure. The sensor showed electro-mechanical stability and high sensitivity. The application involved monitoring of primitive reflexes of infants during the early development period and evaluate early sucking power. The non-invasive, low cost and light weight pressure sensor application is very interesting.

In 2019 Hakyung Jeong et al. fabricated a pressure sensor using PDMS substrate and Ag-nanowires[29]. During the fabrication process Ag electrode was fabricated on the bottom of the PDMS layer by doctor blading method, and Ag-NW was embedded in the top of the PDMS layer, so that natural airgap can be produced between the Nanowires. Thus, the formed air-gap was controlled by the number of Ag-NW layers and played an important role in decreasing the current while decreasing the current in absence of any pressure. A sensitivity of 16.1 kPa^{-1} was reported by optimizing the air-gap thickness and the Ag-NW sensing area. The stability of the pressure sensor was confirmed by durability, repeatability, bending and hysteresis test. This device showed a great opportunity for measuring various type of forces and displacement in wearable devices.

In 2022 Guodong Wang et al. fabricated a pressure sensor based on piezo-resistive composite layer[30]. They have used SAP⁺ polymer on PDMS substrate, here SAP⁺ is used a conductive filler for this pressure sensor. This elastic polymer is used to replace the common rigid substances (CNT, Graphene, CNW etc.). Using this polymer substance, the authors were able to reduce the Young's modulus of the pressure sensor. The sensor showed high sensitivity of 0.062 kPa⁻¹, a fast response time (0.136 s) and excellent cyclic loading and de-loading cycles of >500 cycles.

In 2019 Li et al. fabricated an ultrasensitive, flexible and low cost piezo-resistive pressure sensor for tactile pressure sensing[31]. The authors have reported a facile sacrificial casting method to synthesize nanoporous carbon-nanotube and polymer nanocomposite for conductive filler in the pressure sensor. The authors reported that their solution overcame the limitation of solution-based drop-casting method for impregnating the nanoscale porous surface with nanoscale conductive material. The fabricated pressure sensor showed a strain gauge factor of 300 which approximately 50 times CNT based pressure sensor and 10 times higher any graphene based piezo-resistive sensor. The authors demonstrated that the sensor is capable of sensing subtle pressure in the region of 1 Pa- 1 kPa and gentle pressure of 1 kPa-25 kPa. They have chosen NPC as the microstructure of the device and they have controlled the weight ratio of the ZnO nanoparticles to enhance the porosity of the structure, it was reported that with highly porous device showed greater sensitivity.

2.2 Literature of past Work: SSPM

Non-linear optics is a study of high intensity light in a non-linear medium, and the polarization density is not linearly dependent on the electric field. The inception of the field occurred when Mainman developed first laser in 1960s[32]. In time many non-linear effect

was discovered like SHG, stimulated Raman scattering, optical phase conjugation, optical bi-stability, Saturable absorption, optical Kerr effect. Photonic application has various similarity to electronic application, also added many advantages. Non-linear effects are employed in many applications such as biological image processing[33], ultrafast laser spectroscopy[34], optoelectronic applications [35] and all optical devices[36] like diode, logic gate applications. Third order non-linear susceptibility of the material is an important parameter of the material that contribute towards non-linear property. In general, the methods for measurement of the parameter non-linear susceptibility are four-wave mixing, Z-scan etc. SSPM (Spatial Self-Phase Modulation technique) has some advantage over above mentioned procedure. SSPM is a short method comprising of short measurement period.

SSPM is an all-light modulation technique occurring due to the Kerr nonlinearity of the material.

In 1967, Callen et al. first investigated such non-linear optical property of material[37]. They have experimented on a medium through which a beam of light passes through, and decreases the linear refractive index with the increasing temperature. And the medium acts as negative lens.

In 1978 Stolen et al. employed SSPM technique to find optical response of single-mode fiber[38]. The experiment provided an independent measurement of non-linear coefficient, the self-focusing coefficient. The results also pointed on some basic information of mode-locked laser pulses.

SSPM causes significant spread in the spectrum and achieve precise modulation of the phase. In 1981 Durbin et al. experimented with SSPM technique in liquid crystal and constructed the numerical theory necessary for SSPM technique. With the experiment authors discovered formation of multiple diffraction rings as cw laser beam passes through a homeotropic nematic film. This causes due to SSPM technique resulted due to the laser-induced Freedericksz transition. In the next 30 years the SSPM technique has been mainly concentrated to optical fiber. The research progress has been developing slowly, with the discovery of graphene the SSPM technique and its application progressed rapidly. Graphene is a 2D material that shows strong light-matter interaction, providing strong observation for SSPM technique. The electronic structures of 2D materials make it possible for all kind of Optical applications such as optical diode, optical modulator etc. All optical modulation technology and device technology is going to be very important future application of optoelectronic applications. In dual beam SSPM named as Spatial Cross phase modulation the phase of the incident light is not only modulated by the intensity of its own, also by the pump light intensity.

In 2017 Lu et al. experimented with cross-phase modulation technique with few layers of bismuthene with rhombohedral A7 structure. They found SXPM pattern with 532 nm laser with intensity (I) 5.48 W/cm^2 . SXPM is a modulation technique which can be applied to realize different optical devices. 2D materials shows completely different properties in contrast to bulk material due the quantum confinement effect. For example, graphene has ultra-high carrier mobility, thermal conductivity and high optical absorption[39].

Despite significant research performed on SSPM, there still exists controversy surrounding the true origin of SSPM technique. Two main formation mechanism was proposed one is pure electronic coherence[40] and the other is thermally induced non-linearity[41].

Fundamentals of SSPM

In the field of non-linear optics, the optical response of a material to an applied light can be expressed by the expression,

$$\tilde{P}(t) = \epsilon_0 [\chi^{(1)} \tilde{E}(t) + \chi^{(2)} \tilde{E}^2(t) + \chi^{(3)} \tilde{E}^3(t) + \dots] \dots\dots\dots(2.1)$$

Where, $\chi^{(1)}$ is the linear susceptibility and $\chi^{(2)}$ and $\chi^{(3)}$ are second order and third order non-linear susceptibility. The term $\chi^{(1)} \tilde{E}(t)$ refers to as conventional linear optical effect, the second term $\chi^{(2)} \tilde{E}^2(t)$ refers to as second order non-linear optical effect and the term $\chi^{(3)} \tilde{E}^3(t)$ refers to as third order non-linear effect. This last term contributes towards third harmonic generation.

The optical Kerr effect refers to the phenomenon caused by birefringent of light caused by the electric field of the light acting on the medium. And the change in the refractive index is proportional to the square of the intensity applied. Assuming the medium is isotropic,

The total non-linear refractive index n of the material is expressed as,

$$n = \sqrt{\chi^{(1)} + \frac{3}{4} \chi^{(3)} \tilde{E}^2(t)} = n_0 + \Delta n \dots\dots\dots(2.2)$$

Chapter: 2

Where n_0 is linear refractive index of the material, and Δn is the change in the refractive index. When the laser light passes through the material, according to the optical Kerr effect the refractive index is referred to as,

$$n = n_0 + n_2 I \dots \dots (2.3)$$

here n_2 is the non-linear refractive index and I is the intensity of the light. Further a change in the refractive index of the medium will cause the phase change of the light. In general gaussian beam is used to excite the medium with length L along the z axis, and its electric field distribution can be,

$$E(r, z) = E(0, z) \frac{\omega_0}{\omega(z)} \exp\left(-\frac{r^2}{\omega(z)^2}\right) \times \exp\left(-i\left[kz - \arctan\frac{z}{z_0} \frac{kr^2 n_0}{2R(z)}\right]\right) \dots \dots (2.4)$$

Where λ is the wavelength of the laser incident, $k = 2\pi/\lambda$ is the wave vector, z_0 is the Rayleigh length that propagates like a plane wave. $R(z)$ is the radius curvature of the wave front.

$$R(z) = z[1 + (z_0/z)^2] \text{ and}$$

$$\omega(z) = \omega_0 \sqrt{1 + \left(\frac{z}{z_0}\right)^2} \text{ is the beam radius at } z.$$

when layered materials is at its thinnest limit, it shows interesting properties which is completely different in comparison to the bulk material. Generally, 2D material refers to a crystalline material, where electrons can move in the nanometer scale although this dimension acts as confined dimension. Topological insulator is a new state of matter which is included in the 2D material. Surface of the material is metallic and bulk of the material is insulating. Compared to graphene, TI has some special optoelectronic properties due to

the combined effect of spin-orbit interaction and the surface state is protected by time-reversal symmetry.

Synthesis and the characterization of the 2D material is a large premise. The synthesis can be done using top-down approach and bottom-up approach. Bottom up refers to synthesis of the material through a chemical reaction method.

Because of the strong non-linear Kerr-effect a phase shift is introduced. The phase has a nonlinear modulating behavior to the transverse intensity profile of the incident gaussian laser beam. A phase shift is introduced which is expressed as,

$$\Delta\psi(r) = \frac{2\pi n_0}{\lambda} \int_0^{L_{eff}} n_2 I(r,z) dz \dots\dots\dots(2.5)$$

I is the light intensity, $\Delta\psi$ is the phase shift of the laser beam, r is the radial coordinate, λ is the wavelength, L is the total effective propagation length through the sample containing cuvette, I(r,z) is the intensity of the distribution. N is the total no rings formed. The ‘self’ phase shift ($\Delta\psi$) that gets modulated due to the nonlinear Kerr Effect is result of the change in optical refractive index, n as function of intensity of the coherent Gaussian laser beam. Therefore, the propagating light creates diffraction pattern of bright and dark rings

And the equation corresponding to the bright and dark rings is,

$$\Delta\psi(r_1) - \Delta\psi(r_2) = 2M\pi \dots\dots\dots(2.6)$$

Here M is the integer and it is even or odd corresponding to the bright or dark ring. Here L_{eff} can be calculated using the equation below,

$$L_{eff} = \int_{L_1}^{L_2} \left(1 + \frac{Z^2}{Z_0^2}\right)^{-1} dZ = Z_0 \tan^{-1} \left[\frac{Z}{Z_0} \right]_{L_1}^{L_2} ; Z_0 = \frac{\pi\omega_0^2}{\lambda} \dots\dots\dots(2.7)$$

In 2011 Wu et al. first demonstrated SSPM technique in 2D graphene sheet. They also developed an efficient chemical exfoliation method for high quality graphene sheets that functionalized by alkylamine. They were able to investigate purely coherent nonlinear optical response of the sheets using near infrared, visible and ultra-violet light. They also experimented with ultra-fast laser beams. They observed SSPM in the dispersed solution. Through the experiment they concluded that this coherent light scattering is due to the effect of third order non-linear susceptibility. This third-order non-linear susceptibility occurs due to the large-scale cone-shaped energy band structure of the graphene. By taking 3mm cuvette and linear refractive index of 1.47 they calculated the non-linear refractive index to be $2.5 \times 10^{-9} \text{ m}^2/\text{W}$. And for unfocused beam being $3 \times 10^{-9} \text{ m}^2/\text{W}$. They have also found the effective no. of layers contributing towards SSPM to be of magnitude 100.

In 2014 Karimzadeh et al. formulated to the conclusion that non-asymmetrical thermal convection is the cause of SSPM ring deformation[42]. In this experiment they have observed that the deformation of the upper half of the ring pattern is due to change in refractive index of the upper half compared to the lower half. This heating is due to the absorption of power from the laser. To find this non-linearity they have solved the heat transfer equation including convection and conduction effect in the medium. The temporal dynamics and structural characteristics of the ring pattern is studied theoretically on the basis of Fresnel-Kirchoff diffraction integral.

In 2014 Ghaozhong Wang et al. proposed a non-linear tunable method based on this collapse effect in SSPM[43]. They observed the SSPM pattern made by passing He-Ne laser beam passing through liquid phase graphene dispersed solution. The diffraction pattern was found to be rapidly distorted due to the horizontal passing of the beam in the

solution. They also calculated the relative change in non-linear refractive index determined by the distortion angle to the half cone angle. The effective non-linear refractive index can be changed by the tuning the laser intensity and the temperature of the dispersion solution.

As early as 2011 Zhao's research team formulated the physical phenomenon behind the SSPM which is caused by the non-local coherence, as the SSPM effect in the graphene was discovered. They further stated the wind chime model to further discuss the underlying phenomenon of ring formation.

In 2019 Youxian Shan et al. experimented with Bismuth Sulfide(Bi_2S_3) which is a binary chalcogenide compound that has interesting optoelectronic properties[44]. In this work they showed strong optical non-linearity using SSPM technique. They also formulated all optical devices e.g., photonic diode and logic gates using this method. They made all optical diode using Bi_2S_3 nanosheet and SnS_2 compound. In this work they have found that the refractive index to be

$n_2=3.34 \times 10^{-5} \text{ cm}^2 \text{ W}^{-1}$ with $\lambda=457 \text{ nm}$ $n_2=1.26 \times 10^{-6} \text{ cm}^2 \text{ W}^{-1}$ with $\lambda=532 \text{ nm}$
and $n_2=1.62 \times 10^{-7} \text{ cm}^2 \text{ W}^{-1}$ with $\lambda=671 \text{ nm}$.

In 2018 Yue Jia et al. experimented with two-dimensional transition metal di-chalcogenide, tungsten diselenide due to its gapped electronic structure, high carrier mobility[45]. There have been few studies correlating between electronic structure and optical properties of material. They calculated non-linear refractive index with laser light of three different wavelength 457 nm, 532 nm and 671 nm lasers. For $\lambda=671\text{nm}$ they have found n_2 to be $8.66 \times 10^{-6} \text{ cm}^2 \text{ W}^{-1}$, for 457 nm laser they have found n_2 to be $6.402 \times 10^{-6} \text{ cm}^2 \text{ W}^{-1}$ and $\chi^{(3)}_{\text{total}}$

to be 2.986×10^{-6} . And for 532 nm laser they have found n_2 to be $2.94 \times 10^{-6} \text{ cm}^2 \text{W}^{-1}$ and $\chi^{(3)}_{\text{total}}$ to be 1.371×10^{-6} .

In 2019 Jie Li et al. have experimented with new kind of MXene and have found their non-linear optical properties[46]. Authors were able to synthesize high quality MXene with $\text{Ti}_3\text{C}_2\text{T}_x$ with HF etching method. This material has ultrafast carrier characteristics with an intra-band recovery time of ~ 0.2 ps. This large optical non-linearity makes the MXene ideal candidate for optoelectronic devices. Authors were able to observe SSPM effect in this material min visible to near-infrared spectrum(400-1064nm), this highlights nonlinear broadband characteristics of the material. By studying the ultra-fast response of with an excitation from ultrafast-pulsed lasers authors were able to calculate the third order non-linear susceptibility of the MXene $\text{Ti}_3\text{C}_2\text{T}_x$. their work confirmed that the Mxene is an ideal candidate for non-linear ultra-fast optoelectronic devices. They have found the $\chi^{(3)}_{\text{total}}$ to be 10^{-15} esu at 800 nm and 10^{-7} esu at 1064 nm.

In 2017 Lili Miao et al. experimented with SSPM technique on black-phosphorus solution[47]. From the experimental result they have concluded that the concentration dependent coherent light diffraction is due to the ultra-fast nonlinear third order susceptibility. They have found the $\chi^{(3)}_{\text{total}}$ to be $10^{-19} \text{ m}^2/\text{V}^2$ by analyzing the experimental result. From the experiment they have obtained the fast relaxation time to be 0.13 ps during dynamic relaxation process. They have also implied that novel application in device regime exploiting this kind of non-linear behavior.

In 2016 Xiaohong Li et al. experimented with enhanced no-linear optical response of MoS_2 and $\text{MoS}_2\text{-TiO}_2$ dispersion and thin film[48]. They have calculated the non-linear

refractive index of MoS₂ to be $3.17 \times 10^{-9} \text{ cm}^2/\text{W}$ and the MoS₂ and TiO₂ to be $2.66 \times 10^{-5} \text{ cm}^2/\text{W}$. They have also found that for spin-coated thin film the reorientation cannot happen. Without non-local electron coherence, the nonlinear refractive index is determined by other factors such as band-changing. For this they experimented with Z scan technique to calculate the non-linear refractive index of the thin films. Thus, doing this they have found both positive and negative refractive index of the MoS₂ thin film. They denoted that the positive value has originated from higher percentage of few-layers of MoS₂ nanosheets. From the experiment they have concluded that the MoS₂ can be used as passive-mode locker and Q switching device. And as reverse saturable absorption occurs at higher intensity the MoS₂-TiO₂ composite might work as optical limiter or all-optical switching application.

In 2016 Wang et al. experimented on SSPM technique with MoSe₂ nanosheets[49]. In this experiment they have systematically investigated the SSPM phenomenon of MoSe₂ nanosheets in solution dispersed form. They calculated the $\chi^{(3)}_{\text{monolayer}}$ to be $1.1 \times 10^{-9} \text{ esu}$ at 532 nm laser excitation.

In 2020 Chunmei Song et al. experimented with boron nanosheets which possess unique properties like photosensitivity, photo response and optical nonlinearity[50]. In this experiment authors have shown that interaction between boron nanosheets and incoming light produces diffraction pattern in the far field which is concentric in nature. Their work showed that the SSPM effect of the boron nanosheet is indeed caused by non-local electronic coherence.

In 2022 Biswajit Das et al. experimented with the strong non-linear optical response of 2D MoSe₂ nanoflakes through SSPM and cross phase modulation method[51]. They reported strong coherent interaction of light and MoSe₂ nanoflakes that creates the SSPM pattern. For the light source they have used laser beams of different wavelengths (671 nm, 532 nm, 407 nm). They calculated the non-linear refractive index and the third order non-linear susceptibility by observing the number of rings with varying intensity of the laser beams. This evolution and deformation diffraction ring patterns are analyzed by wind chime model and thermal effect. An all-optical diode has been investigated on MoSe₂-SnS₂ heterojunction to demonstrate non-reciprocal light propagation. Few other optical devices based on MoSe₂ and other semiconducting materials such as Bi₂Se₃, CuPc and graphene has been investigated. They also demonstrated all optical logic gate operation using cross-phase modulation method which uses two laser beams.

2.3 References

1. Han, Z., et al., *Ultralow-cost, highly sensitive, and flexible pressure sensors based on carbon black and airlaid paper for wearable electronics*. 2019. **11**(36): p. 33370-33379.
2. Pan, Y., Z. Lyu, and C.J.O.C. Wang, *All-optical switching in azo dye doped liquid crystals based on spatial cross-phase modulation*. 2021. **4**(11): p. 2714-2720.
3. Jian, M., et al., *Flexible and highly sensitive pressure sensors based on bionic hierarchical structures*. 2017. **27**(9): p. 1606066.
4. Ma, Y. and L.J.S.M. Zhi, *Graphene-based transparent conductive films: material systems, preparation and applications*. 2019. **3**(1): p. 1800199.
5. Gong, S., et al., *A wearable and highly sensitive pressure sensor with ultrathin gold nanowires*. 2014. **5**(1): p. 1-8.
6. Kim, H.-J., et al., *Highly sensitive and very stretchable strain sensor based on a rubbery semiconductor*. 2018. **10**(5): p. 5000-5006.
7. Gao, L., et al., *All paper-based flexible and wearable piezoresistive pressure sensor*. 2019. **11**(28): p. 25034-25042.
8. Mirica, K.A., et al., *Mechanical drawing of gas sensors on paper*. 2012. **124**(43): p. 10898-10903.
9. Liu, H. and R.M.J.A.c. Crooks, *based electrochemical sensing platform with integral battery and electrochromic read-out*. 2012. **84**(5): p. 2528-2532.
10. Zhang, Y., et al., *Flexible paper-based ZnO nanorod light-emitting diodes induced multiplexed photoelectrochemical immunoassay*. 2014. **50**(12): p. 1417-1419.

11. Kurra, N., D. Dutta, and G.U.J.P.C.C.P. Kulkarni, *Field effect transistors and RC filters from pencil-trace on paper*. 2013. **15**(21): p. 8367-8372.
12. Jiang, M.-J., Z.-M. Dang, and H.-P.J.A.P.L. Xu, *Giant dielectric constant and resistance-pressure sensitivity in carbon nanotubes/rubber nanocomposites with low percolation threshold*. 2007. **90**(4): p. 042914.
13. Chen, L., et al., *Silicone rubber/graphite nanosheet electrically conducting nanocomposite with a low percolation threshold*. 2007. **28**(4): p. 493-498.
14. Tao, L.-Q., et al., *Graphene-paper pressure sensor for detecting human motions*. 2017. **11**(9): p. 8790-8795.
15. Tien, N.T., et al., *A flexible bimodal sensor array for simultaneous sensing of pressure and temperature*. 2014. **26**(5): p. 796-804.
16. Wang, X., et al., *Harvesting ambient vibration energy over a wide frequency range for self-powered electronics*. 2017. **11**(2): p. 1728-1735.
17. Luo, N., et al., *Flexible piezoresistive sensor patch enabling ultralow power cuffless blood pressure measurement*. 2016. **26**(8): p. 1178-1187.
18. Mohammad Haniff, M.A.S., et al., *Piezoresistive effects in controllable defective HFTCVD graphene-based flexible pressure sensor*. 2015. **5**(1): p. 1-10.
19. Liu, Y., et al., *Flexible, highly sensitive pressure sensor with a wide range based on graphene-silk network structure*. 2017. **110**(12): p. 123508.
20. Fu, X.-W., et al., *Strain dependent resistance in chemical vapor deposition grown graphene*. 2011. **99**(21): p. 213107.
21. Tian, H., et al., *A graphene-based resistive pressure sensor with record-high sensitivity in a wide pressure range*. 2015. **5**(1): p. 1-6.
22. Yao, H.B., et al., *A flexible and highly pressure-sensitive graphene-polyurethane sponge based on fractured microstructure design*. 2013. **25**(46): p. 6692-6698.
23. Pataniya, P.M., et al., *Flexible paper based piezo-resistive sensor functionalised by 2D-WSe₂ nanosheets*. 2020. **31**(43): p. 435503.
24. Pataniya, P.M., et al., *Highly sensitive and flexible pressure sensor based on two-dimensional MoSe₂ nanosheets for online wrist pulse monitoring*. 2021. **584**: p. 495-504.
25. Kim, S., et al., *Wearable, ultrawide-range, and bending-insensitive pressure sensor based on carbon nanotube network-coated porous elastomer sponges for human interface and healthcare devices*. 2019. **11**(26): p. 23639-23648.
26. Song, D., et al., *Hollow-structured MXene-PDMS composites as flexible, wearable and highly bendable sensors with wide working range*. 2019. **555**: p. 751-758.
27. Li, Y., et al., *Highly flexible strain sensor from tissue paper for wearable electronics*. 2016. **4**(8): p. 4288-4295.
28. de Oliveira, J.G., et al., *A silver nanowire-based flexible pressure sensor to measure the non-nutritive sucking power of neonates*. 2020. **8**(1): p. 1-8.
29. Jeong, H., et al., *Flexible resistive pressure sensor with silver nanowire networks embedded in polymer using natural formation of air gap*. 2019. **174**: p. 50-57.
30. Wang, G., et al., *A flexible pressure sensor based on composite piezoresistive layer*. 2021. **22**(1): p. 405-411.
31. Li, J., et al., *Ultrasensitive, flexible, and low-cost nanoporous piezoresistive composites for tactile pressure sensing*. 2019. **11**(6): p. 2779-2786.
32. Maiman, T.H., *Stimulated optical radiation in ruby*. 1960.
33. Zipfel, W.R., R.M. Williams, and W.W.J.N.b. Webb, *Nonlinear magic: multiphoton microscopy in the biosciences*. 2003. **21**(11): p. 1369-1377.
34. Phillips, K.C., et al., *Ultrafast laser processing of materials: a review*. 2015. **7**(4): p. 684-712.
35. Zakery, A. and S.J.J.o.N.-C.S. Elliott, *Optical properties and applications of chalcogenide glasses: a review*. 2003. **330**(1-3): p. 1-12.

36. Nguyen, T.-P.J.S. and C. Technology, *Polymer-based nanocomposites for organic optoelectronic devices. A review*. 2011. **206**(4): p. 742-752.
37. Callen, W., B. Huth, and R.J.A.p.l. Pantell, *Optical patterns of thermally self-defocused light*. 1967. **11**(3): p. 103-105.
38. Stolen, R.H. and C.J.P.R.A. Lin, *Self-phase-modulation in silica optical fibers*. 1978. **17**(4): p. 1448.
39. Novoselov, K.S., et al., *A roadmap for graphene*. 2012. **490**(7419): p. 192-200.
40. Wu, Y., et al., *Emergence of electron coherence and two-color all-optical switching in MoS₂ based on spatial self-phase modulation*. 2015. **112**(38): p. 11800-11805.
41. Wang, Y., et al., *Distinguishing thermal lens effect from electronic third-order nonlinear self-phase modulation in liquid suspensions of 2D nanomaterials*. 2017. **9**(10): p. 3547-3554.
42. Karimzadeh, R.J.J.o.o., *Spatial self-phase modulation of a laser beam propagating through liquids with self-induced natural convection flow*. 2012. **14**(9): p. 095701.
43. Wang, G., et al., *Tunable effective nonlinear refractive index of graphene dispersions during the distortion of spatial self-phase modulation*. 2014. **104**(14): p. 141909.
44. Shan, Y., et al., *Two-dimensional Bi₂S₃-based all-optical photonic devices with strong nonlinearity due to spatial self-phase modulation*. 2019. **8**(12): p. 2225-2234.
45. Jia, Y., et al., *Broadband nonlinear optical resonance and all-optical switching of liquid phase exfoliated tungsten diselenide*. 2018. **6**(11): p. 1040-1047.
46. Li, J., et al., *Broadband spatial self-phase modulation and ultrafast response of MXene Ti₃C₂T_x (T= O, OH or F)*. 2020. **9**(8): p. 2415-2424.
47. Miao, L., et al., *Ultrafast nonlinear optical response in solution dispersions of black phosphorus*. 2017. **7**(1): p. 1-8.
48. Li, X., et al., *Enhanced nonlinear optical response of rectangular MoS₂ and MoS₂/TiO₂ in dispersion and film*. 2016. **120**(32): p. 18243-18248.
49. Wang, W., et al., *Coherent nonlinear optical response spatial self-phase modulation in MoSe₂ nano-sheets*. 2016. **6**(1): p. 1-6.
50. Song, C., et al., *Liquid phase exfoliated boron nanosheets for all-optical modulation and logic gates*. 2020. **65**(12): p. 1030-1038.
51. Sk, K., et al., *Nonlinear Coherent Light–Matter Interaction in 2D MoSe₂ Nanoflakes for All-Optical Switching and Logic Applications*. 2022: p. 2200791.

Chapter 3

Instruments

Chapter 3: Instruments

In this Chapter a detailed discussion is done on the Characterization tools and equipment that were used in the thesis work.

3.1.1 Crystal Structure Analysis:

X-Rays were discovered by Willhem Conrad Rontgen in the year 1895, just as the studies on crystal structures were being done. Initially physicists were not sure about the exact nature of the X-Rays, although it was suspected that it was some form of electromagnetic radiation, in other words a form of light. The X-Ray can be used in many purposes but for characterization it can determine the structure of any material. Each material has unique characteristics when exposed to X-Ray beam which can be used for the identification purpose of the material. Once the material has been identified the data/pattern can be used to identify the properties of the powder material. X-Ray crystallography can be used to how the atoms pack together in the crystalline state and the interatomic distance and angles are etc. X-Ray diffraction is one of the important tools used in solid state chemistry or material science. We determine the shape and the size of the unit cell for any compound, easily using X-Ray diffraction.

3.1.2 Diffraction:

Diffraction is the slight bending of the light as it passes through an edge of an object. The amount of bending depends on the relative size of the wavelength of the light to size the opening. If the opening is much larger than the wavelength then the bending will not be much noticeable. Diffraction is a scattering phenomenon. For solid crystals arranged in the periodic manner with constant atomic distances. For diffraction to happen the wavelength

Chapter 3: Instruments

of incident rays must be comparable to the interatomic spacing i.e few order of nanometer. X-Rays have wavelength in order of .03 nm to 3 nm which makes them suitable for diffraction phenomenon occurring on the material. When a beam of X-Ray is incident on the solid material surface, a portion of the beam will be scattered in all the directions. Since the atoms are arranged in a periodic manner in a material, the rays scattered by them have a definite phase difference. These phase relation is such that most cases destructive interference occurs, when the beam has constructive interference the intensity increase. This allows pattern to be formed in the X ray diffraction pattern.

3.1.3 X-Ray Generation:

X-Ray can be generated by bombarding metal target with high energy electrons from a hot filament (often tungsten). The high energy electron must penetrate through the outer shells and interact with the inner shell electrons. If more than a critical energy is transferred to the inner shell the electron can be ejected. This electron leaves the shell leaving a vacant space behind. The ionized atoms return to its original state or lowest energy state by filling the vacant space. When this electron refills the vacant space it emits its energy in the detector direction, which is later identified and detected.

3.1.4 Interplanar Spacing and Bragg's Law:

The basic law that is involved with the diffraction is Bragg's Law. For crystalline material we can consider there is two plane of atoms arranged on top of each other. Where the spacing between the interatomic distance is 'd'. Considering two parallel rays coming from a distance gets impinged on the plane. The Ray 1 reflects off the upper atomic upper plane at an angle θ equal to the angle of the incident. The Ray 2 reflects off from the lower atomic

Chapter 3: Instruments

plane at same angle θ . The Ray 2 travels a distance $2d\sin\theta$ more than Ray 1. If this travelled path is integral multiple of the wavelength, then the interference will be constructive otherwise destructive interference will occur. Thus, the condition for constructive interference will be,

$$2d\sin\theta = n\lambda$$

This condition is called the Bragg's law. Here the wavelength λ is the wavelength of the incident X-Ray, n is an integer and d are the spacing between two atomic planes and θ is the angle of the incident X-Ray on the atomic plane.

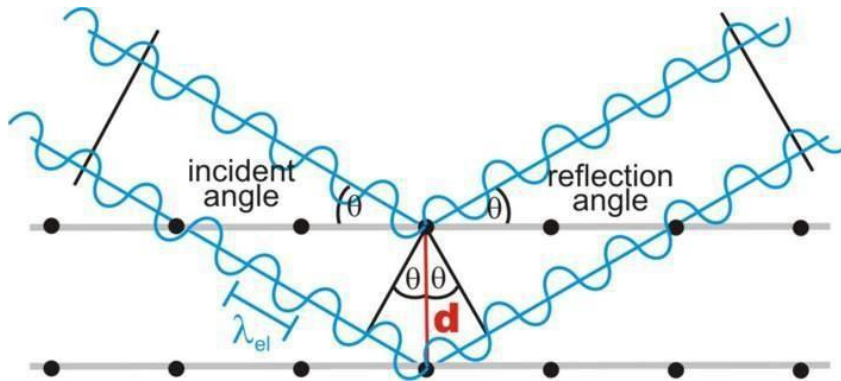


Fig.3.1: X-Ray diffraction from the crystal plane satisfying Bragg's Law

3.1.5 Uses of X-Ray Diffraction:

1. Measurement of interplanar spacing (d_{hkl}) : Diffraction is got when X-Ray interacts constructively with the atoms of the sample placed in lattice planes having (hkl) miller indices with spacing d_{hkl} . This interplanar spacing can be got from the Bragg's Law itself,

$$2d_{hkl}\sin\theta = n\lambda \quad \text{-----(3.1)}$$

where λ is wavelength of X-Ray, θ is angle of diffraction, d_{hkl} is interplanar spacing.

Chapter 3: Instruments

2. Determination of Lattice Parameter: A crystal is a periodic arrangement of atoms which is called lattice and the atoms are denoted by lattice points or basis which extended in all direction along three crystallographic axes. Now a, b, c (the length along this crystallographic axes) and α, β, γ (angle between the sides) are lattice constants or lattice parameters which can be also determined by XRD, as this parameters are related to the interplanar spacing d and the miller indices hkl . For cubic lattice ($a=b=c$, $\alpha=\beta=\gamma=90^\circ$) lattice parameters are determined as,

$$d^2 = \frac{a^2}{h^2 + k^2 + l^2} \text{ -----(3.2)}$$

For hexagonal lattice ($a=b$, $c=5.993\text{\AA}$, $\alpha=\beta=90^\circ$, $\gamma=120^\circ$) lattice parameters are given by,

$$\frac{1}{d^2} = \frac{4}{3} \left(\frac{h^2 + k^2 + hk}{a^2} \right) + \frac{l^2}{c^2} \text{ -----(3.3)}$$

This relation depends on the type of lattice.

3. Determination of Crystallite Size: The crystallite size can be determined using Scherrer

formula given by, $D = 0.9\lambda / \beta \cos\theta$ -----(3.4)

where D is the average crystallite size, $\lambda = 1.541 \text{\AA}$ (X-Ray wavelength), β is the width of the diffraction peak at half maxima for the diffraction angle 2θ which is also known as FWHM.

4. Phase Identification: The generated XRD spectrum is matched with the JCPDS card no. stored in JCPDS file. There are various JCPDS card for every organic and inorganic

Chapter 3: Instruments

materials. Among these the suitable card is compared with the obtained spectrum. Like this this the phase of the sample is identified.

3.2 Morphological Analysis:

3.2.1 Field Emission Scanning Electron Microscopy

The SEM or scanning electron microscopy is one of the most versatile instruments that is used for analysis of the microstructure morphology. SEM utilizes a focused electron beam to scan the surface of the sample, that produces large number of signals. These electron signals are converted into electrical signals that is displayed on the CRT monitor.

This electron beam can be produced in two different ways

- Thermionic emission
- Field emission

For thermionic emission the beam is controlled via controlling the electron generation through thermal energy. For modern electron microscope the field emission gun is being used. As it is a good alternative to thermionic gun. FESEM can be used to image very small topographic details on the surface of the material (~5nm). Researchers in many field biology, chemistry, physics, material science apply this technique to observe structures that are very small in dimension (~1nm).

FESEM can be used to study different morphology, coating on a film etc.

Chapter 3: Instruments

1. Sample Preparation:

For FESEM to operate high energy electron beam is incident on the sample. For this high vacuum is necessary otherwise the any air molecule will get ionize and will interfere with the reading. Also, this means that liquid or other sample containing water or moisture is strictly prohibited for FESEM imagery. The powder sample must be fixed on the specimen holder so that the powder does not contaminate the SEM specimen chamber. Non-conductive tape is attached on the specimen holder so that the sample does not fall off from the holder. Generally, Carbon tape is used for such kind of purpose, for non-conductive material Au, Ag, Pt coating is done on the sample to make it conductive. It is generally done using sputtering method.

2. Components or different parts of FESEM

(i) Electron Gun:

Modern FESEM system requires an electron gun which produces steady flow of electron beam with high energy, small spot size, adjustable energy and small energy dispersion. Several types of gun are used in FESEM, they differ generally using the type of working principle they are working on. First FESEM system incorporated thermionic gun, that works thermionic emission. For this type of gun tungsten hairpin is used. A high voltage is applied along with high temperature on the filament that produces electron beam. For modern FESEM lanthanum hexaboride (LaB_6) is used as an electron source, this type of gun is used field-emission purpose. This provides enhanced current and low energy dispersion. Also, the electron guns have lifetime after which they lose their use.

(ii) Electromagnetic Lenses:

Chapter 3: Instruments

Electron beam can be focused by electrostatic lenses or magnetic lenses. Electron beam operated using magnetic field has a small aberration, so only magnetic field is employed in SEM system. The trajectories of the electron beam can be controlled using electromagnets. In a magnetic field the electron experiences Lorentz force.

$$F = -e(E + v \times B).....(3.5)$$

$$F = evB\sin(\theta, B).....(3.6)$$

Here e is charge of the electron, v is the velocity of the electron in the magnetic field,

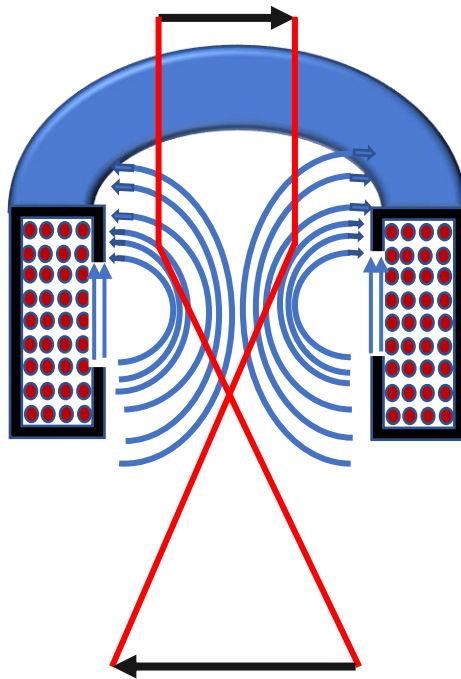


Fig.3.2 Cross-sectional schematic of an electromagnetic Lens

A magnetic lens consists of coil of copper wires inside iron pole pieces, a current through these copper wire creates a magnetic field which is noted in blue color. The rotationally symmetric magnetic field is homogeneous in nature, and it is such that weak in the center of the gap and stronger closer to the bore. Electrons close to the center are strongly

Chapter 3: Instruments

deflected than to those passing the lens from far. The resulting force F is perpendicular to both v and B .

(iii) Condenser Lens:

The electron beam will diverge after passing through anode plate, from emission source. By the use of the condenser lens the electron beam is converged into parallel stream of electron beams. This electron beam is incident upon the sample. A magnetic lens consists of two symmetrically iron pole piece in which there is copper winding wound around the pole shoes. There is a hole in the pole shoes through which electron passes through. The focus point and the length can be changed using the current in the coil. The focusing effect of the magnetic coil increases with the magnetic field B , which can be controlled via the current passing through the copper wire.

(iv) Scan Coils:

The scan coils deflect the electron beam over the object according to a zigzag pattern. The formation of the image on the monitor occurs according to the scan movement. This scan velocity determines the refresh rate of the screen and the noise recorded. Scan velocity determines the rate at which the monitor is able to load the picture after zooming in the sample repeated times. Scan coils often consists of upper and lower coils, which prevents formation of circular shadow at low magnification.

In case of Condenser lens the distance from the point where electron beam starts to bend towards the axis to the point where it crosses the axis is called the lens focal length, given by the equation (3.4),

Chapter 3: Instruments

$$\frac{1}{f} = \frac{1}{a} + \frac{1}{b} \dots \dots (3.7)$$

where f is the focal length, a is the distance of the point where electron beam starts to bend from the lens, b is the distance of the point where it crosses the axis from the lens. Therefore, the magnification is given by,

$$M = b/a \dots \dots \dots (3.8)$$

Thus, the electron probe becomes narrower if the lens action of the condenser lens is strengthened as the ratio b/a gets smaller. There is an aperture placed between the condenser lens and the objective lens. It is a thin metal plate with a small hole which allows a part of the electron probe, which passes through the condenser lens, to reach the Objective lens. Because of this aperture the probe current is adjusted accordingly with the excitation condenser lens. Thus, the Condenser lens enables us to change the electron probe diameter and probe current. While the is used for focusing and for determining the final diameter of the electron probe. So, the objective lens should always be made that has best performance.

(v) Objective Lens

The electron beam will converge below the condenser aperture. Objective lens is solely used for probing the electron beam onto the sample. The spot size can be determined using this lenses smaller spot size leads to more magnification and enhanced resolution.

(vi) The Stigmator Coil:

Chapter 3: Instruments

This type of coil is used to correct the irregularities in the x and y deflections of the beam thus to obtain a perfect beam shape. When the beam is not circular the image looks blurred and stretched in the monitor.

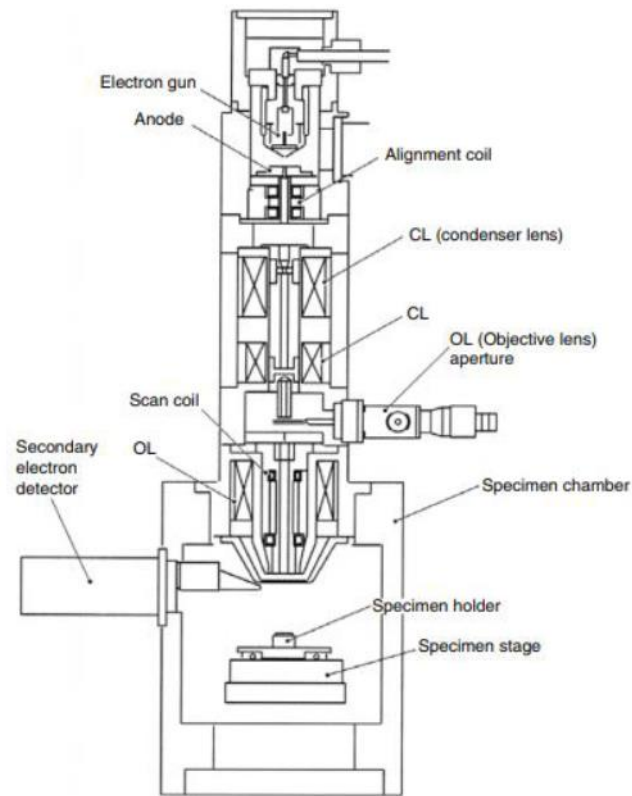


Fig. 3.3 Schematic diagram of cross-section of FESEM

(vii) Objective Chamber:

After the sample has been covered using a conductive layer, it is mounted on a special holder. The object is inserted in the chamber through an exchange chamber. After that the whole column is vacuumed using different pump. The sample holder is then mounted on a movable stage. The secondary electron emission detector is located at the rear of the object holder in the chamber.



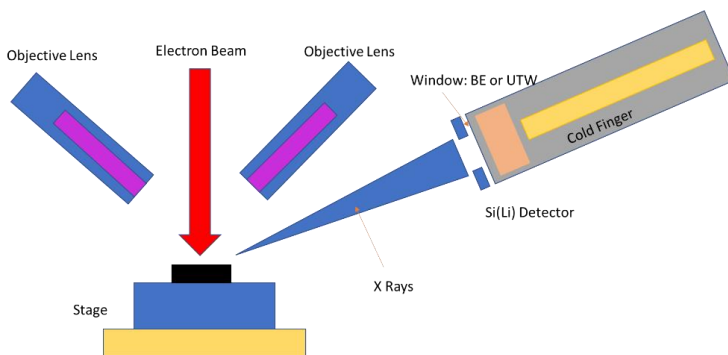
Fig.3.4 FESEM (Hitachi S-4800) set up

3. Image Formation:

Complex interaction occurs when electron beam is incident upon the sample surface and various signal is generated for SEM observations. This signals are backscattered electrons, transmitted electrons, secondary electrons etc. This type of signals is collected and can be displayed and these type of signals reveal the composition of the material. For composition analysis excited X-Ray and auger electrons are analyzed.

3.2.2 Energy Dispersive X-Ray Spectroscopy (EDS/EDX):

Energy dispersive X ray spectroscopy often referred as EDS or EDAX, is an X-Ray technique used for identification of elemental composition of materials. The Energy Dispersive X-Ray Spectrometer (EDS) is used to analyses the Characteristic X-Ray spectra by measuring the energies if the X-Rays. In SEM when the electron probe strikes the specimen then Characteristic X-Ray is also produced along with secondary electrons and backscattered electrons. These X-Rays are analyzed using EDX, which is connected with the FESEM instrument. The emitted X-Rays from the specimen enters the semiconductor, in which electron-hole pair is created whose quantities correspond to the X-Ray energy. The X-Ray spectra is got as X-Ray counts versus X-ray energy. The distribution of specific elements in the specimen can be achieved from Mapping or Area Analysis. It displays 2D distributions of elements of interest in a specific area of the specimen, irradiated by electron probe. EDX can perform on wide range of element and can analyses multi-element simultaneously, with fast measuring speed. Thus, EDX is an important characterization tool, which is done along with FESEM.



Schematic of a Energy Dispersive Spectrometer

Fig.3.5 Schematic Diagram of Energy Dispersive Spectrometer

Chapter 3: Instruments

FESEM imaging system is fully electronic system, not any kind of optical imagery is applied here. The SEM imaging involves discrete events which can be mapped using different kind of signals generated from the sample. At each point of the specimen surface the probe strikes, the number of backscattered electrons and secondary electrons detected gives direct information of the specimen and magnification is achieved by scanning an area on the specimen.

3.2.3 Transmission electron microscopy:

In case of TEM higher energy electrons (λ is about 0.005 nm) are used so that it can penetrate distances of several microns (μm) into thin solid. A beam of electron is made to pass through a ultrathin specimen and the electron beam interacts with the specimen. And an image is formed from the interaction of electron with the sample. For a crystalline solid the electrons are diffracted from the atomic planes of the solid. Thus, a pattern can be formed from the electrons that have been made to pass through. This image of pattern is formed can be scanned using detector, this image can then be formed.

Electron gun and focusing system: This consist of electron generation and focusing system. This electron gun is the source of monochromatic electron beam source. The beam is focused using two kind of condenser lens, the first lens usually determines the spot size, the size range of the electron beam that strikes the sample. The second lens that is controlled by the intensity or the brightness knob changes the spot size onto the sample.

Electron Gun the electron gun produces electron beam with high kinetic energy, enough to enable them to penetrate and pass-through thin areas of the specimen. In the electron gun the cathode is kept at high negative potential and works as an electron source. Also,

Chapter 3: Instruments

in the electron accelerating chamber electrons are accelerated to their final kinetic energy due to huge potential between cathode and anode. There are many types of electron gun depending upon the emission of electrons which operates on different physical principles, like Thermionic Emission Electron gun (TE Gun), Field Emission Electron gun (FE Gun), Schottky Emission Electron gun (SE Gun).

(i)Electron Gun: The electron gun is used for producing electron beam with high kinetic energy, enough to enable them to penetrate and pass through the thin areas of the specimen. In the electron gun there is a cathode which is kept at a high negative potential and works as an electron source. Also, there is an electron-accelerating chamber, where after emission the electrons are accelerated to their final kinetic energy because of the high accelerating potential between the cathode and anode. There are many types of electron gun depending on the type of electron source which operates on different physical principles, like Thermionic Emission Electron gun (TE Gun), Field Emission Electron gun (FE Gun), Schottky Emission Electron gun (SE Gun).

(ii)Condenser Lens System: TEM produces highly magnified image of the sample. To make this possible two condenser lens are typically installed in a TEM. The first condenser lens is a strong magnet, it uses virtual electrons as its object and produces electron beam of certain diameter. This lens mainly provides the magnification action of about $0.4\ \mu\text{m}$ for a Wehnelt filament used in TE gun. The first condenser lens also controls the diameter of the spot size and the second condenser lens is a weaker magnet by comparison, but produces magnification on the sample. But the electron beam allows the beam diameter to be varied continuously over wide range. There is a small hole or aperture just below the polepieces of second condenser lens. It controls the convergence semi-angle (deviation

Chapter 3: Instruments

angle from the optic axis) of the incoming beam. Actually, the beam is constricted by the aperture this cause to knock out electrons of high kinetic energy all those who are far away from the axis. The condenser lens system also contains a stigmator coil to correct the residual astigmatism of both condenser lens system. Lastly, the illumination system contains two pairs of coils. One pair produces uniform magnetic fields in horizontal direction, to shift the electron beam horizontally and another pair adjusts the angle of the incident electron beam relative to the optic axis. These two pairs of coils are called Illumination Shift and Tilt Controls.

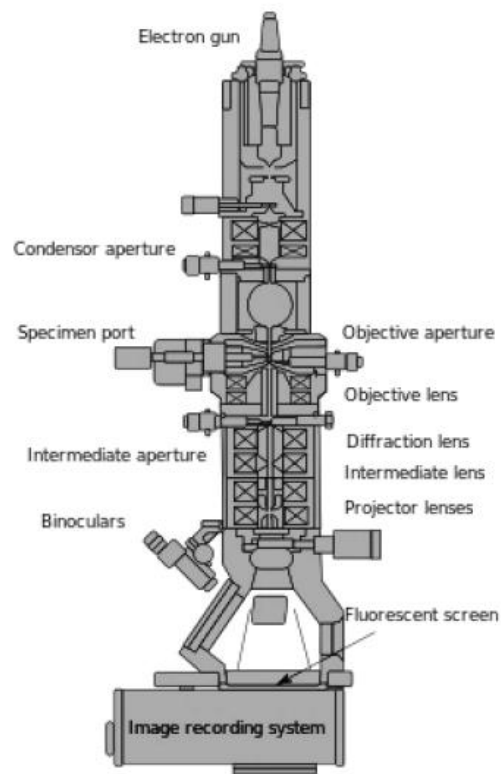


Fig.3.6 Schematic cross-sectional diagram of a Transmission Electron Microscope.

(iii) Specimen Stage

TEM specimen stage s designed in such a way that it can hold the specimen without toppling the specimen, so that there is no movement to the image while the imaging is

Chapter 3: Instruments

being done. It must be noted that the specimen sample must be transparent so that electrons can get through the sample and the magnified image can be formed. The specimen stage should be designed such that the specimen is inserted in the vacuum of the TEM column without introducing air. Thus, there is a small chamber which can be evacuated before the specimen is inserted. This is called Airlock.

There are two basic designs of specimen stage:

Side Entry Stage: Here the specimen is clamped close to the end of a rod like specimen holder and the specimen is inserted horizontally through the airlock.

Top-Entry Stage: Here the specimen is clamped to the bottom end of a cylinder-shaped holder that is equipped with a conical collar. By the means of sliding and tilting arm, the holder is loaded through an airlock.

(iv) Imaging system

TEM imaging system consists of,

A. Objective Lens System: Objective lens system is the closest system to the specimen, with a small focal length. It often experiences high excitation current so it is cooled using water coolant. This lens produces a magnified real image of the specimen below the center of the lens. Objective lens is referred to an Immersion lens also as the specimen is usually located within the pre-field of the lens. This Objective pre-field exerts a strong focusing effect on the incident illumination making it into a nanoprobe of typical diameter 1 – 10 nm. The combination of second condenser lens and objective condenser lens is called condenser-objective lens system. The post field of the imaging

Chapter 3: Instruments

system works as the first imaging lens with small focus. At the Back Focal Plane (BFP) of the post-field of the objective lens, a objective diaphragm can be inserted around an aperture which is called Objective Aperture. BFP is the plane at which a diffraction pattern of the specimen is formed. Electrons which are deflected far from the central axis gets absorbed using diaphragm, so that they don't distort the final image. This also reduces the distortions caused by the spherical and chromatic aberrations. This also minimizes the astigmatism and the streaking effect of an objective stigmator.

- B. **Selected-Area Diffraction (SAD) Aperture:** In the image plane of the objective lens that contains the first magnified (real) image, a diaphragm can be inserted around a aperture called Selected-Area Diffraction (SAD) Aperture. This causes a limitation in the specimen image that can be formed. Therefore, SAD aperture provides diffraction information with good angular and spatial resolution.
- C. **Intermediate lens and projector lens:** TEM contains several lenses between the objective lens and the final lens, these are called projector lenses. The combined function of all these lenses can be merged together to form intermediate lens. The image magnification can be changed by changing its focal length in small steps. This allows the overall magnification of TEM to be varied over 10^3 to 10^6 . Also, by changing the immediate lens excitation image diffraction pattern can be produced on the TEM screen. Finally, the last lens of TEM imaging system is called Projector Lens. It basically produces an image or diffraction pattern such that it fills up the TEM screen with an overall diameter of several centimeters.

Chapter 3: Instruments

D. **TEM Screen and Camera:** For the imaging purpose a phosphor scree is used which can transform the electrons into visual form. Generally, ZnS (Zinc Sulfide) is used as phosphor screen.



Fig.3.7 HRTEM (JEOL-200 kV)

The main purpose of the REM screen is for viewing the TEM image or diffraction pattern. For this, light optical binoculars are often mounted outside the viewing window which provides some additional magnification. Previously to record TEM image photographic plates were used now for the imaging purpose electronic photodetector devices (Charge coupled detector) were used. Because of this it is possible to save the image in computer memory.

Chapter 3: Instruments

3.3 Raman Scattering

Raman spectroscopy was first discovered by C.V Raman and it was used to investigate the vibrational states of many molecules. In Raman scattering a technique is used where a light of monochromatic light is incident on the sample, then the inelastic scattering of this monochromatic light is recorded. A laser beam is used as the monochromatic light source to irradiate the light spot on to the sample. Inelastic scattering deals with the phenomenon in which the frequency of the photon light changes upon the interaction with the sample. Frequency of the re-emitted photons is shifted up and down in comparison to the original frequency, this is called the Raman Effect. The scattered radiation produced by the Raman effect contains the information about the energies of molecular vibrations and rotations. And these depend on the particular atom and ions that comprises the molecule, the chemical bond that connects them. The chemical bond structure, the symmetry can be found using the Raman spectroscopy. Raman spectroscopy can be used on gaseous, liquid, solid samples. Raman Spectrometer is used to conduct Raman Spectroscopy which is a type of molecular spectroscopy. It is a popular technique for analyzing molecular structure, also it gives the information about the vibrational modes of a molecule. The spectroscopy is used incorporating Raman effect which relies on scattering of light.

The scattering can be elastic, that is, the molecule maintains its initial energy state and incident light scatters with its energy unchanged for which Rayleigh Line at wave number, $\tilde{\nu}$.

The scattering can be inelastic, where molecule is in its ground energy state E_1 after absorbing photon energy the state is E_2 which is higher energy state. Consequently, the

Chapter 3: Instruments

photon is scattered with a smaller energy, $hc\tilde{\nu} - \Delta E$, where, $\Delta E = E_2 - E_1$, and, $hc\tilde{\nu}$ is the incident photon energy. This is raman scattering which gives rise to the raman line with a frequency lower than the incident spectral line denoted by the wave number $\frac{hc\tilde{\nu} - \Delta E}{hc}$. Here wavenumber shift is denoted by the number $\frac{\Delta E}{hc}$. These lines are called stokes line. In this inelastic the molecule with higher energy state E_2 loses energy and comes to ground energy state E_1 . Thus, the scattered photon energy is increased, $hc\tilde{\nu} + \Delta E$. For this Raman line with higher spectral raman line occurs with wave number $\frac{hc\tilde{\nu} + \Delta E}{hc}$. These lines are called anti-stoke line. Therefore, Stokes line and Anti-Stokes line occurs symmetrically on the either side of Rayleigh line and thus, the Raman Shift is, $\Delta\tilde{\nu} = \Delta E/hc$, which is equal to the energy difference between the incident and scattered photon. From the experiment we can get information about molecular vibration energy by plotting the resulting spectrum between scattered light intensity versus Raman shift.

(i) Basic Parts of Raman Spectrometer

The basic part of the Raman spectrometer is the light-source, Raman tube, spectrograph, detectors.

Source: The source here used is intense light source capable of producing monochromatic light. A mercury lamp or a discharge lamp is used for this purpose. The most suitable light source is the laser light capable of producing high intensity light. This laser light can be used to focus the beam of light as a spot on the sample using a lens. Monochromator is also used for a better purpose.

Chapter 3: Instruments

Raman Tube: In case of liquid samples, Raman tube is used in thin wall glass called cuvette. This is 15 cm long and 2 cm in diameter in dimension, whose one end is closed with a glass or quartz plate and the other end is covered with a black tape. The sample solution is poured in this tube. The flat end of this tube serves as the window for the scattered light to emerge, while blackened end causes total reflection of back scattered light.

Filters: In case of Raman scattering the intensity of the Raman scattering is very less than the Rayleigh scattering. Hence it is tough to distinguish between two kind of scattering. So, it is required to separate them with precautions. For this purpose, a notch or long-pass optical filters are used. Also, the reflected laser signal is required to be separated which can be done by a laser rejection filter. For this to happen, a notch or a long pass optical filter are used. Also, the reflected laser signal is required to be separated, this can be done using a laser rejection filter.

Spectrograph: This is an instrument which separates the incoming light depending on the frequency, it works just like prism. It also records or maps the resulting spectrum. This is required to separate the Raman lines of different frequency of the scattered light after it is filtered. In most of the Raman Spectrometer a good prism spectrograph is used.

Detectors: Modern Raman Spectrometer uses arrays of CCD (charge coupled diode) that is capable of distinguishing between different frequencies. The spectral range depends on the size of the CCD and the focal length of spectrograph used. Also, in some Raman spectrometer an interferometer is used for detection by Fourier transform method. They are always used with NIR photodetectors. These lasers used depends on the exciting

Chapter 3: Instruments

wavelength. Basically, InGaAs is used as laser source material. It can be found that Raman spectroscopy yields same result as infrared spectroscopy, but gives complementary results.

(ii) Working principle

When a sample is irradiated with monochromatic light source (usually laser source), most of the light is incident on the sample and the same wavelength incident on the sample as of incoming radiation and it gets scattered following the process known as Rayleigh scattering. However, a small portion of photon typically one in million gets scattered in different wavelength that of



Fig.3.8 Raman Spectrometer (WITec ALPHA300 RS).

incoming beam. The Raman effect is based on the molecular deformations in electric field determined by molecular probability α . The laser beam can be considered as oscillating

Chapter 3: Instruments

electromagnetic wave of electric field vector E . upon interaction with the sample the electric field deforms the sample and produces an electric dipole moment ($P=\alpha E$) in the molecule. Because of the periodic deformation molecules starts oscillating with another frequency ν_m an amplitude of the vibration called a nuclear displacement. In other words, the monochromatic light of the frequency ν_0 excites molecules and transform them into oscillating dipoles. Depending upon the scattering and the change in the frequency Raman Spectroscopy can be classified as,

1. Rayleigh Scattering: A molecule with no Raman active mode absorbs a photon with frequency ν_0 , as an excitation source and emits radiation of the same frequency. This type of scattering is known as elastic Rayleigh scattering.
2. Stokes: A photon with frequency ν_0 is absorbed by the Raman active molecule which in time of absorption is in basic vibrational state. Part of the photon's energy is transferred to the Raman active molecule with frequency ν_m emits a photon light of the frequency $\nu_0 - \nu_m$. This Raman frequency is called stokes frequency or just 'Stokes'.
3. Anti-Stokes: A photon with frequency ν_0 is absorbed by the Raman active material, which at the time of absorption is already in excited vibrational state. Excessive energy of the Raman active mode is released, molecules return to its original vibrational state and the resulting frequency of the scattered light is increased up to $\nu_0 + \nu_m$. This Raman frequency is called Anti-stokes frequency or just anti-stokes.

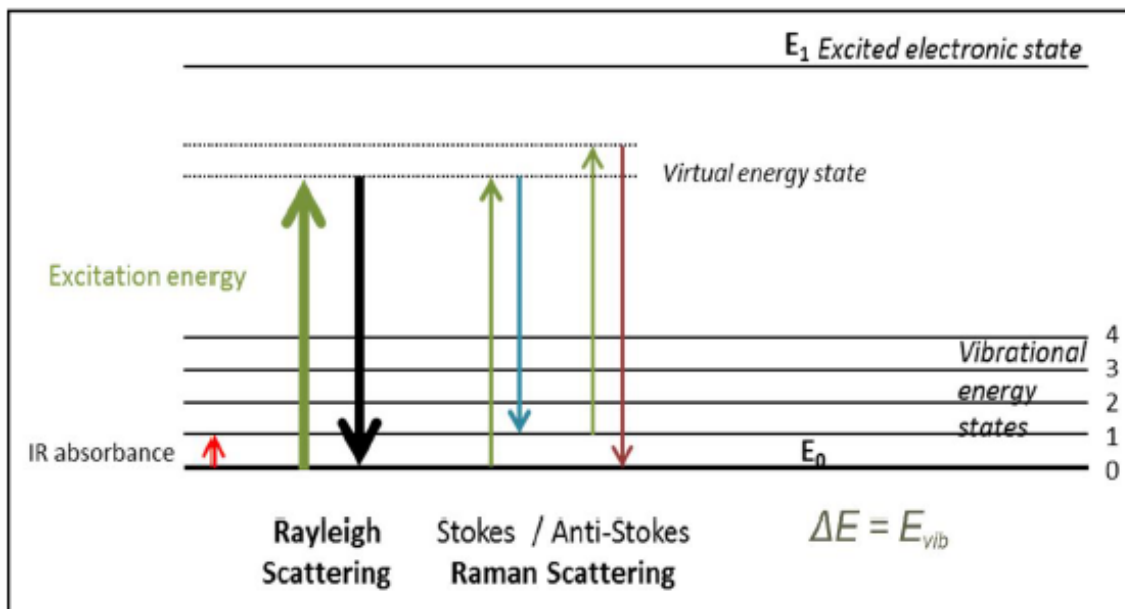


Fig.3.9: Different scattering of the Raman Spectra.

3.4 Atomic Force Microscopy

Atomic force microscopy or scanning force microscopy is a very high-resolution type microscopy capable of resolution of few nm and more than 1000 times better optical diffraction limit. Here the surface information is gathered by touching the surface using mechanical probe. Piezoelectric elements are used as a tip for this kind of microscopy, and the tip progresses this kind of precise movement.

The AFM has three major kind of abilities: force measurement, topographic imaging and manipulation.

1. In the force measurement the probe can be used to measure the forces between the probe and the sample as a function of their mutual separation. This force microscopy can be used to measure mechanical property of the sample. Such as Young's modulus a measure of stiffness.

Chapter 3: Instruments

2. For imaging purposes, the application of forces to the probe that can be used to produce three-dimensional high-resolution image. This kind of imagery is possible by raster scanning the position of the sample with respect to the tip recording the height of the probe that corresponds to the sample-probe interaction.
3. In manipulation the interaction between the sample and the tip can be used to change the properties of the sample in a controlled way. Examples of this kind of manipulations are atomic manipulation, scanning probe lithography etc.

The major difference between AFM and other imaging techniques are that it does not uses any kind of lenses or beam irradiance. Thus, it does not suffer from limitation in in spatial resolution such as diffraction and aberration. The complex beam making procedure is not necessary hence it is more reliable.

(i) **Configurations of a working AFM**

Here the probe is supported by small cantilever, the support is usually a piezoelectric element (typically made of ceramic material), this piezoelectric element oscillates the cantilever in a fixed frequency. A tip is attached to the cantilever this acts as a probe to apply the force and a detector is mounted to record the image or the information. Also, a drive is loaded to move the sample in XYZ direction and record the information using the probe.

According to the configuration shown above the interaction between the tip and the sample which is nanoscale phenomenon can be transduced into change via. The motion of the cantilever, which is a macroscale phenomenon. Several different aspect of

Chapter 3: Instruments

cantilever motion can be used to quantify the interaction between the tip and the sample. Several different aspect of the cantilever motion can be used to quantify the interaction between the sample and the tip.

A laser beam is used to detect the cantilever deflections toward the surface. By reflecting an incident beam off the flat top of the cantilever, any cantilever deflection will cause change in direction of the reflected beam. A position-based photo diode can be used to track these change in position. However, as the cantilever is made in to come in proximity of the surface, but with time increase in repulsive force makes the cantilever to be pushed away.

The AFM can generate accurate topographic image of the sample. The raised and lowered version of cantilever the scanning can be influenced. This deflection is monitored by PSPD (position sensitive photo diode). By this a feedback loop is generated which controls the distance between the tip and the surface. The detector detects this deflection (displacement with respect to equilibrium position) of the cantilever this deflection is converted into an electrical signal. Various method of deflection can be recorded such as interferometry, optical levers, and STM based detectors.

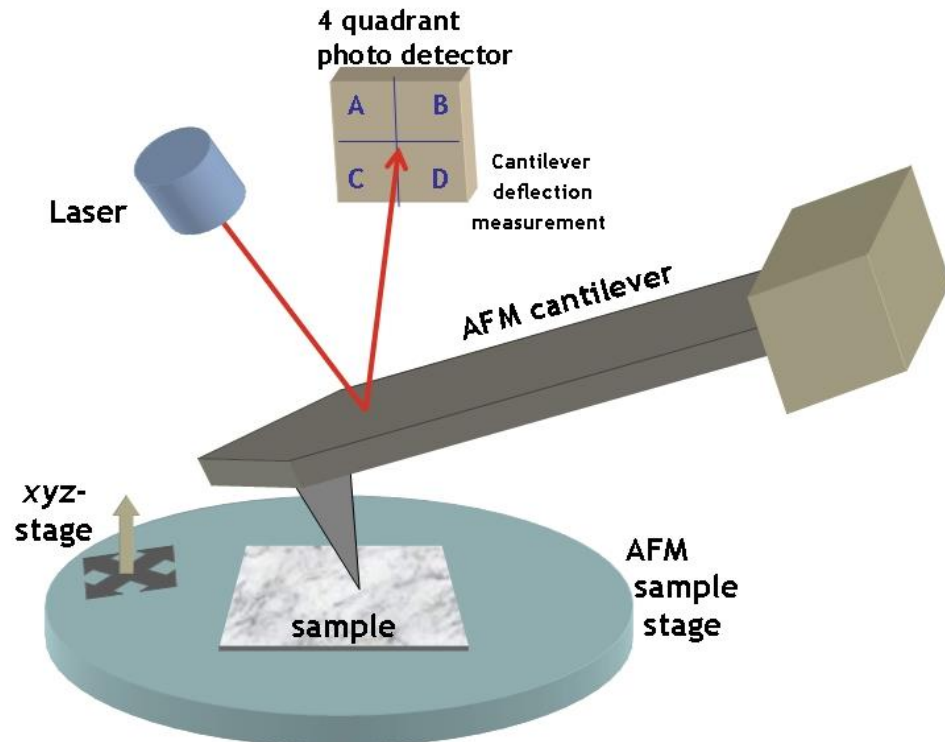


Fig. 3.10. Schematic diagram of Atomic Force Microscopy.

(ii) Image Formation

During the imaging process the tip is brought in contact with the sample. And the sample is raster scanned using atomic force microscopy in the X-Y direction. An electronic feedback loop is employed to make the probe-sample force constant during the scanning procedure. This feedback loop has the cantilever direction as input and the output controls the deflection along the Z axis. As long as the probe remains in contact with the sample the scanning continues. The sample is scanned in the x-y direction and the height in z direction will make the output. The feedback then adjusts the height of the probe so that the deflection remains same throughout the sample scanning. This feedback loop is important for scanning the surface of the sample, this can also adjust the support-sample separation during the scanning period so that the

Chapter 3: Instruments

deflection remains constant throughout the procedure. This feedback is done by servo mechanism.

The AFM consist of sharp tip that is used to scan the surface of the specimen. The cantilever is typically made of silicon or silicon-nitride with a tip radius curvature in nm. When the tip is made to come into the proximity of the surface of the material a deflection occurs on the cantilever. This deflection can be measured using Hooke's Law. The forces that can be measured using the AFM include mechanical contact force, Van der Waals force, capillary force, chemical bonding, electro-static forces, magnetic forces.

The AFM can be operated in different modes possible imaging modes are divided into static modes, dynamic mode. According to the naming the static mode suggests that the static mode is the contact mode. In the tapping mode the tip is dragged across the sample and the contours of the sample is measured using the deflection of the cantilever directly or using the feedback signal used to make the cantilever steady. In contact mode the AFM is almost done at depth where the overall force is repulsive. Because in this mode the AFM output signal is prone to background noise the cantilever is chosen in such a way that it has low stiffness so that it produces large deflection.

In tapping mode, the cantilever is made to oscillate up and down in resonant frequency on the sample surface. The oscillation can be achieved using a small piezo element. The amplitude of this oscillation generally varies from several nm to 200 nm. In this mode the frequency of the cantilever oscillation is made fixed. This is used for sample with liquid meniscus layer.

Chapter 3: Instruments

(iii) Applications

The AFM has been applied into wide variety of applications such as solid-state physics, semiconductor science and technology, molecular engineering, polymer chemistry and physics, surface chemistry, molecular biology, medicine etc. Application in the field of solid -state physics include i) identification of the atom at the surface. ii) the evaluation of interaction between the atoms and their neighboring atoms, iii) study of changes in properties due to change in atomic arrangements. In molecular biology the AFM can be used to study the structure and mechanical properties of protein complexes. AFM has been used to study the microtubules and their stiffness. In cellular biology AFM can be used to distinguish between cancer cells and normal cells based on the hardness of the cells.

3.5 Equipment used for Pressure Sensor Experiment:

The equipment that was used for performing the pressure sensor experiment are:

3.5.1 Keysight B2902A: The Keysight B2902A is Source Measurement unit, that enables user to quickly take various I-V measurements in high accuracy and precision. The results can be viewed easily on the LCD screen without requiring any external connection. When paired up with Quick I-V measurement it can display I-V Curves and other types of curve in front of the monitor. Through this tool it is possible to get accurate measurement of current and voltage. The Keysight B2902A SMU unit integrates many different source and measurement capabilities into one compact form factor.

Chapter 3: Instruments



Fig.3.11. The Keysight B2902A SMU unit.

The Keysight B2902A SMU unit uses banana jack terminals, which can support many accessories. It can detect very low current up to 1 nA. A banana jack to tri-axial cable is used to test fixtures and wafer probers. Also, 2 wire and 4 wire tri-axial cable is available. It offers support to high pin count devices. It also provides high sweep rate than any other SMU unit. In addition, The Keysight B2902A SMU unit supports a trace buffer that can store up to 10,000 data points. This allows multiple data points to be downloaded at the same time.

3.5.2 Hot Air Oven

Hot air ovens are the laboratory equipment that works on dry heat or hot air mixture. It's working principle is mainly on the convection process of dry and hot air. The exterior surface of an item absorbs heat from the hot air and passes on to the next layer. This method was introduced by Louis Pasteur. A hot air oven consists of the following parts: (a) A chamber which is insulated and surrounded by an outer case that contains electric heaters, (b) A fan, (c) Some shelves, (d) A thermostat and (e) Door locking controls. Hot air ovens

Chapter 3: Instruments

are mainly used for sterilization of articles that can withstand temperature and do not get burned like, glass wares, powders, pharmaceutical products like liquid paraffin, fats, grease, etc. Also, it is the only method of sterilizing oils and powders. It is also applicable for Annealing, Die-bond curing, Polyimide baking, in healthcare industry, technology and transportation industry.



Fig.3.12 Hot Air Oven

3.5.3 Calibrated Weights: Calibrated weights have been used for pressure sensing mechanism. These weights are brought from the market and have been used to generate pressure.



Fig.3.13. Calibrated Weights.

3.6 Equipment used for SSPM Experiment

The equipments that were used for performing the SSPM experiment are -

3.6.1 Ultra Sonic Water Bath (Sonicator)

It is a device mainly used for mixing solutions which works on the principle of sonication.

Ultrasonic sound waves (frequency 20-25 kHz) are used to agitate particles in a solution.

This instrument has three parts **(a)** a generator which transforms input electrical power into an electrical signal for driving the transducer, **(b)** a transducer for converting the electrical signal into



Figure 3.14. Ultrasonic Water Bath.

vibration, **(c)** a probe tip to which the vibration is given so that it can be amplified to a longitudinal vibration causing a cavity in the sample solution. This cavitation causes the disruption of the sample and breaks down into smaller ones. Thus, the evenly mixing of

Chapter 3: Instruments

sample in a solution is achieved. It is commonly used in nanotechnology for dispersing nanoparticles evenly in liquids.

3.6.2 LASER Source

A LASER source is a device which can emit an intense, almost perfectly monochromatic, directional, and highly coherent beam of light. The word LASER is an acronym for Light Amplification by Stimulated Emission of Radiation. Thus, its action is based on the stimulated emission predicted by Einstein in 1916. The interaction of radiation with matter can happen in three ways.

(i) *Stimulated Absorption of Radiation*: in this case an atom usually in a lower state rises to higher state by absorbing radiation of frequency, $\nu = (E_2 - E_1)/h$, where E_2 , E_1 are the energies of higher and lower state respectively and h is the Planck's constant.

(ii) *Spontaneous Emission of Radiation*: in this case an atom which is initially in a higher state decays to the lower state, as its lifetime in the higher state is very small (10^{-8} seconds approximately), emitting a photon of frequency, $\nu = (E_2 - E_1)/h$.

(iii) *Stimulated Emission of Radiation*: here an atom in higher state, under the influence of photon frequency ν , decays to the lower state emitting an additional photon of same frequency. The direction of propagation, energy, phase of this emitted photon is exactly same as that of the incident stimulated photon. As a result, the radiation passing through an assembly of atoms is amplified. This, three type of radiation-matter interaction gives rise to the lasing action of the LASER. To have a continuous lasing action it is required to have more population of atoms in the higher state than the lower state which is called Population Inversion. A laser source has three main components – the **Active Medium**

Chapter 3: Instruments

which conducts the lasing action and produces light, the **Pumping Source** for the achievement of population inversion and the **Optical Resonator** for amplification of light. There are many types of laser device – SOLID STATE LASER like Ruby Laser which is a three-level laser; GAS LASER like He-Ne Laser which is four level laser; DIODE LASER which is a semiconductor injection laser.

3.6.3 Laser Power Meter

A Power Meter usually measures the power in an optical signal. Laser Power Meters are used to measure the light power of lasers. These are often Thermopile Laser Sensors which is a series of bimetallic junctions that can sense temperature difference. These power meters work on the principle of a thermal detector converting optical power to heating power via an absorber structure with a black coating. The thermopile measures the resulting temperature difference between the absorber and the mount, which is proportional to the absorbed power. This is how the power meter measures the laser power. It is to be noted that the laser beam must hit the center of the of power meter for maximum power to be measured.

Chapter 4

Wearable, Ultrawide-Range, and Bending-Insensitive Pressure Sensor Based on 2D Bi₂Se₃ NFs coated tissue for Human-machine Interface and Healthcare Devices

Chapter: 4

4.1 Introduction

With the development of modern flexible electronics, pressure sensors have drawn much attention. Flexible pressure sensors can be used in many applications such as health care monitoring[1, 2], human machine interfacing[3-5] and robot prosthetics[6]. In recent years, flexible electronics has been a topic of massive interest due to their application in various fields and they are widely employed as pressure sensors. A novel pressure sensor should have high sensitivity, mechanical flexibility, fast response time, low fabrication cost and simple processing etc. Various sensing mechanisms have been employed to fabricate flexible and sensitive pressure sensors based on piezo-capacitive[6, 7], piezoresistive[8], piezoelectric [9] and tribo-electric effect [10]. Among these types, the piezo-resistive pressure sensor is thought to be the most energy efficient and cost effective as it does not require complex fabrication method, also the signal acquisition method is also easy. To construct a piezo-resistive pressure sensor two main key factors come into play- (i) the active conductive material and, (ii) microstructure of the pressure sensor.

Till date, there has been many report on variation of the active conductive material and microstructure of the pressure sensor and various kind of conductive material has been used such as graphene[11], reduced graphene oxide[12], carbon-nanotubes[13], Au-nanowires [14] and Ag nanowires[15]. Also, there has been variation in the microstructure such as micro-pyramid structure [16], micropillar structure [17], microdome structure[18], the interlocked structure[19], the porous structure[20]. This microstructure can provide more contact points between material and electrode under loading -unloading condition. Pang et al. reported a highly flexible pressure sensor based on two-interlocked layers of Pt-coated nanofibers in PDMS substrate[19]. Shao et al fabricated a high-performance

Chapter: 4

pressure sensor that worked on PDMS micropillar structure and on conductive polypyrrole film, with sensitivity of 1.8 kPa^{-1} and detection limit as low as 2 Pa. The sensing materials in the afore mentioned section have been well researched but very costly. This sole reason prohibits any practical use in the future. So, we have to select the conductive material and microstructure in such a way that the sensor shows good repeatability and good sensitivity. In contrast to these relatively expensive materials, cost-effective solutions can be of future use. Some complicated, costly and time-consuming process have been used for fabrication process like traditional lithography, ion-etching and thermal treatment, those processes can hinder large scale production. In this work, we have chosen Bi_2Se_3 as a conductive material and for microstructure we have chosen tissue paper, which is a porous medium. Recently paper based electronic devices have drawn attention due to their ultra-low cost and mechanical flexibility. It has many application such as microfluidics device[21, 22], supercapacitor, nanogenerators[23] and on paper electronics[24]. Whitesides has done extensive study on paper-based electronics; he reported a paper based multiplexed transaminase test that can work as a rapid test and can separate aminotransferase and alanine aminotransferase [21]. Wang et al fabricated supercapacitors and nanogenerators using paper-based substrates; they fabricated a flexible supercapacitor based on polyaniline-Au-paper electrodes[25]. He also designed and fabricated a polytetrafluorethylene-Ag-paper based nanogenerator operating on electrostatic effect[23]. Cheng reported a wearable and highly sensitive pressure sensor fabricated using Au-Nw impregnated tissue paper, which was prepared using dip-coating Au-NWs into the tissue paper[14]. Zhan et al fabricated a pressure sensor based on single walled nanotube- paper through a simple dip-coating process[26]. Despite this literature reporting high sensitivity,

Chapter: 4

the cost of the conductive material was pretty high. Hence, we can see that a paper-based sensor is very much needed and has immense research value in wearable electronics. In our work, Bi_2Se_3 , a well-known topological insulator of new generation, has been chosen as the conductive material and since there has been no report of such kind, it is worth exploring. Bi_2Se_3 has unique conducting surface states at its edges[27], these surface states are protected by time-reversal symmetry, the spin-momentum being locked at the surface due to the strong spin-orbit coupling between Bi and Se[28]. The bands at the surface have Dirac-like dispersion, unequal topological invariance makes it robust, here any perturbation like any oxidation cannot disturb the robustness. Using Bi_2Se_3 , a wide range of applications have been explored till date such as photodetectors[29], resistive switching devices[30], low macroscopic field emitters for cold cathode applications[31], photocatalysis[32], Tetra-hertz frequency detection[33] etc. The main advantage of using Bi_2Se_3 is that liquid exfoliation is possible, and the synthesis can be done in simple solvothermal method. It has high yield, cost effectiveness and easy synthesis technique[30]. Specially Bi_2Se_3 is a heavily studied two-dimensional topological insulator, it has a conducting surface state and bulk bandgap of 0.3 eV. Bi_2Se_3 shows huge potential in electronic and optoelectronic applications.

In this thesis, piezo-resistive quality of a paper-based pressure sensor functionalized by Bi_2Se_3 is studied. For better sensing or improved sensitivity, moderation of the porous structure is done by stacking multiple layers of tissue paper functionalized by Bi_2Se_3 . The pressure sensing capability of this sensor has been explored for different pressure range and reported.

4.2 Experimental Technique

4.2.1 Solvothermal Synthesis and Liquid exfoliation of Bi_2Se_3 Nanoflakes

The Bi_2Se_3 nanostructures (NFs) were synthesized by solvothermal method. At first, a solid mixture of 1 mmol of bismuth nitrate pentahydrate $[\text{Bi}(\text{NO}_3)_3 \cdot 5\text{H}_2\text{O}]$ and 1.5 mmol of selenium (Se) powder (in a molar ratio of 2:3) was dissolved in 80 ml N,N-dimethylformamide (DMF). The same was placed in an ultrasonic bath for 30 min to obtain a uniform reaction mixture.

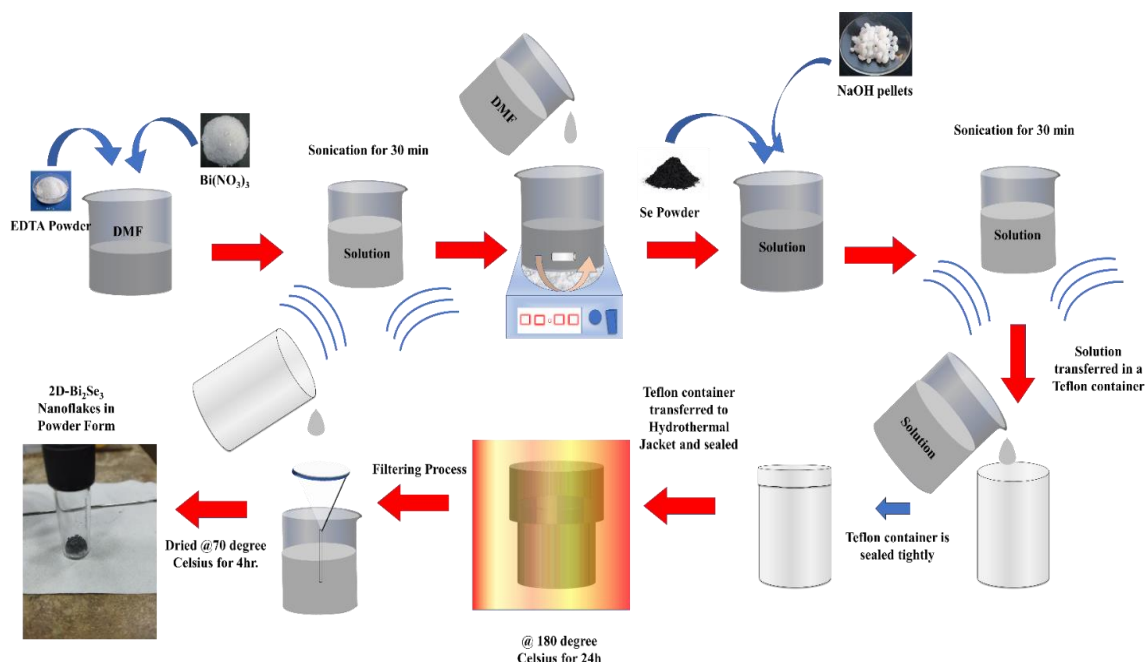


Fig.4.1 Solvothermal synthesis technique of Bi_2Se_3 Nanoflakes

Then, 4 mmol of sodium hydroxide (NaOH) as a reducing agent and 2 mmol of ethylenediaminetetraacetic acid (EDTA) as a size-directing additive were added. After sonication, the solution was transferred into a Teflon-lined stainless-steel autoclave, which was heated in the furnace at 180 °C for 24 h. After the reaction, the autoclave was allowed

Chapter: 4

to cool down to room temperature for a time period. The black precipitate produced from the reaction was filtered, rinsed with ethanol and de-ionized (DI) water for several times, then dried at 70°C in oven for 4h to obtain the resulting powder sample. The Bi_2Se_3 (NFs) were collected from dried Whatman paper using spatula. Figure 4.1 shows the schematic presentation of the solvothermal synthesis technique of Bi_2Se_3 nanoflakes.

4.2.2 Characterization of Bi_2Se_3 Nanoflakes

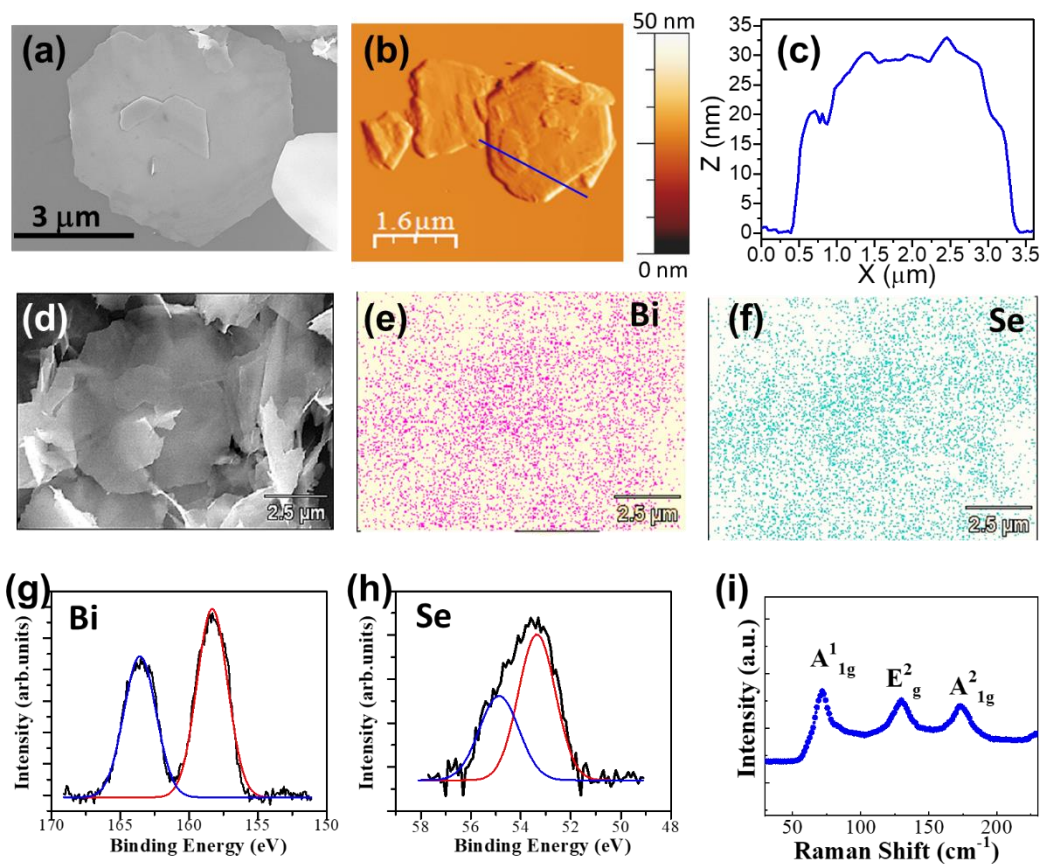


Fig. 4.2 Characterization of Bi_2Se_3 Nanoflakes. (a) SEM image of Bi_2Se_3 nanoflake (b) AFM image of a Bi_2Se_3 nanoflake. (c) height profile of the nanoflake. (d) SEM image of Bi_2Se_3 nanoflakes. EDS elemental mapping of (g) Bi 4f and (h) Se 3d binding energy spectrum of Bi_2Se_3 nanoflakes. (i) Raman Spectrum of Bi_2Se_3 NFs.

FESEM

Chapter: 4

Scanning electron microscopic (SEM, Hitachi, S-4800) image of the as-synthesized Bi_2Se_3 NFs is shown in Figure 4.2(a). We can observe that the prepared sample consists of hexagonal Bi_2Se_3 NFs, and the size of these NFs are about 2–5 μm .

AFM

AFM measurements were carried out in tapping mode configuration. The AFM image of a Bi_2Se_3 NF is shown in figure 4.2(b). The height profile is found to be in the range of 20-30nm with non-uniform surface height as shown in figure 4.2(c).

XPS

Chemical composition of Bi_2Se_3 NFs was investigated by X-ray photoelectron spectroscopy (XPS, Specs, Germany) analysis. Figures 4.2(g) and 4.2(h) show the core level spectra of chemically coordinated Bi and Se, respectively. Binding energies of Bi $4f_{7/2}$ and Bi $4f_{5/2}$ were found at 158.2 and 163.5 eV [Figure 4.2(g)], confirming that bismuth is in its Bi (III) state and the peak corresponding to Se 3d state is split into well-defined $3d_{5/2}$ and $3d_{3/2}$ peaks at 53.3 and 54.8 eV, respectively [Figure 4.2(h)].

Raman Spectroscopy

To further assess the Bi_2Se_3 NFs, we performed μ -Raman spectroscopy using a Witech Raman spectroscope. Figure 4.2(i) shows Raman spectrum of Bi_2Se_3 NFs under 532nm excitation wavelength. Three characteristic peaks at 71.6, 130.19 and 173.34 cm^{-1} are observed corresponding to A^1_{1g} , E^2_g , and A^2_{1g} modes, respectively, where A^1_{1g} and A^2_{1g} are associated with out-of-plane vibration of selenium atoms and E^2_g mode is related with in-plane vibrations of Bi and Se atoms which is similar to the previous reports by Zhang et al.[34]

EDS and Elemental Mapping

The stoichiometric and chemical compositional study was accomplished by energy-dispersive spectroscopy (EDS) with elemental mapping. The figures 4.2(e) and 4.2(f) shows the elemental mapping of the Bi_2Se_3 NFs. The analysis shows that the elements are uniformly distributed throughout the NFs.

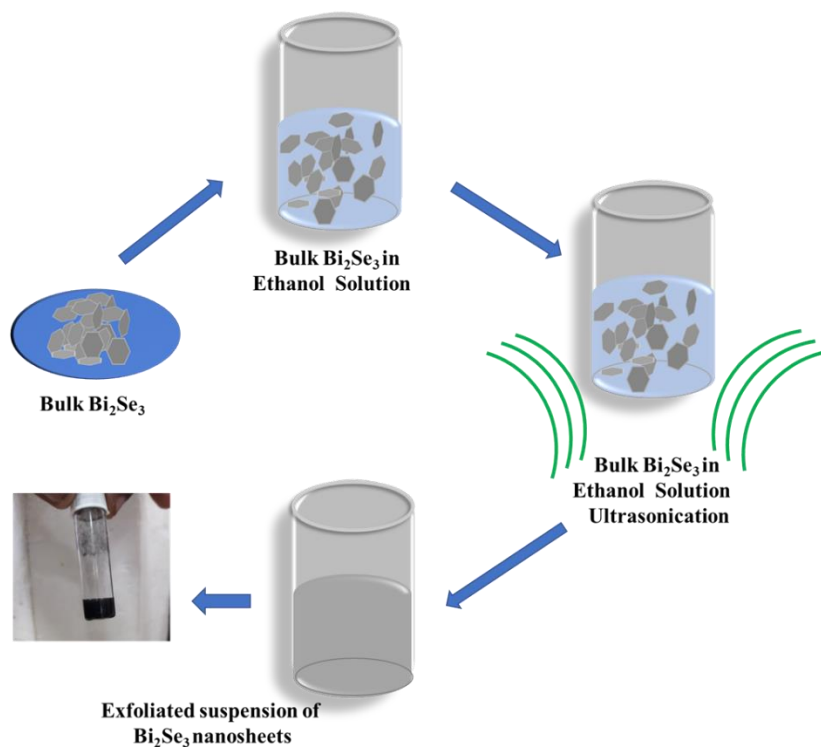


Fig.4.3 Schematic of synthesis of Bi_2Se_3 Nanosheets by liquid phase exfoliation technique.

4.2.3 Fabrication of Paper Based Pressure Sensor

The Bi_2Se_3 nanoflakes prepared using solvothermal technique is in powder form. To make the tissue paper functionalized by Bi_2Se_3 nanoflakes a solution is made by using 99.8% pure ethanol as the solvent. In the work, the solution concentration was varied with

Chapter: 4

different loadings of Bi_2Se_3 nanoflakes, i.e. 1mg/ml, 2mg/ml, 3mg/ml and 5mg/ml. This is done by adding Bi_2Se_3 nanoflakes in the solvent, and ultrasonicing it for 30 minutes. This solution-making procedure is shown in figure 4.3. Tissue papers were cut in the dimension 1cm X 1cm and placed in a clean petri dish. The tissue paper used were clean from any impurities. Fabrication process of the device is shown in the figure 4.4.

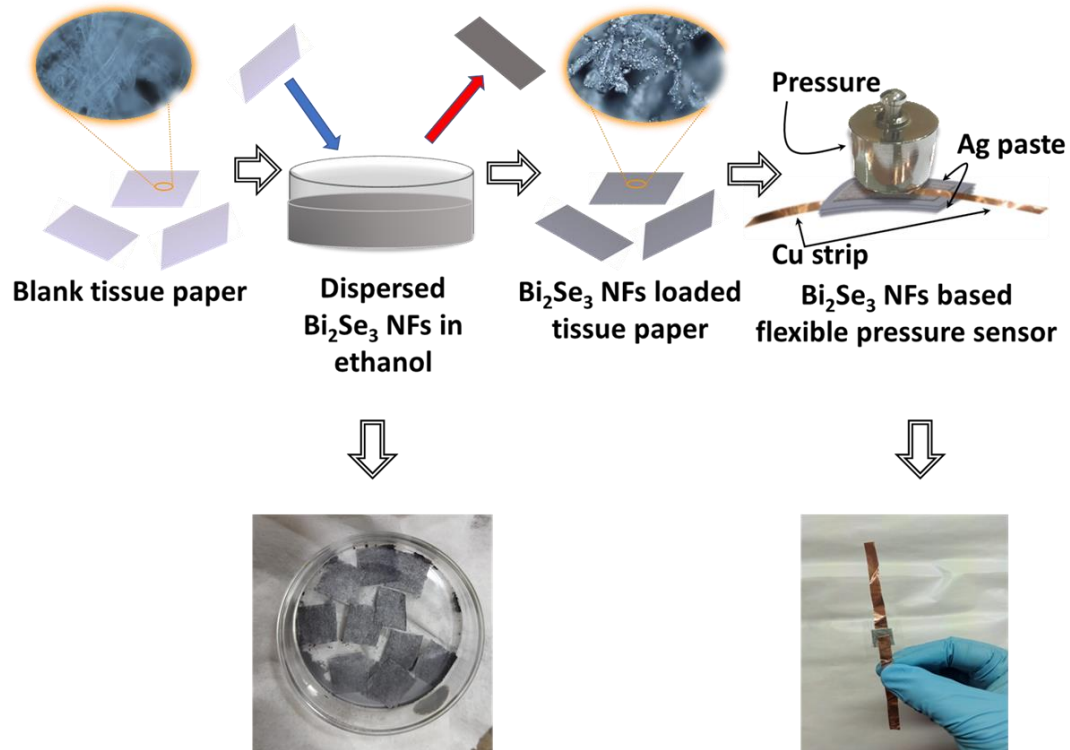


Fig. 4.4 Schematic diagram of the fabrication process of the Piezo-resistive pressure sensor functionalized by Bi_2Se_3 NFs.

Now this Bi_2Se_3 nanoflakes-ethanol solution is poured into the petri dish and the tissue papers were left to soak in the solution overnight. The ethanol evaporates from the solution, and we are left with Bi_2Se_3 nanoflakes coated tissue papers. The conductive element Bi_2Se_3 is necessary for the electrical conduction to happen. For electrical measurements, Ag paste was applied on the tissue paper in very little amount so that any kind of metal diffusion does not happen at high electric field or during the measurement. Later, the electrode-metal

Chapter: 4

variation was done to find out the best working electrode for measuring the sensitivity of the pressure sensor. Finally, the piezo-resistive sensor and electrode were encapsulated by two pieces of transparent scotch-tape on each side to protect the device from any kind of environmental damage and for easy measurements. This scotch-tape possesses good flexibility and is water-proof. Multiple layers provide mechanical strength to the sensor by making it robust. It is noteworthy that no complicated process such as lithography was employed during the fabrication process. As all the related components are flexible, the sensor may perform as good flexible device and can be attached to any surface regardless of its shape. Also, stacking of different numbers of layers (i.e. 1, 3 and 5 layers of tissue paper) is done to obtain the best performing device. Then, two copper wires-one on the top and another on the bottom of the stacked layers are connected using Ag-paste. And then the sensor is encapsulated by using a transparent scotch tape. After fabricating the device, a simple set of known and calibrated weights and Keysight B2902A Precision SMU unit was used to investigate the electrical performance of the pressure sensor under the influence of application of the weights. Figure 4.4 shows schematic illustration of fabricating Bi_2Se_3 based pressure sensor.

4.3 Results and Discussions

4.3.1 Pressure Sensing Mechanism and Electro-mechanical Performance of Bi_2Se_3 coated Tissue Paper

As all the components of the fabrication process is of ultra-low cost and the process itself is an easy one, the sensor can be effectively employed as a pressure sensor. Multiple numbers of Bi_2Se_3 coated tissue papers (1-layer, 3-layer and 5-layer devices) were stacked onto each other to form piezo-resistive sensor, and their sensitivity was recorded.

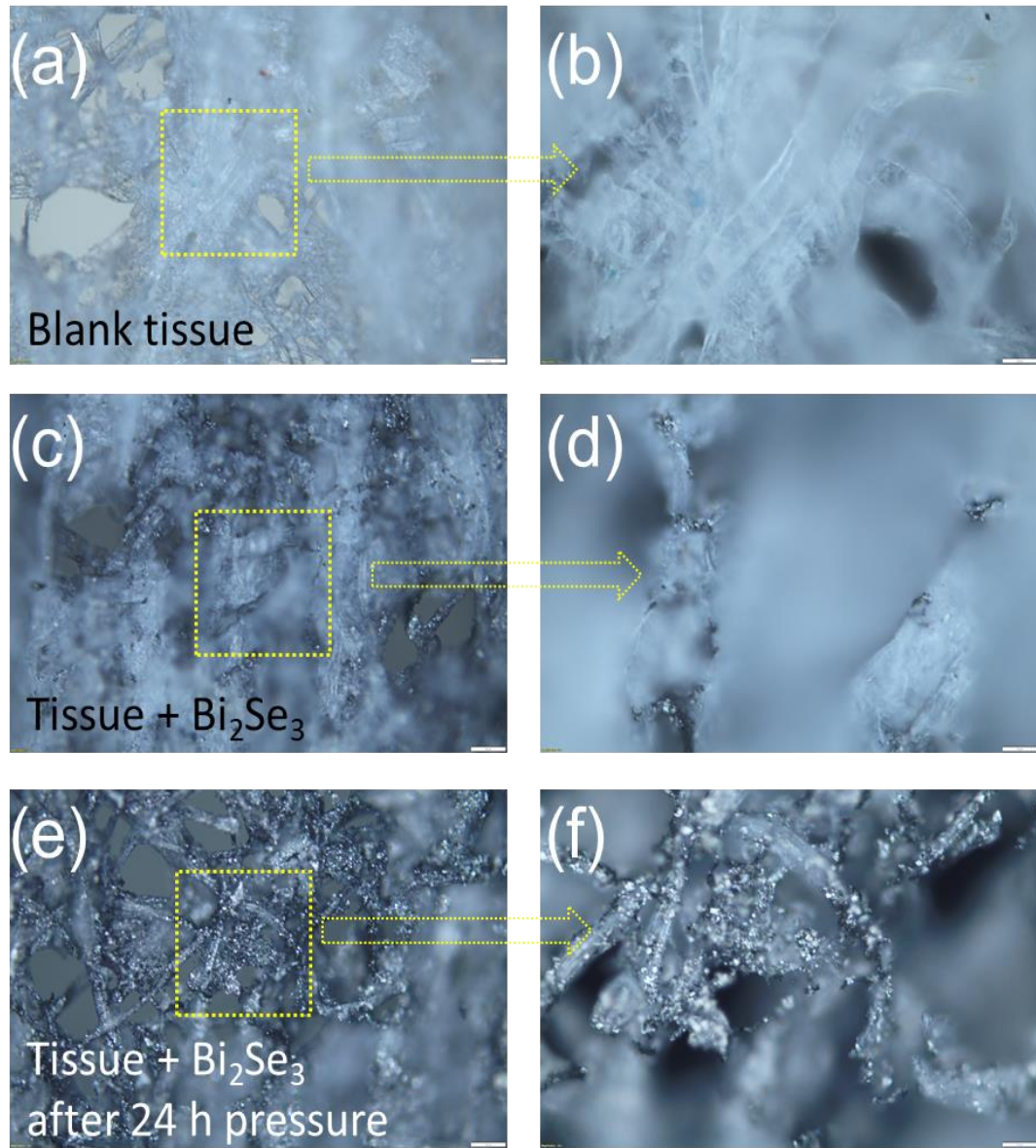


Fig.4.5 Optical microscope images of Bi₂Se₃ coated tissue paper (a)Blank tissue without any exposure to Bi₂Se₃ Nanoflakes, (b) corresponding optical image at high resolution, (c) Bi₂Se₃ Nanoflakes coated tissue paper without any compression, corresponding optical image is shown in (d), (e) image of the Bi₂Se₃ coated tissue paper exposed to 24h compression. Image (f) corresponds to optical image of the Bi₂Se₃ coated tissue paper under 24hr compression.

The number of layers is varied to get the best operating device, the more the layers are added to the sensor the more is the resistance change, because more deformity takes place. But, in this work, according to the choice of our microstructure and conductive material the maximum number of layers that can be employed in the device turns out to be three.

Chapter: 4

This claim is established by taking electrical measurements by using well calibrated weights bought from market.

In figure 4.5(a) Optical microscope image of a blank tissue paper was taken. And it was compared with other Bi_2Se_3 NFs coated tissue papers under no pressure and exposing to 24 hr. of continuous pressure. It can be seen that 24 h sample has denser network of NF coated tissue fibers.

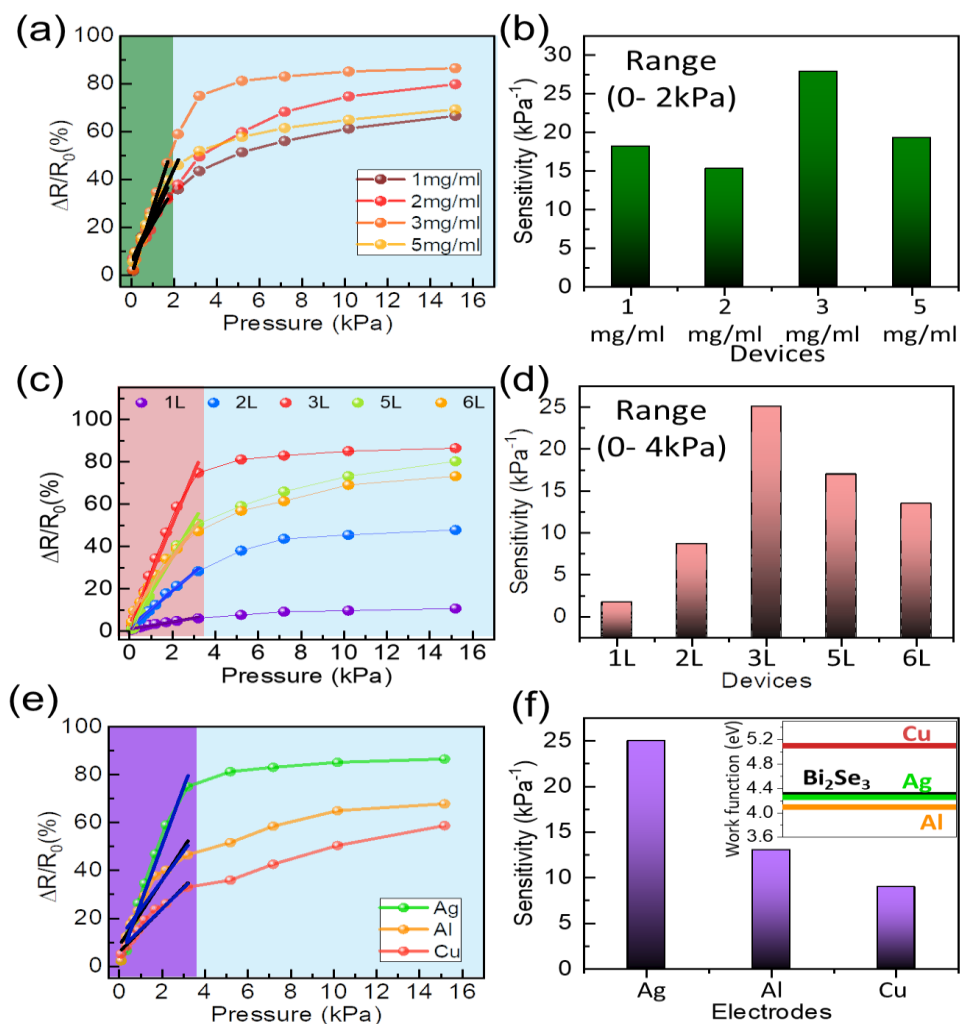


Fig.4.6(a) Variation in sensitivity due to varying concentration of solution. (b) static responses in terms of sensitivity due to layer variation. (c) sensitivity variation for different no. of stacked layers with pressure. (d) height bar showing sensitivity value due to layer variation in 0-4 kPa range. (e) sensitivity variation due to variation in electrode material. (f) height bar showing sensitivity value due to electrode variation in 0-4 kPa range

Chapter: 4

The figure 4.6(b) shows the relative resistance change in the pressure sensor due to static compression, this relative resistance change is denoted as $\Delta R/R_0 = (R - R_0)/R_0$, here R_0 and R refers to the resistance values of one, two, three and five layer of pressure sensor before and after compression, respectively. Further study for 1, 2 and 5 mg/ml concentration devices showed the sensitivity values of 18.2, 15.3 and 19.3 kPa^{-1} (shown in figure 4.6(a)) respectively. The difference in sensitivity due to concentration variation is shown in figure 4.6(b). It can be easily understood that three-layer device will show reduced stiffness than four-layer device. With optimum number of layers and concentration best performing device is found that showed highest sensitivity in 0-2 kPa region. As, the number of layers is increased, the sensitivity increases up to three-layer device, then decreases. The sensitivity of the highest performing pressure sensor consisting of three layers is calculated to be 25.1 kPa^{-1} in the range of 0-2 kPa. The calculated sensitivity for one layer, two layer, five-layer device and six-layer device is calculated to be 1.73, 8.67, 17 kPa^{-1} and 13.5 kPa^{-1} respectively (shown in figure 4.7(d)). From the above calculated values of sensitivity of the pressure sensor, it was found that three-layer device performs best. Also, the concentration variation is done to investigate best concentration of the functionalizing material for the tissue papers to soak in. Through experiment it was found that for the concentration of 3mg/ml the three-layered device showed highest sensitivity of 27.9 kPa^{-1} . Electrode-metal variation is done to investigate the best performing device and it was found that the device incorporating Ag paste showed higher sensitivity (25 kPa^{-1}) compared to other devices. For aluminum electrode and copper electrode the calculated sensitivities were 13 kPa^{-1} and 9 kPa^{-1} respectively as shown in figure 4.6(f). To determine different amount of pressure responses, time dependent measurement was done and shown in figure

Chapter: 4

4.7(a), the pressure was varied from 0.5 kPa to 7.0 kPa and the corresponding responses were recorded. For next measurement, 0.5 kPa, 1 kPa, 2 kPa and 3 kPa pressure was applied sequentially, each load undergoing three individual loading and unloading cycles, and the response shown in figure 4.7(b). The recorded response was steady and repeatable.

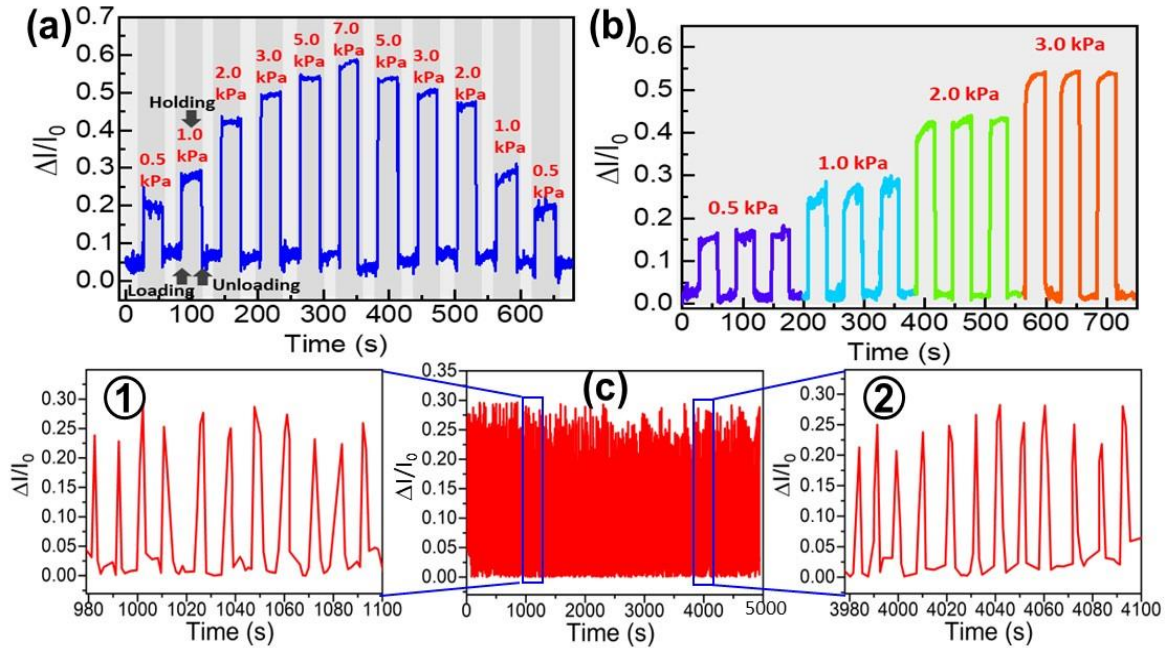


Fig.4.7(a) Response of the sensor due to different pressure values from .5 kPa to 7.0 kPa.(b) sequential loading of different pressure values ranging from 0.5 kPa-3.0 kPa.(c) relative change in sensitivity under cyclic loading and de-loading. (c)①showing initial period of the fatigue test and (c)②shows the end period.

Fig 4.7(c) shows sensitivity variation under fatigue test in more than 5000 cycles, after which the sensor showed same sensitivity under compression. Figure 4.7(c)① and ② shows the sensitivity variation of the device during the 1000s and 4000s of the fatigue test. The sensor showed the same sensitivity over the test which suggest it is very high-performance device. To explain the working mechanism of the pressure sensor, the

Chapter: 4

schematic illustration of a three-layer device is shown under no-pressure condition and under compression (figure 4.8). When no compression was applied, there were too many air-gaps and very few contact points between the three layers of Bi_2Se_3 coated tissue papers. Hence a large resistance exists in this state. When a small pressure is applied on the sensor, the amount of air space between the layers decreases, also the number of contact points with the electrode increases, as shown in figure 4.8(b). This leads to a sharp decline in resistance value and the sensor shows high sensitivity due to afore-mentioned process. As the pressure increases more, the internal microstructure gets more compressed, the tissue fibers form denser network and elastically deforms, and in turn increases the number of contact points. This process is shown in figure 4.8(a).

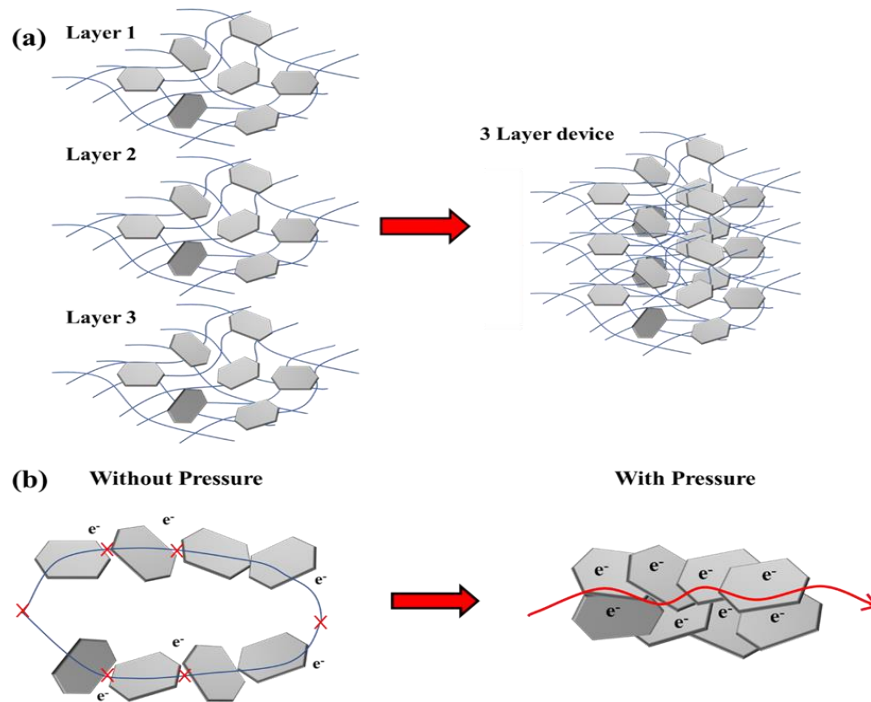


Fig.4.8 (a), (b)The schematic of pressure dependent static performance of a Bi_2Se_3 Nanoflakes coated tissue paper.

4.3.2 Application of Bi_2Se_3 functionalized Tissue Paper based Pressure Sensor

Chapter: 4

Due to excellent sensitivity, repeatability and broad pressure range the pressure sensor can be used in multiple applications such as detecting finger tapping, finger bending, air blowing from mouth, vibration monitoring system etc. The sensor can detect air flow blown from mouth as shown in figure 4.9(e), the response data is shown in figure 4.9(f). The sensor is also capable of detecting the pressure caused by Hg drops placed upon the sensor (figure 4.9(a)), as the number of drops increase the sensitivity increases indicating the minor pressure change caused by the increasing number of drops. This Hg drops were placed carefully and the data shows extreme responsiveness of the pressure sensor in low pressure regime.

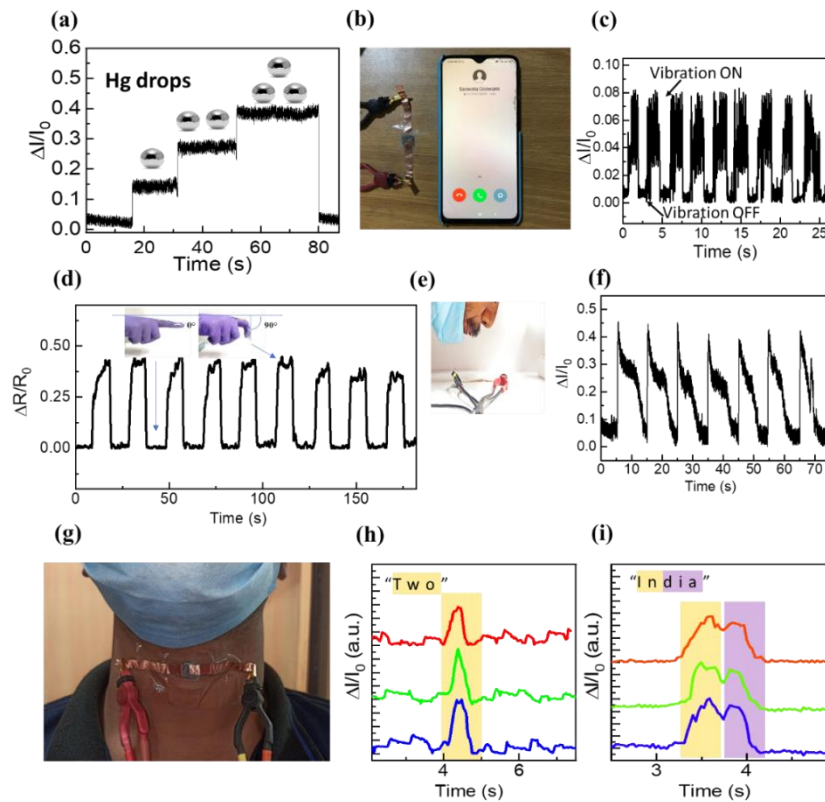


Fig. 4.9. Application of flexible pressure sensor for various real-time physiological signal monitoring. (a) time resolved response of pressure sensor for small pressure of Hg drops. (b) digital photograph of the sensor adjacent to vibrating cell-phone. (c) resistive response of the sensor generated from vibration. (d) change in sensitivity due to bending of the sensor mounted on the finger under two different angles 0° and 90° . (e) photograph showing the sensor blown by mouth. (f) the corresponding sensitivity variation caused by previous action. (g) digital photograph showing sensor pasted on human throat for voice recognition application. (h) and (i) real time response data caused by phonation of words 'two' and 'India' respectively.

The sensor showed response on high-frequency vibration caused by a mobile phone in figure 4.9(b)., the response data is shown in the fig. 4.9(c). From the response data the vibrating mode and the non-vibrating mode of the phone can be distinguished. The device shows excellent response on subtle pressure, it can also detect large amount of pressure caused by finger movement. The sensor mounted onto the top of the finger, is able to detect the deformation caused by the

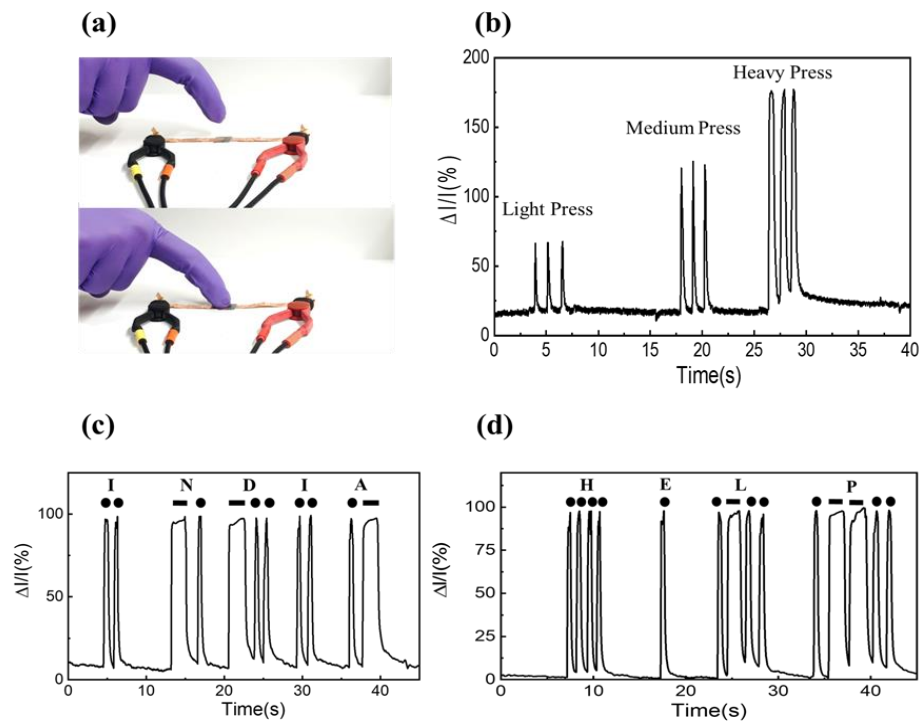


Fig.4.10(a) digital photograph of the sensor showing response for finger tapping. (b) change in sensitivity due to pressing, three different pressing pressure is identified. (c)(d) two different morse code generated by tapping on the sensor.

bending (figure 4.9d). The finger is bent at an angle 90 degree for repeated times and the response was recorded as shown in figure 4.9(e). This response shows promising application in athletic science for monitoring athlete's performance. Figure 4.9(g) shows

Chapter: 4

the flexible pressure sensor being attached to throat, below the vocal cord, to record the muscle motion. This effectively detects the vocal muscle motion when the person speaks. The sensor is able detect the words like 'two', 'India' etc. and their response is shown in figure 4.9(h) and figure 4.9(i).

The sensor shows response on gentle pressing onto the sensor as shown in figure 4.10(b). The figure 4.10(a) shows the digital photograph of the finger tapping experiment. The sensor can distinguish between heavy press, medium press and light press as shown in figure 4.10(b), hence it can be applied in various IOT (Internet of Things) applications. One such interesting application is Morse Code generator. Two different words 'INDIA' and 'HELP' are generated using the morse code method, illustrated in figure 4.10(c) and 4.10(d). This type of application can realize real time IOT device which can be used for biological activity monitoring. This pressure sensor is made using cost-efficient method without involving any lithography procedure. Here a flexible array of electronic skin matrix is made to determine spatial distribution and magnitude of applied pressure. This mentioned attributes are critical in the application of wearable electronics and in human-machine interfacing.

Figure 4.11(a) shows the pixelated 3X3 cross-bar array, each pressure unit has one top electrode and one bottom electrode and their combination is unique to the particular unit. This strategy can be used to individually select each sensing unit. The e-skin matrix is able to distinguish between heavy loading and light loading, the digital photograph of the

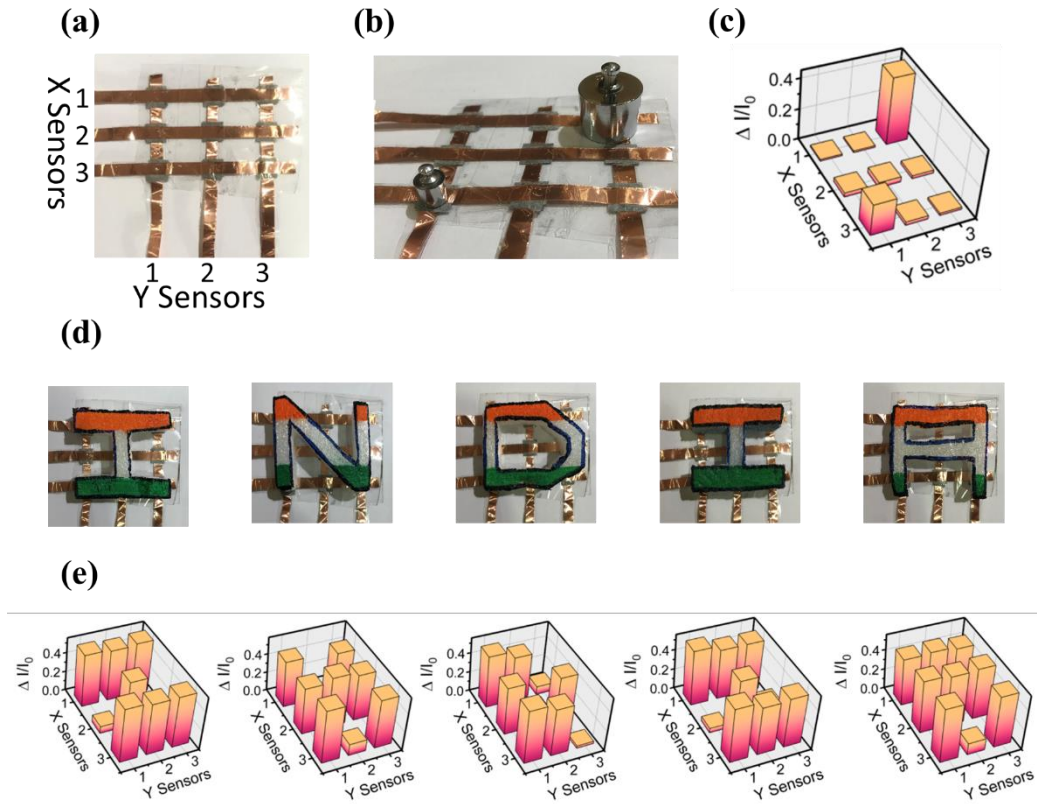


Fig.4.11 (a) 3X3 array of matrix that resembles e-skin type behavior. (b) 3X3 array of matrix loaded with two different weights. (c) response due to previous loading and heigh difference shows difference in sensitivity. (d)top view of the alphabetical structures positioned over the e-skin. (e)corresponding response mapping of the pressure distribution.

experiment is shown in the figure 4.11(b). 100g and 10g weights were loaded on different pixels to generate real time sensitivity variation caused by the different weights. The fabrication method of the matrix sensor is same as that of general pressure sensor, only the copper electrodes were arranged in a matrix manner. Between every top and bottom electrodes, a three-layer stacked Bi_2Se_3 coated tissue paper is placed. Sponges were cut in alphabetical shapes to generate response from matrix array, the shapes were positioned over the array skin and pressure was applied upon them. The response we got from the skin for the word 'INDIA', the corresponding resistive response generated from each letter is shown in form of 3D bars in figure 11(e).

4.4 Conclusion

In short, in this work a cost-efficient, easy-to-fabricate piezo-resistive pressure sensor has been fabricated that shows high sensitivity and flexibility. The sensing material is based on Bi_2Se_3 nanoflakes, and the microstructure is low-cost tissue paper. The tissue papers were soaked in Bi_2Se_3 nanoflakes (synthesized using simple solvothermal method) solution followed by simple stacking of multiple layers to form the pressure sensor; a top electrode and a bottom electrode were added with the help of Ag paste for measurement purpose. The simple fabricated pressure sensor showed excellent response due to unique structure and compressive electrical contact. The sensitivity of the piezo-resistive pressure sensor is reported to be 25.1 kPa^{-1} (in the range 0-2 kPa). The sensor is capable of detecting mobile vibration, weak air flow from mouth, voice recognition, bending, differentiating between different amounts of pressures etc. All these characteristics are attributed to the high sensitivity of the pressure sensor. Also, the optimized sensor is used to fabricate an array of matrix resembling electronic-skin. This previously mentioned e-skin array can be used to detect spatial pressure distribution and pressure magnitude. It is believed that such low-cost, easy-to-fabricate pressure sensor can open up new opportunities and applications in e-skin and smart wearable electronics.

4.5 References

1. Chung, H.U., et al., *Binodal, wireless epidermal electronic systems with in-sensor analytics for neonatal intensive care*. 2019. **363**(6430): p. eaau0780.
2. Boutry, C.M., et al., *Biodegradable and flexible arterial-pulse sensor for the wireless monitoring of blood flow*. 2019. **3**(1): p. 47-57.
3. He, F., et al., *Recent progress in flexible microstructural pressure sensors toward human-machine interaction and healthcare applications*. 2021. **5**(3): p. 2001041.
4. Zhong, M., et al., *Wide linear range and highly sensitive flexible pressure sensor based on multistage sensing process for health monitoring and human-machine interfaces*. 2021. **412**: p. 128649.

Chapter: 4

5. Chen, T., et al., *Highly sensitive and wide-detection range pressure sensor constructed on a hierarchical-structured conductive fabric as a human-machine interface*. 2020. **12**(41): p. 21271-21279.
6. Tabor, J., et al., *Textile-based pressure sensors for monitoring prosthetic-socket interfaces*. 2021. **21**(7): p. 9413-9422.
7. Ha, K.H., et al., *Highly sensitive capacitive pressure sensors over a wide pressure range enabled by the hybrid responses of a highly porous nanocomposite*. 2021. **33**(48): p. 2103320.
8. Fiorillo, A., et al., *Theory, technology and applications of piezoresistive sensors: A review*. 2018. **281**: p. 156-175.
9. Tressler, J.F., S. Alkoy, and R.E.J.J.o.e. Newnham, *Piezoelectric sensors and sensor materials*. 1998. **2**(4): p. 257-272.
10. Lei, H., et al., *Advances in self-powered triboelectric pressure sensors*. 2021.
11. Ma, Y. and L.J.S.M. Zhi, *Graphene-based transparent conductive films: material systems, preparation and applications*. 2019. **3**(1): p. 1800199.
12. Zhu, B., et al., *Microstructured graphene arrays for highly sensitive flexible tactile sensors*. 2014. **10**(18): p. 3625-3631.
13. Jian, M., et al., *Flexible and highly sensitive pressure sensors based on bionic hierarchical structures*. 2017. **27**(9): p. 1606066.
14. Gong, S., et al., *A wearable and highly sensitive pressure sensor with ultrathin gold nanowires*. 2014. **5**(1): p. 1-8.
15. Kim, H.-J., et al., *Highly sensitive and very stretchable strain sensor based on a rubbery semiconductor*. 2018. **10**(5): p. 5000-5006.
16. Choong, C.L., et al., *Highly stretchable resistive pressure sensors using a conductive elastomeric composite on a micropylamid array*. 2014. **26**(21): p. 3451-3458.
17. Park, H., et al., *Stretchable array of highly sensitive pressure sensors consisting of polyaniline nanofibers and Au-coated polydimethylsiloxane micropillars*. 2015. **9**(10): p. 9974-9985.
18. Lee, Y., et al., *Flexible ferroelectric sensors with ultrahigh pressure sensitivity and linear response over exceptionally broad pressure range*. 2018. **12**(4): p. 4045-4054.
19. Pang, C., et al., *A flexible and highly sensitive strain-gauge sensor using reversible interlocking of nanofibres*. 2012. **11**(9): p. 795-801.
20. Yao, H.B., et al., *A flexible and highly pressure-sensitive graphene-polyurethane sponge based on fractured microstructure design*. 2013. **25**(46): p. 6692-6698.
21. Pollock, N.R., et al., *A paper-based multiplexed transaminase test for low-cost, point-of-care liver function testing*. 2012. **4**(152): p. 152ra129-152ra129.
22. Cate, D.M., et al., *Recent developments in paper-based microfluidic devices*. 2015. **87**(1): p. 19-41.
23. Zhong, Q., et al., *A paper-based nanogenerator as a power source and active sensor*. 2013. **6**(6): p. 1779-1784.
24. Russo, A., et al., *Pen-on-paper flexible electronics*. 2011. **23**(30): p. 3426-3430.
25. Yuan, L., et al., *Paper-based supercapacitors for self-powered nanosystems*. 2012. **51**(20): p. 4934-4938.
26. Zhan, Z., et al., *Paper/carbon nanotube-based wearable pressure sensor for physiological signal acquisition and soft robotic skin*. 2017. **9**(43): p. 37921-37928.
27. Hasan, M.Z. and C.L.J.R.o.m.p. Kane, *Colloquium: topological insulators*. 2010. **82**(4): p. 3045.
28. Jiang, Y., et al., *Vertical/planar growth and surface orientation of Bi₂Te₃ and Bi₂Se₃ topological insulator nanoplates*. 2015. **15**(5): p. 3147-3152.
29. Das, B., et al., *Topological insulator Bi₂Se₃/Si-nanowire-based p-n junction diode for high-performance near-infrared photodetector*. 2017. **9**(27): p. 22788-22798.

Chapter: 4

30. Das, B., et al., *Flexible, transparent resistive switching device based on topological insulator Bi₂Se₃-organic composite*. 2018. **124**(12): p. 124503.
31. Das, B., et al., *rGO-Wrapped flowerlike Bi₂Se₃ nanocomposite: synthesis, experimental and simulation-based investigation on cold cathode applications*. 2016. **6**(31): p. 25900-25912.
32. Razzaque, S., et al., *Selective synthesis of bismuth or bismuth selenide nanosheets from a metal organic precursor: investigation of their catalytic performance for water splitting*. 2021. **60**(3): p. 1449-1461.
33. Viti, L., et al., *Plasma-wave terahertz detection mediated by topological insulators surface states*. 2016. **16**(1): p. 80-87.
34. Zhang, J., et al., *Raman spectroscopy of few-quintuple layer topological insulator Bi₂Se₃ nanoplatelets*. 2011. **11**(6): p. 2407-2414.

Chapter 5

Kerr Non-Linearity in 2D Bi₂Se₃ for all Optical Switching and Photonic Logic Gate Application

Recently optical responses of two-dimensional(2D) materials have drawn much attention due to their strong nonlinear characteristics and Kerr nonlinearity. The various optoelectronic device applications like photonic diode and logic application have emerged as hot topic of discussion. In this work we have discussed the strong optical non-linear responses of 2D Bi_2Se_3 nanosheets through Spatial self- phase modulation method (SSPM). This SSPM phenomenon is caused by non-local coherent light-matter interaction. The layered Bi_2Se_3 is made by solvothermal method. The coherent interaction of light and Bi_2Se_3 nanoflakes suspended in the solution, forms concentric circles of diffraction rings, this is formation of the diffraction ring described by the wind chime model. Third order nonlinear optical coefficients are determined from the self-diffraction patterns caused varying intensity of different wavelengths. By taking advantage of reverse saturated absorption of 2D SnS_2 nanosheets compared to Bi_2Se_3 NFs, an all-optical diode has been investigated with Bi_2Se_3 - SnS_2 heterostructure by the method of non-reciprocal light propagation.

5.1 Introduction

Strong light-matter interactions in 2D materials produces many non-linear optical phenomenon that can have far reaching effect in science and technology. 2D materials have drawn significant attention for their optoelectronic properties and non-linear optical characteristics[1].

The non-linear optical properties of a material are determined by following three methods namely,

1. Four Wave mixing [2]
2. Z-Scan method [3]
3. Spatial -Self Phase Modulation(SSPM) [4]

Among the methods discussed above Four Wave mixing and Z-Scan methods are complicated methods, which require expensive set up and complicated result analysis. In contrast to aforementioned techniques SSPM method is quite easy and requires less rigorous experimental analysis. Hence the SSPM Spectroscopy has become quite well-known technique to determine non-linear optical parameters of the materials, like non-linear refractive index and third-order non-linear susceptibility $\chi^{(3)}$ [5]. In this technique strong light matter interaction creates spatial phase modulation of the incident laser beam creates and produces diffraction ring pattern in the far-field. In 2011 Wu et al. investigated non-linear susceptibility $\chi^{(3)}$ of graphene nanoflakes using SSPM method[6]. After that there has been increased interest SSPM method and many group studied non-linear optical properties of different materials using SSPM technique. The non-linear interaction leads to self-diffraction rings and patterns in the far field due to SSPM method. The formation, expansion and collapse process of the diffraction rings with time are understood and described by the non-local coherent theory[7]. This model has been named as ‘Wind Chime Model’. According to this model the layered nanostructures gets reoriented due to the polarization caused by incoming coherent light beam. The electric-field in the light beam causes the samples to be polarized; this causes the diffraction pattern[8]. Based on energy relaxation process the nanoflakes are reoriented in the direction of electric-field of

incoming light. The transition metal di-chalcogenides are attractive candidate due to their tunable band structure and interesting optoelectronic property. TMDs materials are composed of transition metal intercalated between chalcogen elements in the layered structures[9]. This layers are held together by weak Van der Waals force. The 2D Bi_2Se_3 is explored for various applications like photodetector[10], resistive switching device[11], low macroscopic field emitters for cold cathode application[12], photocatalysis[13], terahertz frequency detection[14].

So far SSPM method has been used to determine the third order non-linear susceptibility and non-linear refractive index of the material. But recently optical device-based applications are being done. Although very few groups have investigated logic-based application and diode application[15, 16].

In this work we have discussed the non-linear optical properties of the material Bi_2Se_3 nanoflakes using SSPM method. In this work the potential applications such as novel photonic diode and logic application is also explored.

5.2 Experimental Technique

5.2.1 Solvothermal Synthesis and Liquid exfoliation of Bi_2Se_3 Nanoflakes

The Bi_2Se_3 nanostructures (NFs) were synthesized by solvothermal method. At first, a solid mixture of 1 mmol of bismuth nitrate pentahydrate $[\text{Bi}(\text{NO}_3)_3 \cdot 5\text{H}_2\text{O}]$ and 1.5 mmol of selenium (Se) powder (in a molar ratio of 2:3) was dissolved in 80 ml N,N-dimethylformamide (DMF). The same was placed in an ultrasonic bath for 30 min to obtain a uniform reaction mixture.

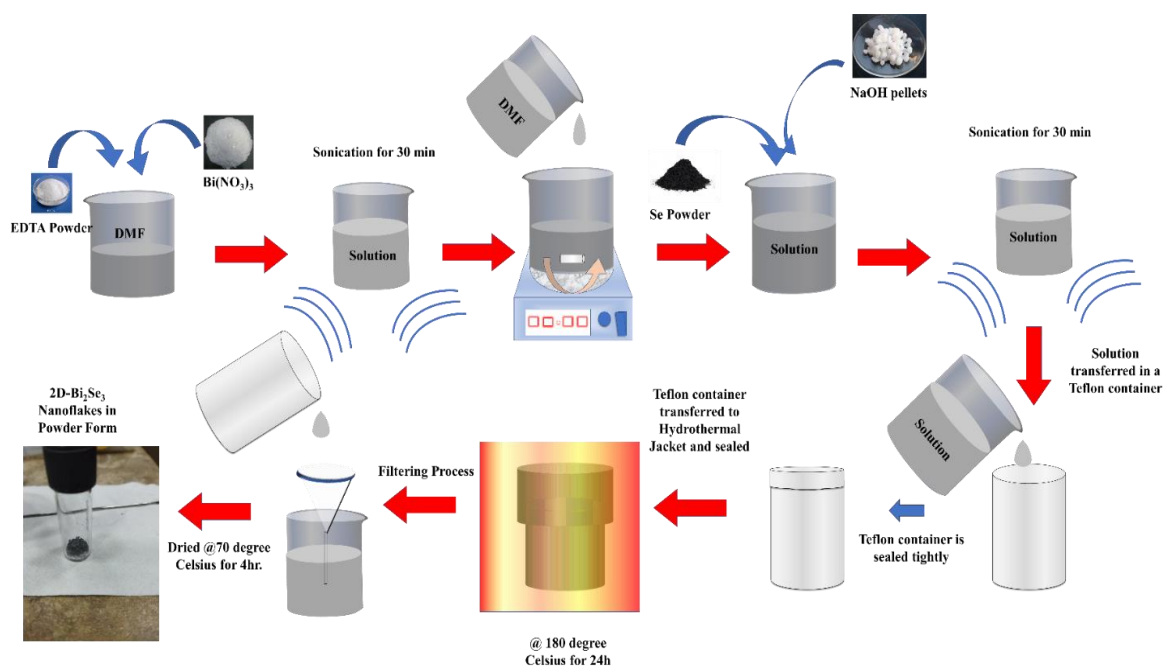


Fig.5.1 Solvothermal synthesis technique of Bi_2Se_3 Nanoflakes

Then, 4 mmol of sodium hydroxide (NaOH) as a reducing agent and 2 mmol of ethylenediaminetetraacetic acid (EDTA) as a size-directing additive were added. After sonication, the solution was transferred into the Teflon-lined stainless autoclave, which was heated in the furnace at 180 °C for 24 h. After the reaction, the autoclave was allowed to cool down to room temperature for a time period. The black precipitate produced from the reaction was filtered, rinsed with ethanol and de-ionized (DI) water for several times, and dried at 70 °C in vacuum for 4 h. to obtain the resulting powder sample. The Bi_2Se_3 NFs were collected from dried Whatman paper using spatula. Figure 4.1 shows the solvothermal synthesis technique of Bi_2Se_3 nanoflakes using solvothermal technique.

5.2.2 Characterization of Bi_2Se_3 Nanoflakes

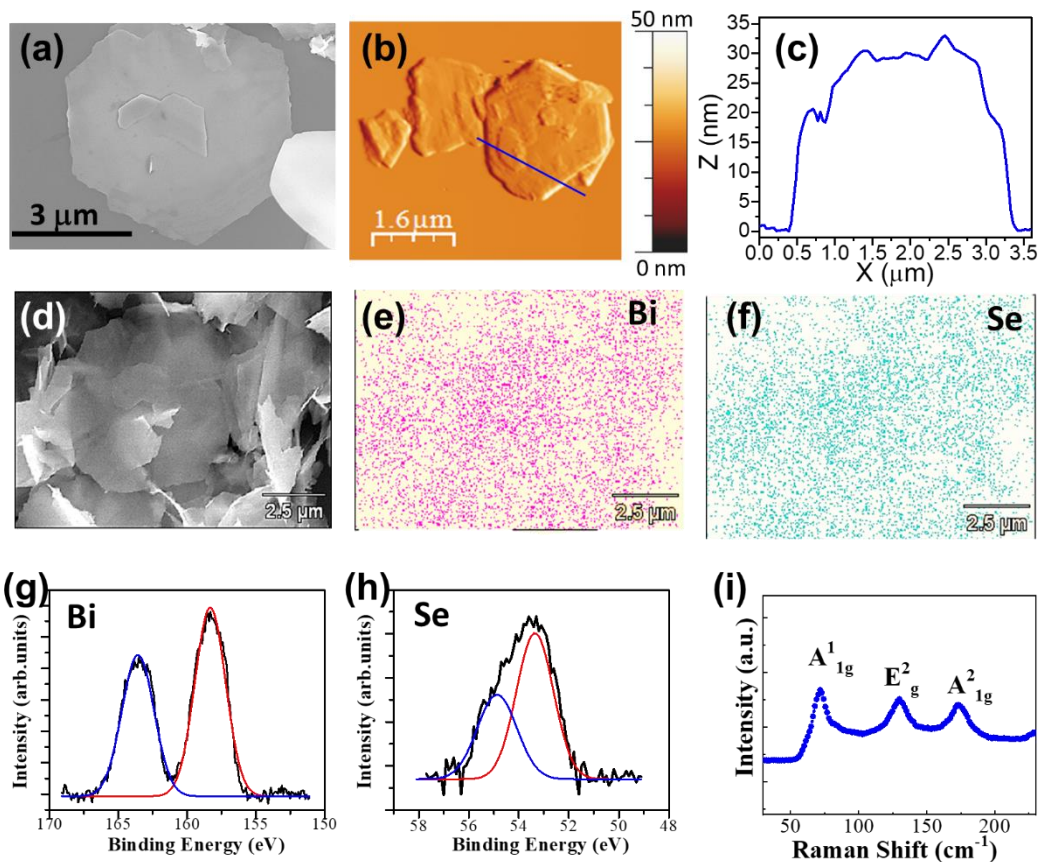


Fig. 5.2 Characterization of Bi_2Se_3 Nanoflakes. (a) SEM image of Bi_2Se_3 nanoflake (b) AFM image of a Bi_2Se_3 nanoflake. (c) height profile of the nanoflake. (d) SEM image of Bi_2Se_3 nanoflakes. EDS elemental mapping of (g) Bi 4f and (h) Se 3d binding energy spectrum of Bi_2Se_3 nanoflakes. (i) Raman Spectrum of Bi_2Se_3 NFs.

FESEM

Scanning electron microscopic (SEM, Hitachi, S-4800) image of as-synthesized Bi_2Se_3 NFs is shown in Fig. 4.2(a). We can observe that the prepared sample consists of hexagonal Bi_2Se_3 NFs, and the sizes of these NSs are about 2–5 μm .

AFM

AFM measurements were carried out in tapping mode configuration. The height profile of the nanoflakes found to be in range of 20-30 nm with non-uniform surface height shown in fig.4.2(c).

XPS

Chemical composition of Bi_2Se_3 NFs was investigated by X-ray photoelectron spectroscopy (XPS, Specs, Germany) analysis. Figure 4.2(g) and 4.2(h) show the core level spectra of chemically coordinated Bi and Se. Binding energies of Bi $4f_{7/2}$ and Bi $4f_{5/2}$ were found at 158.2 and 163.5 eV [Fig. 4.2(g)], confirming that bismuth is in its Bi (III) state and the peak corresponding to Se 3d state is split into well-defined $3d_{5/2}$ and $3d_{3/2}$ peaks at 53.3 and 54.8 eV, respectively [Fig. 4.2(h)].

Raman Spectroscopy

To further assess the Bi_2Se_3 NFs, we performed μ -Raman spectroscopy using a Witech Raman microscope. Figure 4.2(i) shows Raman spectrum of Bi_2Se_3 NSs under 532nm excitation wavelength. Three characteristic peaks at 71.6, 130.19, and 173.34 cm^{-1} are observed corresponding to A^1_{1g} , E^2_g , and A^2_{1g} modes, respectively, where A^1_{1g} and A^2_{1g} are associated with out-of-plane vibration of selenium atoms and E^2_g mode is related with in-plane vibration of Bi and Se atoms which is similar to the previous reports by Zhang et al.[17]

EDS and Elemental Mapping

The stoichiometric and chemical compositional study was accomplished by EDS with elemental mapping. The figures 4.2(e) and 4.2(f) shows the elemental mapping of Nanoflakes. The analysis shows that the elements are uniformly distributed.

5.3 Results and Discussion

5.3.1 Non-Linear Kerr Effect

Non-linear Kerr effect is important to study non-linear optical properties of the 2D material. According to these effects non-linear Kerr effect can be written in the form of below,

Equation describing light intensity and non-linear refractive index are,

$$n = n_0 + n_2 I \dots \dots \dots (5.1)$$

here n is the refractive index, n_0 is the linear refractive index, n_2 is the non-linear refractive index and I is the Intensity of laser light.

Because of the strong non-linear Kerr effect, a phase shift is introduced. The phase has a nonlinear modulating behavior to the transverse intensity profile of the incident gaussian laser beam. A phase shift is introduced which is expressed as,

$$\Delta\psi(r) = \frac{2\pi n_0}{\lambda} \int_0^{L_{eff}} n_2 I(r,z) dz \dots \dots \dots (5.2)$$

I is the light intensity, $\Delta\psi$ is the phase shift of the laser beam, r is the radial coordinate, λ is the wavelength, L is the total effective propagation length through the sample containing cuvette, $I(r,z)$ is the intensity of the distribution. N is the total no rings formed due to diffraction. The ‘self’ phase shift ($\Delta\psi$) that gets modulated due to the nonlinear Kerr Effect is result of the change in optical refractive index, n as function of intensity of the coherent

Gaussian laser beam. Therefore, the propagating light creates diffraction pattern of bright and dark rings. The formation of the diffraction pattern is shown in fig.5.3(a).

And the equation corresponding to the bright and dark rings is,

$$\Delta\psi(r_1) - \Delta\psi(r_2) = 2M\pi \dots\dots\dots (5.3)$$

Here M is the integer and it is even or odd corresponding to the bright or dark ring. Here

L_{eff} can be calculated using the equation below,

$$L_{eff} = \int_{L_1}^{L_2} \left(1 + \frac{Z^2}{Z_0^2}\right)^{-1} dZ = Z_0 \tan^{-1} \left[\frac{Z}{Z_0} \right]_{L_1}^{L_2} ; Z_0 = \frac{\pi\omega_0^2}{\lambda} \dots\dots\dots (5.4)$$

Here L_1 and L_2 are the distance from the focus(f) to each side of the quartz cuvette. The central intensity profile of the transmitted gaussian beam can be expressed as

$I(0,z)=2I$, where I be the average intensity of the incident laser, z_0 is the diffraction length and w_0 is the $1/e^2$ beam radius.

From the equation (5.2) and (5.4) we can conclude that the nonlinear refractive index(n_2) to be,

$$n_2 = \frac{\lambda}{2n_0 L_{eff}} \frac{dN}{dI} \dots\dots\dots (5.5)$$

Also, we can calculate $\chi^{(3)}(t)$ from the derivation as described in [18],

$$\chi^3 = \frac{n_0^2 c}{12\pi^2} n_2 \dots\dots\dots (5.6)$$

Available number of 2D nanoflakes in the solution greatly influence the value of $\chi^{(3)}$. So, it is necessary to conclude the $\chi_{monolayer}$ for single layer Bi_2Se_3 . For total value of χ^3 can be calculated using the formula [18]

$$\chi_{total}^{(3)} = \chi_{monolayer}^{(3)} \times N_{eff}^2 \dots\dots\dots (5.7)$$

Where N_{eff} represents the effective number of layers in the cuvette.

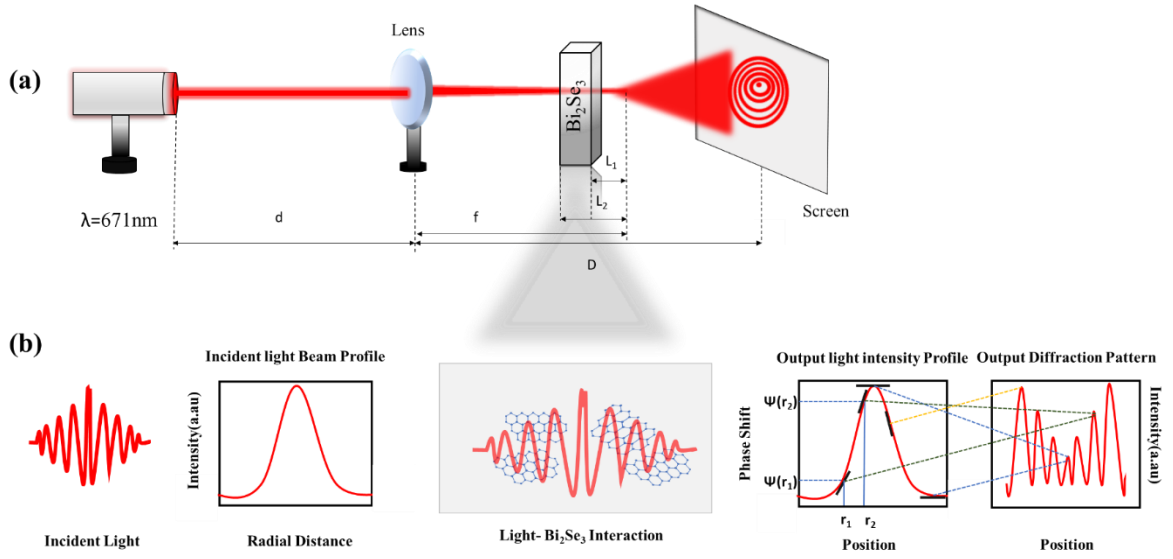


Fig. 5.3 Schematic of the experimental setup and SSPM in Bi_2Se_3 NFs. (a) Experimental setup for SSPM study of Bi_2Se_3 NFs. (b) Schematic diagram of the microscopic light-matter interaction process: The diffraction ring produced through the coherent interaction of light and suspended Bi_2Se_3 NFs.

This $\chi_{\text{total}}^{(3)}$ has strong dependence on the electric-field strength of the incident laser light.

The dN/dI is a crucial parameter for the determination of the NLO refractive index of the material. Figure.5.3(a) shows the optical setup necessary for the SSPM experiment.

The figure 5.4(a) ①-⑥ shows different ring patterns projected in screen as a function of intensity of light emitted from the laser itself (for $\lambda = 671 \text{ nm}$). As we can see from the figure5.4(a) that with intensity the number of ring increases linearly, also the horizontal diameter increases. The same experiment has been done for $\lambda = 532 \text{ nm}$ and $\lambda = 405 \text{ nm}$. The

experimental results for the latter two can be seen in figure 5.4(b) ①-⑥ (for $\lambda=532$ nm)

and figure.5.4(c) ①-⑥ (for $\lambda=405$ nm).

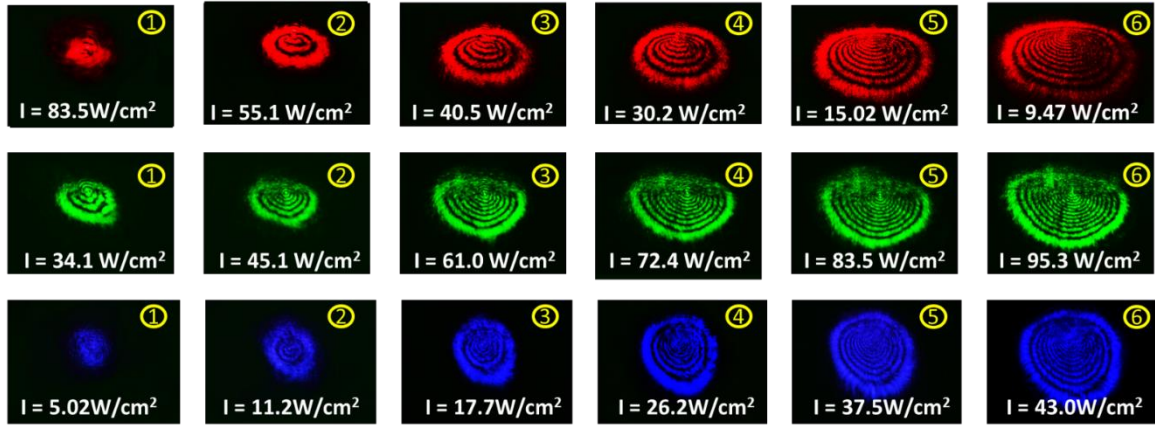


Fig.5.4(a) ①-⑥ The evolution of diffraction ring patterns on the screen with the intensity of incident laser ($\lambda = 671$ nm). (b) ①-⑥ the evolution of diffraction ring patterns on the screen with the intensity of incident laser ($\lambda = 532$ nm). (c) ①-⑥ the evolution of diffraction ring patterns on the screen with the intensity of incident laser ($\lambda = 405$ nm).

It was found that with decreasing wavelength the dN/dI increases. This is shown in the figure. 5.5(a)(b)(c).

The Figure 5.5 shows the linear variation of ring numbers and corresponding linear fit as function of incident laser intensity. The slopes (dN/dI) are found to be 1.271, 3.2705 and 5.756 for $\lambda = 671$, 532 and 405 nm, respectively. The results reveal that dN/dI increases with decreasing wavelength of the incoming laser beam. Here, the larger photon energy gives rise to higher SSPM effects, this theory is consistent with other previously reported results[19, 20].

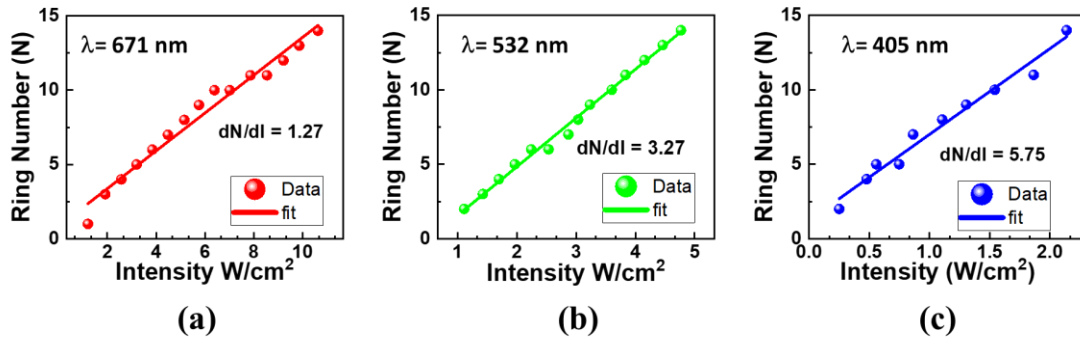


Fig.5.5(a) The plot of different ring numbers vs intensity of the laser light ($\lambda = 671$ nm) **(b)** The plot of different ring numbers vs intensity of the laser light ($\lambda = 532$ nm) **(c)** The plot of different ring numbers vs intensity of the laser light ($\lambda = 407$ nm).

Table: 5.1 Calculated n_2 and χ^3 from SSPM experiment at different wavelength.

Wavelength(λ) nm	L (mm)	C (mg/ml)	dN/dI (cm ² /W)	n_0 (cm ² /W)	n_2 (cm ² /W)	$\chi^{(3)}$ total	$\chi^{(3)}$ monolayer
671	10	0.25	1.27	5.54	7.746×10^{-6}	0.00602	1.9×10^{-8}
532	10	0.25	3.27	3.75	2.321×10^{-5}	0.00829	2.62×10^{-8}
407	10	0.25	5.75	2.26	5.156×10^{-5}	0.0066	2.11×10^{-8}

Now we have calculated the non-linear refractive index of the material n_2 and non-linear susceptibility (χ^3) of the material. This is represented in the table 5.1 format above.

The variation caused by the cuvette is reported in-terms of dN/dI change is shown in figure. 5.6. This result can be understood by the amount of interaction of light with suspended nanoflakes.

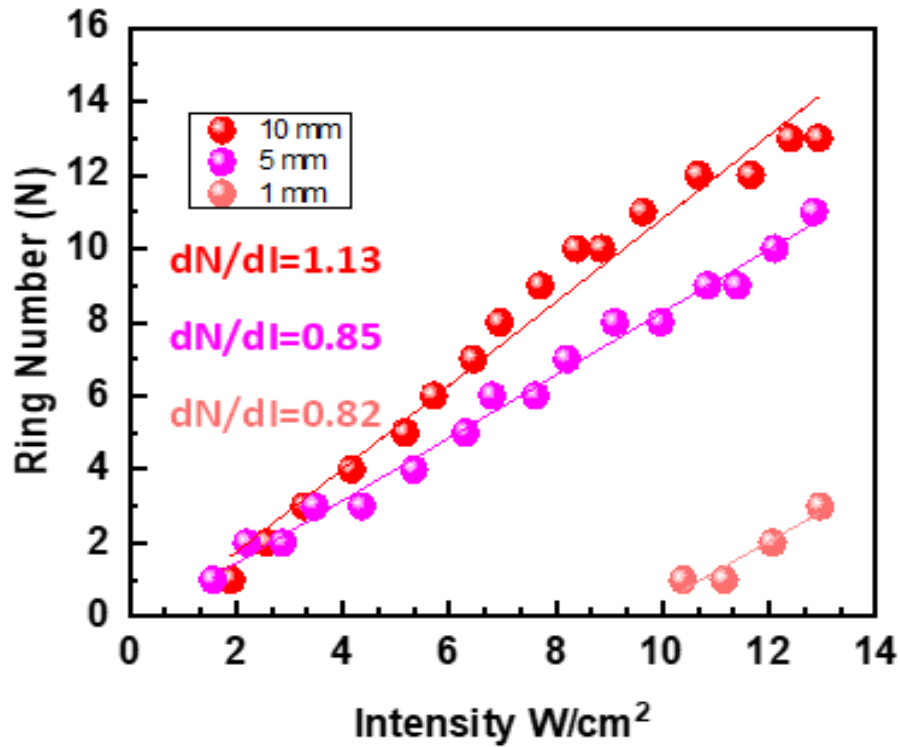


Fig. 5.6 The variation of diffraction ring numbers with incident laser beam intensity with cuvette lengths of 1,5 and 10mm.

increasing cuvette thickness the amount of interaction between the light and the suspended material increases. The electrons of the NFs oscillate coherently due to strong light-matter interaction. This causes larger spatial phase shift of the incoming light which creates more diffraction rings.

5.3.2 SSPM Mechanism of Light-Matter Interaction

In the non-linear Kerr effect, that leads to SSPM, the diffraction ring number increases with time and the n_2 and the $\chi_{total}^{(3)}$ depends upon the suspended 2D flakes on the solution.

In the SSPM technique the no. of diffraction ring increases with time leading to a maximum value. The time required to reach a maximum diameter at a fixed intensity is described by wind-chime model proposed by Wu et al[18]. This, model suggests that the intense laser beam polarizes the suspended nanoflakes of the material in the solution along the direction of the electric field through energy relaxation process. With time the number of rings increases, as the number of the nanoflakes to get oriented in the direction of electric field increases. Oriented nanoflakes interact coherently with the incident laser beam and initially a bright spot is formed with time. When all the nanoflakes are reoriented with electric-field, the full circular rings appear. This is shown in the figure 5.7. it is shown how the number of ring increases with time. According to the wind chime model the time taken to form maximum diameter diffraction pattern is the time taken for the 2D NFs to reorient themselves. The ring formation dynamics follow the exponential decay model.

$$N = A(1 - e^{-t/\tau_c}) \dots \dots \dots (5.8)$$

where N is the number of rings, A is a constant, τ_c is the rise time of ring formation.

The minimum time required for the NFs to re-orient themselves are,

$$T = \frac{\epsilon_r \pi \eta \xi R c}{1.72(\epsilon_r - 1) I h} \dots \dots \dots (5.9)$$

where ϵ_r is the relative dielectric constant of the material, η is the coefficient of viscosity of the solvent, R is the domain radius, h is the flake thickness, and I is the intensity of the laser beam.

Also, keeping all the other parameters constant if we change the solvent of the material the with little bit more viscous material the time will change. Low viscous medium takes shorter time to reorient the suspended nanoflakes of the material towards the incident electric field. Hence lower the value of η the less time it will take to reorient the nanoflakes.

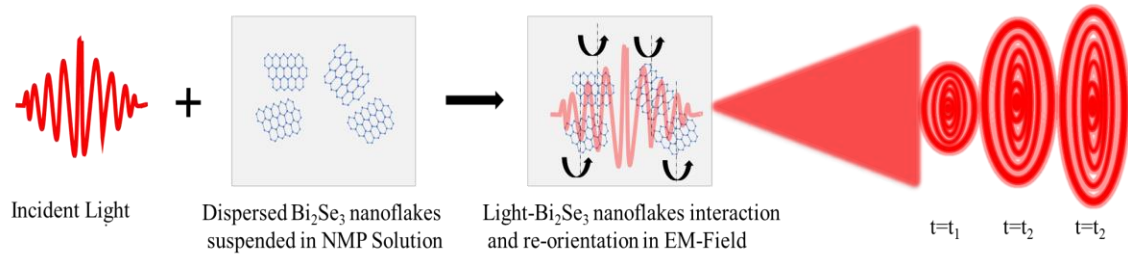


Fig.5.7 Schematic presentation of the formation of SSPM patterns for Bi₂Se₃ NFs via wind-chime model.

In the fig. 5.8(a) ①-⑧ shows the evolution process of the SSPM phenomenon for the wavelength 671 nm. Here we can initially see a bright spot is formed, as the nanoflakes becomes more oriented and aligned with time, a fully circular diffraction pattern can be seen. This process can be seen for other two wavelengths also, figure 5.5(b) ①-⑧ for $\lambda=532$ nm and figure 5.5(c) ①-⑧ for $\lambda=405$ nm. According to wind-chime model, the time required to produce fully circular pattern with maximum diameter is the same time required by the electric-field to reorient the nanoflakes. Here we have calculated the τ_c for wavelengths 671 nm, 532 nm and 405 nm, and the plot for ring number vs time is given in the figure 5.8(d), (e), (f) sequentially. The rise time for ring formation is found to be 0.28037 s (671 nm), 0.26706 s (532 nm) and 0.17742 s (405 nm).

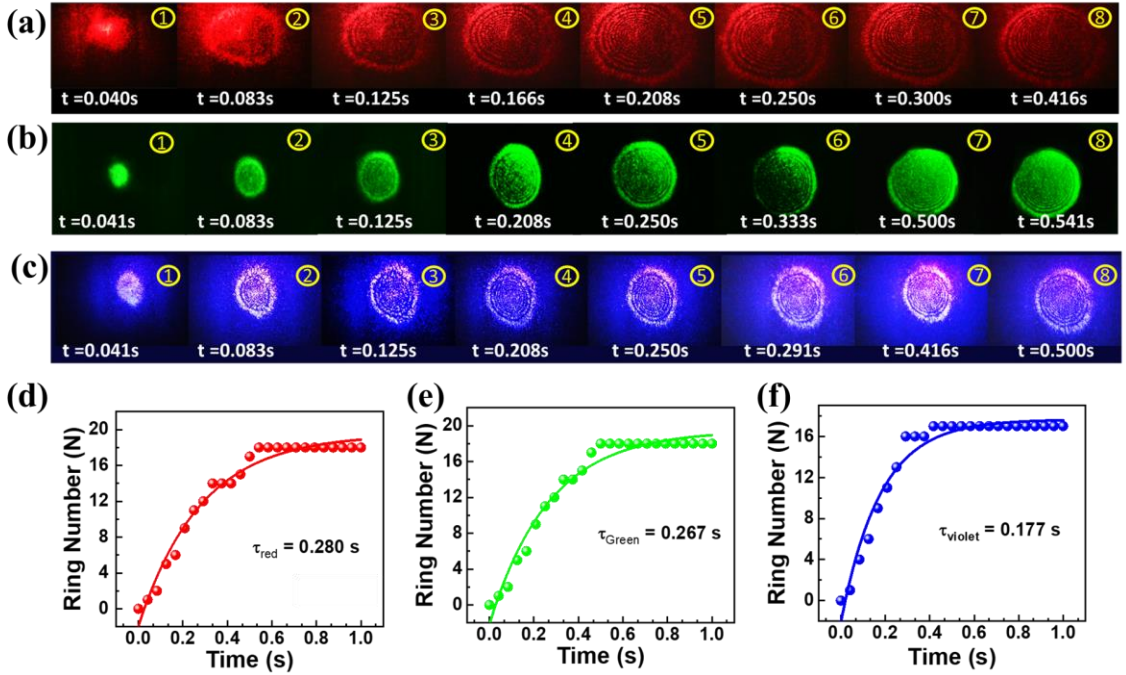


Fig.5.8(a-c) The diffraction ring pattern formed on the screen as function of time for $\lambda = 671$, 532 , and 405 nm, respectively. (d) The evolution of the diffraction ring numbers with time at highest intensity for $\lambda = 671$ nm. (e) The evolution of the diffraction ring numbers with time at highest intensity for $\lambda = 532$ nm. (f) The evolution of the diffraction ring numbers with time at highest intensity for $\lambda = 405$ nm.

In addition to the non-linearity the laser beam can cause temperature gradient in the solvent medium. This temperature gradient can cause change in non-linear refractive index in the upper part of diffraction ring pattern[21].

5.3.3 Dynamics of the Collapse Process of Diffraction Patterns

It can be seen that after some time upper half of the diffraction rings are getting distorted. In the SSPM process the diffraction rings form when the light interacts with the suspended Bi_2Se_3 nanoflakes. After the diffraction, rings reach its maximum number, the upper half of the ring pattern starts to collapse toward center.

Therefore, the upper part of the incident laser beam is less diffracted by the dispersed 2D materials which creates distortion in ring pattern which eventually collapses towards the center. This phenomena can be described by the half-cone angle of the diffraction pattern of the Gaussian laser beam, θ_H (the maximum half diffraction angle), which is change in phase shift, $\Delta\psi$ of the beam with respect to laser radial position, r and can be expressed as [19],

$$\theta_H = n_2 \left[-\frac{8IrL}{\omega_0^2} \exp\left(-\frac{2r^2}{\omega_0^2}\right) \right]_{max} \quad \text{-----}(5.10)$$

where, $\left[-\frac{8IrL}{\omega_0^2} \exp\left(-\frac{2r^2}{\omega_0^2}\right) \right]$ is a constant when $r \in [0, +\infty)$. Thus, θ_H is proportional to the effective nonlinear refractive index of the material. Again, the intensity-dependent collapse behavior, that occurs to the diffraction rings, is quantified by the change in diffraction angle formed between the sample and the screen. Now, through a series of coaxial cones, the formation of the diffraction rings can be described and the distortion angles can be described by

$$\theta_D = \theta_H - \theta_{H'} = \frac{R_H}{D} - \frac{R_{H'}}{D} = \frac{R_D}{D} \quad \text{-----}(5.11)$$

where R_H is the maximum diffracted radius, θ_H is the maximum half diffraction angle. After, the distortion in the rings happens, R_H and θ_H changes to new values $R_{H'}$ and $\theta_{H'}$, respectively. Also, θ_D can be expressed as, (in terms of the difference of non-linear refractive index)

$$\theta_D = \theta_H - \theta_{H'} = (n_2 - n'_2)IC = \Delta n_2 IC \quad \text{-----}(5.12)$$

where, C is $\left[-\frac{8rL}{\omega_0^2} \exp\left(-\frac{2r^2}{\omega_0^2}\right)\right]$. Therefore, the relative change in the non-linear refractive index can also be presented as the ratio between the distorted and maximum half-angle as,

$$\frac{\Delta n_2}{n_2} = \frac{\theta_D}{\theta_H} = \frac{R_D}{R_H} \text{-----}(5.13)$$

More distortion occurs in the vertical direction than along the horizontal direction as shown in figure.5.9 ①-②. After few seconds of time elapse the rings reaches an equilibrium position this can be seen in figure.5.9 ②. This collapse of upper half is due to the non-axis-asymmetrical thermal convection leading to the diffraction phenomenon, this has been described by Wang et al.[22]. During the diffraction phenomenon the dispersive medium absorbs some amount of energy from the propagating light through the medium. As a result, the temperature gradient increases with time enhancing the thermal convection process[23]. Once the wind chime has created more electrons coherence can be formed, and there will be less collision due to the re-orientation of 2D nanosheets. A large number of researchers believe that thermal lens effect co-exist with electronic coherence, recently Xiao et al. claimed to observe two mechanisms simultaneously in SSPM with Bi_2TeSe_2 [24].

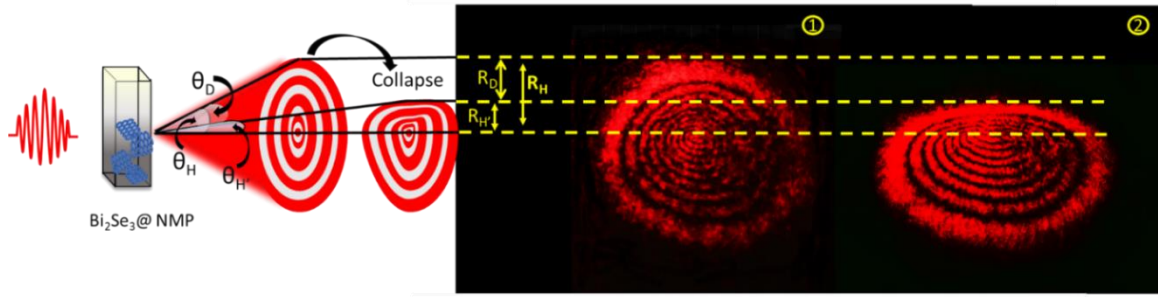


Fig.5.9. Schematic representation of the collapse process of the diffraction ring with half-cone and distortion angle. ① and ② are the real images of the SSPM diffraction pattern at maximum and distorted condition.

5.3.4 Non-Reciprocal Light Propagation in Bi_2Se_3 based Photonic Diode

We have also experimented with a novel-linear photonic diode device using Bi_2Se_3 - SnS_2 hybrid structure (figure 5.10(a)①-②) based on SSPM method. The SnS_2 is another material which shows non-linear optical response. The SnS_2 (2.6 eV) has larger bandgap than Bi_2Se_3 (0.3 eV), and the hybrid structure can be represented as photonic diode for non-reciprocal light propagation[16, 20]. The laser light $\lambda = 671$ nm is used to characterize the photonic-diode based on Bi_2Se_3 - SnS_2 heterostructure. The photonic diode produces the diffraction pattern when the laser beam propagates in the forward direction (Bi_2Se_3 - SnS_2) in figure.5.10(b)①. Whereas in the reverse direction figure.5.10(b)② SnS_2 - Bi_2Se_3 no diffraction is achieved. In the reverse direction large absorption through SnS_2 reduces the intensity of the laser light, so that when the light reaches to the Bi_2Se_3 , it is unable to produce the diffraction pattern. This property of material can be used for all optical switching application where non-reciprocal light propagation can be achieved. Here the value of dN/dI is found to be 1.088 for $\lambda = 671$ nm. This is nearly same as the slope with single cuvette Bi_2Se_3 solution. In this experiment laser light of higher energy than Bi_2Se_3

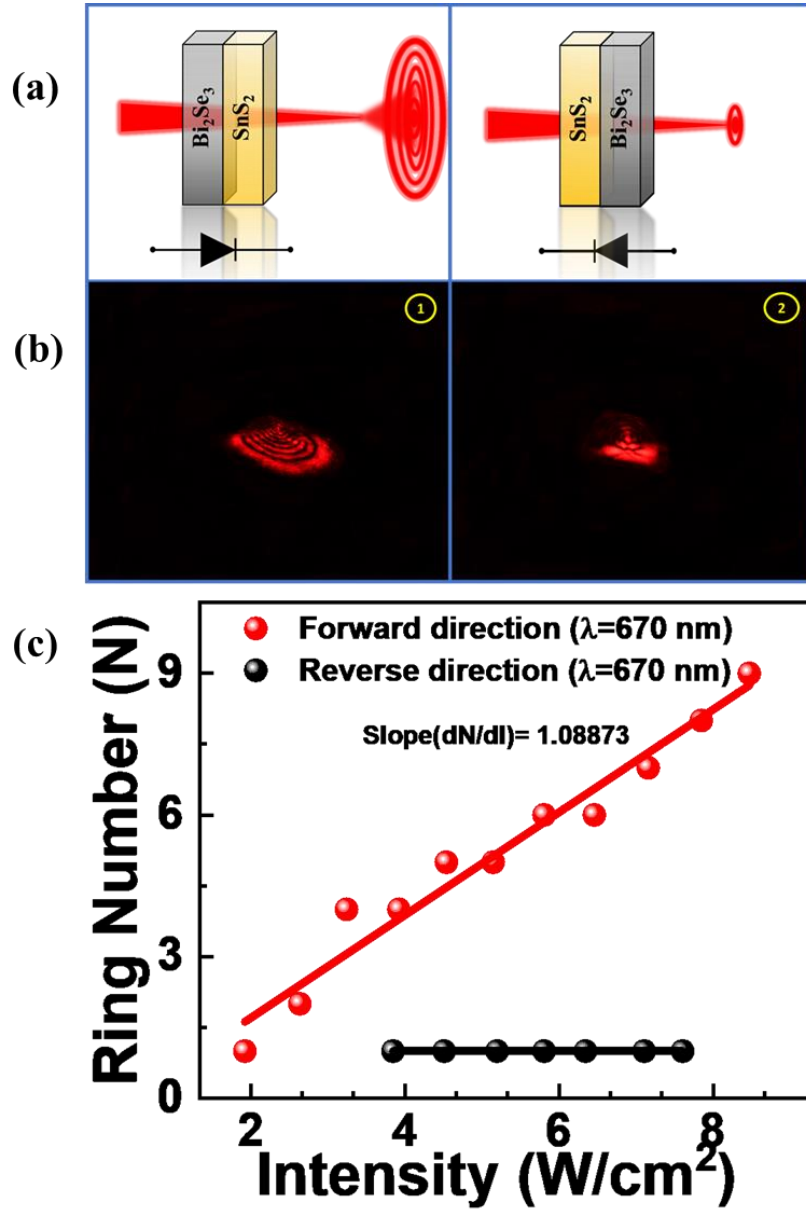


Fig. 5.10: Nonreciprocal light propagation in all-optical photonic diode. (a) shows the schematic presentation of the nonreciprocal light propagation in forward and reversed direction. (b) ① and ② shows the diffraction patterns obtained at forward condition and reverse-biased condition for $\lambda = 671$ nm respectively. (c) The experimental result obtained for the nonlinear photonic diode based on $\text{Bi}_2\text{Se}_3/\text{SnS}_2$ hybrid structure for incident laser light of $\lambda = 671$ nm.

(bandgap 0.3 eV) is used. So that photon can excite the electrons to go from lower energy state to higher energy state, the electrons go from valance band to conduction band. After some time, the electrons emit the photon and go to ground state. This emitted photon interacts with incoming laser light and produces optical Kerr effect[20]. In this process the

electrons move in the opposite direction as that of previous interaction, as that of applied electric-field and it polarizes the Bi_2Se_3 nanoflakes. The re-orientation process reduces the angle between the polarization direction and electric field applied to achieve minimum interaction energy configuration. Laser light of 532 nm and 671 nm is unable to excite the valence band electrons of the SnS_2 material, hence no diffraction rings are observed[20]. This above experiment is shown in the figure. 5.11.

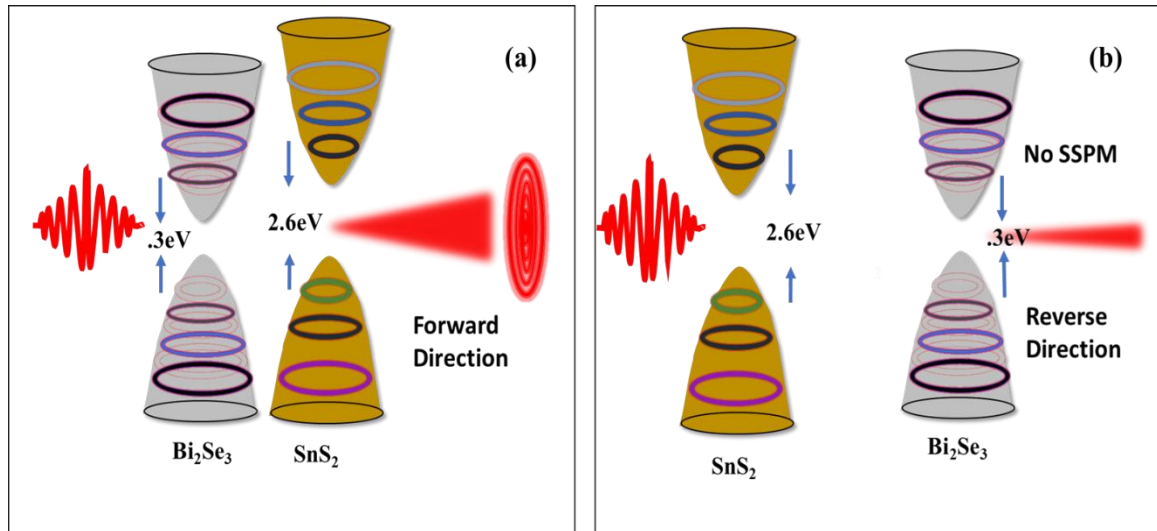


Fig. 5.11: Nonreciprocal light propagation in all-optical photonic diode. (a)bandgap arrangement during forward biased condition.(b) (a)bandgap arrangement during reverse biased condition.

Figure 5.11(a) the Bi_2Se_3 solution is placed in front of SnS_2 and the diffraction occurs as the intensity of the light passing through the Bi_2Se_3 solution causes the diffraction, it is concluded as forward bias condition. The figure 5.11(b) represents the reverse bias condition. Here the intensity of laser beam decreases after passing through SnS_2 solution, and yields no diffraction rings while passing through Bi_2Se_3 solution.

5.3.5 Cross-Phase Modulation : Bi₂Se₃ based All-Optical switching and Logic Gates

By taking advantage of SSPM of Bi₂Se₃ nanoflakes, an all-optical switching logic gate is demonstrated, to perform the logic operation of 'OR' Gate. This is shown in the figure 5.12. The schematic of this mode is shown in the figure 5.12(a). This logic operation is done using cross-phase modulation (XPM) technique[25]. Two lasers of different wavelength are used as the input signals (A, B) of the logic system and the resultant XPM is the corresponding outputs of the logic gate. This figure 5.12(b) shows the symbol and the switch circuit of the 'OR' Gate. When one of the input is high the output will be high (1), and when both inputs are at low level the output will be low (0). The corresponding switching scheme is shown in the figure 5.12(c). Here logic levels are realized by observing the number of rings formed using XPM process. Here we observed a two-laser system to achieve light-light modulation. The diffraction ring cannot form when the intensity of the incident light is too low, low interaction between light and sample causes and gaussian light appears, which is suggested to be '0' in logic level. Two individual lights of wavelength 671 nm and 532 nm are used as logic input 'A' and 'B', respectively. When both lights are cross-coupled and the final image is formed on the screen, this image is considered to be output 'Y'.

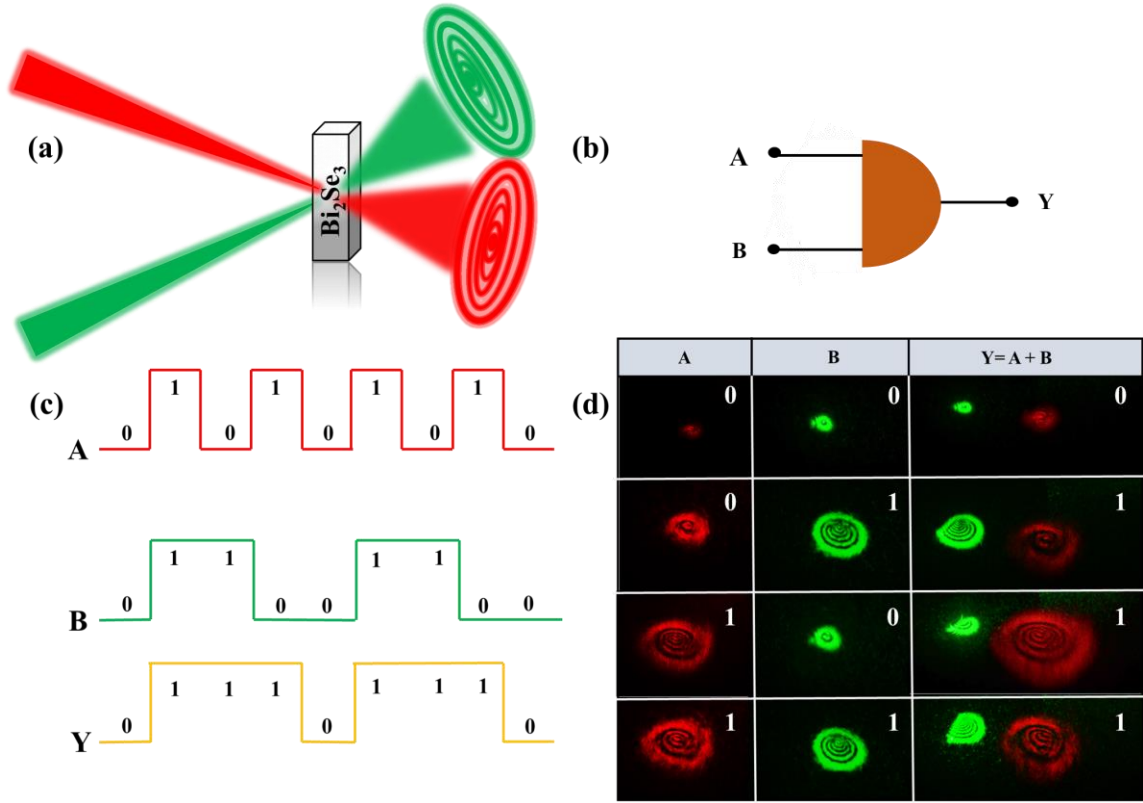


Fig.5.12(a)Schematic representation of XPM inside Bi_2Se_3 NFs for optical-logic gate application. (b) symbol and circuit model of the logic 'OR' gate. (c) The waveform of OR gate (input: A and B; output: Y). (d) Bi_2Se_3 based experimental results for optical OR gate operation using two-color XPM technique for the combination of $\lambda = 671 \text{ nm}$ & $\lambda = 532 \text{ nm}$

Fig. 5.12(d) shows output for different input generated due to cross-modulation happening. The diffraction rings are modulated. When another laser light (pump light) is cross modulated with Gaussian probe light, it can form diffraction rings on the screen for both lights. Based on the output using two-lasers we can build optical logic 'OR' gate. Here we have used laser of two different wavelengths 671nm and 532nm.

5.4 Conclusion

In this work, the SSPM phenomenon is reported on Bi_2Se_3 nanoflakes in NMP solvent. The Bi_2Se_3 Nanoflakes are synthesized using a cost efficient solvothermal technique. The

nonlinear broadband response of the Bi₂Se₃ nanoflakes has been investigated using laser beams of different wavelengths (671 nm, 532 nm, 405 nm). The non-linear refractive index and the third-order non-linear susceptibility is calculated from the change in number of rings at different laser power. The obtained n_2 and χ^3 for wavelength 671 nm is reported to be 7.74×10^{-6} esu and 1.9×10^{-8} esu. The large values indicate strong coherent non-linear interaction between light and suspended Bi₂Se₃ nanoflakes. The main theory behind the formation of the diffraction ring is understood to be wind-chime model. Based on SSPM method Bi₂Se₃-SnS₂ based diode has been investigated to demonstrate non-reciprocal light propagation. Also, an all optical “OR” gate application has been performed using cross-phase modulation method, involving two laser beams of different wavelength. It is believed that such non-linear optical phenomenon can open up new path for Bi₂Se₃ based all optical devices.

5.5 References

1. You, J., et al., *Nonlinear optical properties and applications of 2D materials: theoretical and experimental aspects*. 2019. **8**(1): p. 63-97.
2. Turitsyn, S.K., et al., *Inverse four-wave mixing and self-parametric amplification in optical fibre*. 2015. **9**(9): p. 608-614.
3. Wang, C., et al., *Nonlinear Optical Response of SbSI Nanorods Dominated with Direct Band Gaps*. 2021. **125**(28): p. 15441-15447.
4. Wu, Y., et al., *Electronic origin of spatial self-phase modulation: evidenced by comparing graphite with C60 and graphene*. 2016. **108**(24): p. 241110.
5. Jia, Y., et al., *Nonlinear optical response, all optical switching, and all optical information conversion in NbSe₂ nanosheets based on spatial self-phase modulation*. 2019. **11**(10): p. 4515-4522.
6. Wu, R., et al., *Purely coherent nonlinear optical response in solution dispersions of graphene sheets*. 2011. **11**(12): p. 5159-5164.
7. Wu, Y., et al., *Emergence of electron coherence and two-color all-optical switching in MoS₂ based on spatial self-phase modulation*. 2015. **112**(38): p. 11800-11805.
8. Xiao, S., et al., *Revealing the intrinsic nonlinear optical response of a single MoS₂ nanosheet in a suspension based on spatial self-phase modulation*. 2020. **8**(11): p. 1725-1733.
9. Liao, Y., et al., *All-optical applications for passive photonic devices of TaS₂ nanosheets with strong Kerr nonlinearity*. 2019. **806**: p. 999-1007.

10. Das, B., et al., *Topological insulator Bi₂Se₃/Si-nanowire-based p–n junction diode for high-performance near-infrared photodetector*. 2017. **9**(27): p. 22788-22798.
11. Das, B., et al., *Flexible, transparent resistive switching device based on topological insulator Bi₂Se₃-organic composite*. 2018. **124**(12): p. 124503.
12. Das, B., et al., *rGO-Wrapped flowerlike Bi₂Se₃ nanocomposite: synthesis, experimental and simulation-based investigation on cold cathode applications*. 2016. **6**(31): p. 25900-25912.
13. Razzaque, S., et al., *Selective synthesis of bismuth or bismuth selenide nanosheets from a metal organic precursor: investigation of their catalytic performance for water splitting*. 2021. **60**(3): p. 1449-1461.
14. Viti, L., et al., *Plasma-wave terahertz detection mediated by topological insulators surface states*. 2016. **16**(1): p. 80-87.
15. Wu, L., et al., *1D@ 0D hybrid dimensional heterojunction-based photonics logical gate and isolator*. 2020. **19**: p. 100589.
16. Song, C., et al., *Liquid phase exfoliated boron nanosheets for all-optical modulation and logic gates*. 2020. **65**(12): p. 1030-1038.
17. Zhang, J., et al., *Raman spectroscopy of few-quintuple layer topological insulator Bi₂Se₃ nanoplatelets*. 2011. **11**(6): p. 2407-2414.
18. Shan, Y., et al., *A promising nonlinear optical material and its applications for all-optical switching and information converters based on the spatial self-phase modulation (SSPM) effect of TaSe₂ nanosheets*. 2019. **7**(13): p. 3811-3816.
19. Shan, Y., et al., *Two-dimensional Bi₂Se₃-based all-optical photonic devices with strong nonlinearity due to spatial self-phase modulation*. 2019. **8**(12): p. 2225-2234.
20. Wu, L., et al., *Kerr nonlinearity in 2D graphdiyne for passive photonic diodes*. 2019. **31**(14): p. 1807981.
21. Dabby, F., et al., *thermally self-induced phase modulation of laser beams*. 1970. **16**(9): p. 362-365.
22. Wang, G., et al., *Tunable effective nonlinear refractive index of graphene dispersions during the distortion of spatial self-phase modulation*. 2014. **104**(14): p. 141909.
23. Teng, C., et al., *Flexible, thermally conductive layered composite films from massively exfoliated boron nitride nanosheets*. 2019. **124**: p. 105498.
24. Xiao, S., et al., *Observation of spatial self-phase modulation induced via two competing mechanisms*. 2020. **45**(10): p. 2850-2853.
25. Lu, L., et al., *All-optical switching of two continuous waves in few layer bismuthene based on spatial cross-phase modulation*. 2017. **4**(11): p. 2852-2861.

Chapter 6

Grand conclusion and future Scope

6.1 Conclusion

In this work '*Wearable, Ultrawide-Range, and Bending-Insensitive Pressure Sensor Based on 2D Bi₂Se₃ NFs coated tissue for Human-machine Interface and Healthcare Devices*' a cost-efficient, easy-to-fabricate pressure sensor has been fabricated that shows high sensitivity and flexibility. The sensing material is based on Bi₂Se₃ nanoflakes, and the microstructure is low-cost tissue paper. The tissue papers were soaked in Bi₂Se₃ nanoflakes (synthesized using simple solvothermal method) solution followed by simple stacking of multiple layers to form the pressure sensor; a top electrode and a bottom electrode were added with the help of Ag paste for measurement purpose. The fabricated pressure sensor showed excellent response due to unique structure and compressive electrical contact. The pressure sensitivity of the sensor is reported to be 25.1 kPa⁻¹ (in the range 0-2 kPa). The sensor is capable of detecting wide range of signals such as mobile vibration, weak air flow from mouth, voice recognition, bending, differentiating between different magnitude of pressures etc. All these characteristics are contributed to the high sensitivity of the sensor. Also, the optimized sensor in terms of layer variation, solution concentration that is used for soaking the tissue paper and the electrode material to fabricate well all-around sensor. This optimized sensor is then used to fabricate a e-skin which This previously mentioned e-skin array can be used to detect spatial pressure distribution and pressure magnitude. It is believed that such low-cost, easy-to-fabricate pressure sensor can open up new opportunities and applications in e-skin and smart wearable electronics.

In the work "*Kerr Non-Linearity in 2D Bi₂Se₃ for all Optical Switching and Photonic Logic Gate Application*" the non-linear optical response of the Bi₂Se₃ nanosheets has been explored. The non-linear response has been investigated using laser beams of different

wavelengths. The non-linear refractive index and third order non-linear susceptibility has been calculated for different wavelengths (671 nm, 532 nm and 405 nm). The reported high values of n_2 and χ^3 suggest strong light-matter interaction. This SSPM phenomenon is described by “Wind Chime model”. Based on SSPM method Bi_2Se_3 - SnS_2 based diode has been investigated to demonstrate non-reciprocal light propagation. Also, an all optical “OR” gate application has been performed using cross-phase modulation method involving two laser beams of different wavelengths. Different photonic device application is possible using Bi_2Se_3 nanoflakes. This non-linear optical properties can be further more explored to realize different domain of photonic application.

6.2 Future Scope

The Bi_2Se_3 nanoflakes can be used to realize different device application, such as spintronic device application, new type of heterojunction devices for light-detection capabilities etc. The topological insulator property can be used for quantum computing application. The fabricated pressure sensor can be used with real time circuit for health care monitoring. The SSPM phenomenon can be used to realize all optical devices.